Interfacial Phenomena and Surface Forces of Hydrophobic Solids

Dean J Mastropietro

Dissertation submitted to the faculty of the Virginia Polytechnic Institute and State University in partial fulfillment of the requirements for the degree of

Doctor of Philosophy

In

Chemical Engineering

William A Ducker

John Y Walz

Richey M Davis

Alan R Esker

Stephen M Martin

May 6th, 2014

Blacksburg, Virginia

Keywords: AFM, Hydrophobic, Aqueous, Surface Forces

Interfacial Phenomena and Surface Forces of Hydrophobic Solids

Dean J Mastropietro

ABSTRACT

At the molecular level the entropic "hydrophobic effect" is responsible for high interfacial energies between hydrophobic solids and aqueous liquids, the low solubility of apolar solutes in aqueous solvents, and self-assembly in biological processes, such as vesicle formation and protein folding. Although it is known that a strong attraction between apolar molecules exists at the molecular level, it is not clear how this force scales up to objects with dimensions in the range 100 nm–1 m. This work sets out to *measure* the forces between particles with a radius of about 10 μm. Because we can only measure the total force, which includes the van der Waals force and the electrostatic forces, it is important to isolate the effect of "hydrophobicity". We do this by measuring for systems where the particles are very hydrophobic (water contact angle, $\theta \sim 110°$) and the van der Waals and electrostatic forces are very small. Under these conditions we find that the total force is very small: it is similar to the van der Waals force at separations exceeding 5 nm.

Many early works on the hydrophobic force reported surface force at over 100 nm of separation. However, many of these strong, long-ranged attractive forces are likely caused by submicron interfacial bubbles, known as nanobubbles. Nanobubbles were imaged with an atomic force microscope to better understand their stability and dependence on solution properties, such as initial concentration of dissolved gas and changes in gas concentration. We found that nanobubbles still formed in degassed solutions and that lowering the dissolved gas concentration did not reduce the bubble size, implying that nanobubbles do not form from dissolved gas in the liquid phase or do not contain gas and are instead water vapor. Furthermore, addition of an oxygen scavenger agent, sodium sulfite, to a liquid phase that had been pressured with oxygen did not reduce bubble size which could be evidence that nanobubbles are impermeable to gas diffusion across the gas-liquid interface, do not form from the dissolved gas in the surrounding liquid, or do not contain gas and are instead water vapor.

"Our greatest weakness lies in giving up.

The most certain way to succeed is always to try just one more time."

-Thomas Edison

Table of Contents

I. Overview 1

Significance and Motivation 1

Overview of Sections 2

II. Literature Review 3

The Original Work by Israelachvili and Pashley 3

Other Literature 10

Nanobubbles and Hydrophobic Forces 11

Mobile Surface Charge and Hydrophobic Forces 13

Short-Range Forces between Hydrophobic Surfaces: The True Hydrophobic Force 17

Water at Hydrophobic Solids 19

III. *Atomic Force Microscopy Background and Techniques* 21

Contact Mode Force Measurement 23

Probe Characterization 23

Spring Constant Calibration 24

Force Curve Analysis 25

Features of a Force Curve 29

IV. Lifshitz Theory 32

Background 32

Van der Waals 33

Lifshitz Theory 33

Determination of Parameters from Absorption Data 35

Layered Bodies 39

V. Effect of Temperature on the Hydrophobic Force 41

Introduction 41

Experimental 46

The Total Force Between Hydrophobic Surfaces is Not Temperature Dependent 48

Conclusion of Temperature Effects 56

Significance of this Work 57

VI. Effect of Salt Concentration on the Hydrophobic Force 58

Introduction 58

Experimental 58
Preparation of Colloidal Probes 58
Preparation of OTS-coated Glass Plates 58
Preparation of OTS-coated Glass Spheres 59
Preparation of Solutions 59
Goniometry 59
Surface Imaaging 60
Cantilever Calibration 60
Atomic Force Microscopy 60
DLVO Predictions 61
Force Analysis 62
Force Between Hydrophobic Surfaces in Aqueous Solutions has the Form of a DLVO Force at Separations > 5-10 nm 66
The Position Of The Instability Is Independent Of Salt Concentration 67
Force Between Hydrophobic Surfaces in Aqueous Solutions at Low pH 73
The Force Between Pristine Hydrophobic Surfaces in Aqueous Solutions is Not Unique 75
Conclusions of Salt Concentration Effects 78
Significance of this Work 80
VII. Nanobubble Stability 81
Introduction 81
Literature Review 83
Nanobubble Stability 83
Nanobubble Formation 84
Materials and Methods 86
Surface Imaging 86
Substrate Preparation 86
Bare Mica and HOPG 87
Amine-terminated Silicon 87
Alkyl-terminated Glass and Silicon 87
Gold-Thiol 88
Solution Preparation 88

Dissolved Oxygen (DO) Measurements 88
Results and Discussion 89
Selecting a Surface for Use as a Metric for Distinguishing ONS60 and RNS60 89
Effect of Solution Exchange and the Impact of the Initial Solution 96
Are Nanobubbles Permeable to Gas? 96
Do Nanobubbles Without Oxygen Present? 99
Pinning of Nanobubbles at the Three Phase Line 101
Conclusions 103
VIII. Future Work 104
Characterization of the unstable region 104
Pull-off Force between Hydrophobic Surfaces 106
Linear Compliance from a Sliding Sphere 107
Do Bubbles Contain Gas? 108
References 110

List of Figures

Figure 1: Force vs Separation measurements for a *bare mica* system in water plotted with DLVO fits for constant charge and constant potential conditions. ***(Reprinted from Journal of Colloid and Interface Science, Vol. 98, Israelachvili, JN; Pashley, RM, Measurement of the Hydrophobic Interaction between 2 Hydrophobic Surfaces in Aqueous-Electrolyte Solutions, pp. 500–514. Copyright 1984, with permission from Elsevier)[54]*** **..... 4**

Figure 2: Force vs Separation measurements for a *CTAB-coated* mica system in water plotted with DLVO fits for constant charge, σ, and constant potential, , conditions. ***(Reprinted from Journal of Colloid and Interface Science, Vol. 98, Israelachvili, JN; Pashley, RM, Measurement of the Hydrophobic Interaction between 2 Hydrophobic Surfaces in Aqueous-Electrolyte Solutions, pp. 500–514. Copyright 1984, with permission from Elsevier)[54].*** **..... 5**

Figure 3: Force vs separation between hydrophobic surfaces plotted on a log-normal plot. Data points represent the difference between the total measured force (CTAB-coated mica in water) and predicted DLVO theory. Lifshitz predictions for mica-water-mica and hydrocarbon-water-hydrocarbon are also shown. ***(Reprinted from Journal of Colloid and Interface Science, Vol. 98, Israelachvili, JN; Pashley, RM, Measurement of the Hydrophobic Interaction between 2 Hydrophobic Surfaces in Aqueous-Electrolyte Solutions, pp. 500–514. Copyright 1984, with permission from Elsevier)[54].*** **..... 7**

Figure 4: $\partial(F_H/R)/\partial D$ vs separation for CTAB-coated mica in water. Values for $\partial(F_H/R)/\partial D$ were determined by summing the spring constant of the cantilever and the value of the gradient of the predicted DLVO interaction $\partial(F_{DLVO}/R)/\partial D_J$. ***(Reprinted from Journal of Colloid and Interface Science, Vol. 98, Israelachvili, JN; Pashley, RM, Measurement of the Hydrophobic Interaction between 2 Hydrophobic Surfaces in Aqueous-Electrolyte Solutions, pp. 500–514. Copyright 1984, with permission from Elsevier)[54].*** **..... 9**

Figure 5: Schematic showing how nanobubbles create "long-range" attractions. The separation between the nanobubbles is much smaller than the separation between the actual surfaces. So, a short range force between two bubbles could look like a long range force between two solids. Additionally, the coalescence of the bubbles produces a very strong attraction. These two factors have led to many groups misinterpreting nanobubble coalescence or bridging forces as long-range hydrophobic forces. 13

Figure 6: Schematic of how surface-charge mobility on neutral surfaces can produce an attraction. Well-anchored groups (top) maintain homogeneous charge distribution and result in a net repulsion (symmetric surfaces always produce a repulsive double-layer) while mobile charges (bottom) produce a heterogeneous charge distribution and result in a net attraction if the net charge is zero. 15

Figure 7: Schematic showing the method for detecting force in an atomic force microscope. 22

Figure 8: Scanning a sphere-mounted cantilever over a single tip on a characterization grating produces an image of the sphere topography. 24

Figure 9: Schematic of the regions of a deflection-displacement curve 26

Figure 10: Schematic showing how separation depends on both deflection and the distance moved by the piezoactuator. 28

Figure 11: Schematic of a force-separation curve. The solid line represents the region of mechanically stable force measurements while the dashed line represents the region of mechanically unstable data points..... 29
Figure 12: Cauchy plot demonstrating the effect different dissolved salts have on the spectral properties of water. Note that only the intercept (oscillator strength) varies with added solute. 37
Figure 13: Schematic of two half-spaces of material *A* coated with a layer of material A_1 of thickness a_1 and separated by a distance of *l* with an intervening medium *m*. 39
Figure 14: Lifshitz calculation for van der Waals interactions between two semi-infinite half spaces coated in a layer of hexadecane, thickness *t*, across 1 M aqueous salt solutions. The hexadecane is our model compound for OTS. The hydrocarbon film weakens the interactions. Variations in interaction energy with temperature are small. 45
Figure 15: Contact mode AFM image of a typical OTS-coated glass plate 47
Figure 16: Measured force vs separation for OTS-coated borosilicate glass interacting across aqueous 1.0 M KCl solution. The force has been normalized by $2\pi R$, which for a sphere-plate geometry is equal to the energy per unit area for flat plates (the Derjaguin approximation)[97]. Open circles show measured points at separations greater than the point of mechanical instability for the sphere (which occurs when the gradient of the attractive force equals the spring constant). The red (filled) circles represent smoothed data: the raw deflection data was smoothed using a 101-point moving average before conversion to force-distance. The smoothed curve was truncated 50 points (~0.50 nm) before the mechanical instability so that data from the instability is not included in the smoothing. In this data the mechanical instability occurred at about 6 nm, and in a series of repeat runs, instabilities occurred at 8.5 nm, 10.9 nm, 6.5 nm, 6.7 nm, 7.5 nm, 6.8 nm, 6.2 nm, 6.2 nm, 6.7 nm, and 7.0 nm. 49
Figure 17: Comparison between measured forces and Lifshitz calculation for borosilicate glass coated in OTS immersed in 1 M aqueous salt at 23°C. Circles and Squares represent data from different experiments. Lifshitz calculations represent the limiting cases of infinite and zero hydrocarbon thickness as well as the measured thickness of 2.7 nm. Closed symbols represent data averaged from several force runs. The random error in the force is about ±0.06 μN/m (i.e. about the point size) and in separation is ±0.1 nm. There is a systematic error of ±20% in the force arising from errors in the spring constant, the radius and the calibration of the spring deflection ("invols"). At small separations, there are fewer data points, so the data is not averaged. These unaveraged data points are shown as open symbols. The measured interactions agree with the calculated van der Waals interaction at separation greater than about 6 nm. Comparison at smaller separations is difficult because there are fewer measured points and greater error in the theoretical force. 51
Figure 18: Force as a function of temperature for OTS-coated borosilicate glass interacting across 1.0 M KCl. The measurements cannot resolve differences as a function of temperature. Lifshitz calculations represent the limiting cases of infinite and zero hydrocarbon thickness as well as the measured thickness of 2.7 nm. Filled markers represent averaged data points while open markers represent single measured data points. 54
Figure 19: Displacement vs deflection of an OTS-coated sphere and plate. Data was collected at 25 kHz at an approach/withdraw velocity of 20 nm/s. Contact was established prior to friction force measurement. The first linear-region (constant compliance) extends roughly 40 nm on both the approach and the withdraw. After the applied force overcomes the static friction force the probe slides across the surface manifesting as a change in the slope of the linear-compliance region. .. 64

Figure 20: Force vs separation curves for OTS-coated borosilicate glass surfaces immersed in aqueous 15 mM KCl solution. Force is normalized by 2πR, which for a sphere-plate geometry is the interaction energy per unit area for flat-parallel plates (the Derjaguin approximation)[104, 105]. The original force data (black dots) was truncated up to the mechanical instability so that data from the instability were not included in the average. The averaged data (red triangles) is an 80-point running average. 65

Figure 21: Gradient of the DLVO force with respect to separation for 15 mM, 150 mM and 1 M KCl. The theoretical electrostatic double layer force is calculated from Debye-Hückel theory using a surface potential of 60 mV and a Debye length of 2.5, 0.8, and 0.3 nm for 15 mM, 150 mM and 1 M KCl, respectively. Lifshitz theory was used to predict the van der Waals force between OTS-coated glass surfaces separated by aqueous salt solution. 68

Figure 22: Force vs separation curves for OTS-coated borosilicate glass surfaces in 15 mM KCl at 23° C. Triangles, diamonds, and squares represent different experiments. Each curve is an average of a single, typical curve from the data set. A mechanical instability occurs at 7–10 nm in all experiments. The solid line is the sum of the electrostatic double layer and the van der Waals prediction for the system. The theoretical electrostatic double layer force is calculated from Debye-Hückel theory using a surface potential of 60 mV and a Debye length of 2.5 nm. Lifshitz theory was used to predict the van der Waals force between OTS-coated glass surfaces separated by aqueous salt solution. 70

Figure 23: Force vs separation curves for OTS-coated borosilicate glass surfaces in 150 mM KCl at 23° C. Triangles, diamonds, and squares represent different experiments. Each curve is an average of a single, typical curve from the data set. A mechanical instability occurs at 7–10 nm over all experiments. The solid line is the sum of the electrostatic double layer and the van der Waals prediction for the system. The theoretical electrostatic double layer force is calculated from Debye-Hückel theory using a surface potential of 60 mV and a Debye length of 0.8 nm. Lifshitz theory was used to predict the van der Waals force between OTS-coated glass surfaces separated by aqueous salt solution. 71

Figure 24: Force vs separation curves for OTS-coated borosilicate glass surfaces in 1 M KCl at 23° C. Diamonds and squares represent different experiments. Each curve is an average of a single, typical curve from the data set. A mechanical instability occurs at 5–10 nm over all experiments. The solid line is the sum of the electrostatic double layer and the van der Waals prediction for the system. The theoretical electrostatic double layer force is calculated from Debye-Hückel theory using a surface potential of 60 mV and a Debye length of 0.3 nm. Lifshitz theory was used to predict the van der Waals force between OTS-coated glass surfaces separated by aqueous salt solution. 72

Figure 25: Force vs separation curves for OTS-coated borosilicate glass surfaces in 15 mM, 150 mM and 1 M KCl at 23° C. Squares, triangles, and circles represent KCl concentrations of 15 mM, 150 mM, and 1 M, respectively. Each curve is an average of a single, typical curve from the data set. A mechanical instability occurs at 5–10 nm over all experiments. 73

Figure 26: Force vs separation curves for OTS-coated borosilicate glass surfaces in 1 mM and 10 mM KCl solutions at pH 2 and 23° C. Open and closed circles represent KCl concentrations of 1 mM and 10 mM, respectively. Each curve is an average of a single, typical curve from the data set. A mechanical instability occurs at 5–10 nm for both concentrations. The dashed line is a Lifshitz theory prediction of the van der Waals force between OTS-coated glass surfaces separated by aqueous salt solution. The '×' symbols are the 1 M KCl data found in Figure 17. 77

Figure 27: Force vs separation curves for OTS-coated borosilicate glass surfaces in 15 mM KCl at 23° C. Different symbols represent different approaches in the same experiment. An 80-point moving average is taken of each curve to reduce the number of points. The "First Contact" curve was measured without any prior contact between the sphere and the plate. 78

Figure 28: AFM tapping (top) and contact (bottom) mode images of a 20×20 μm² region of bare mica (θ_A<10°) submerged in RNS60. Imaging was performed on a Cypher AFM (Asylum Research) using an ORC8 cantilever (68 kHz, 0.38 N/m, Bruker). 90

Figure 29: AFM tapping (top) and contact (bottom) mode images of a 20×20 μm² region of APTES-coated (θ_A=60°) silicon submerged in RNS60. Imaging was performed on a Cypher AFM (Asylum Research) using an ORC8 cantilever (68 kHz, 0.38 N/m, Bruker). 91

Figure 30: AFM tapping (top) and contact (bottom) mode images of a 20×20 μm² region of HOPG (θ_A=85°) submerged in RNS60. Imaging was performed on a Cypher AFM (Asylum Research) using an ORC8 cantilever (68 kHz, 0.38 N/m, Bruker). 92

Figure 31: AFM tapping (top) and contact (bottom) mode images of a 20×20 μm² region of undecanethiol on silicon (θ_A=100°) submerged in PNS60. Imaging was performed on a Cypher AFM (Asylum Research) using an ORC8 cantilever (68 kHz, 0.38 N/m, Bruker). 93

Figure 32: AFM tapping (top) and contact (bottom) mode images of a 20×20 μm² region of OTS-coated silicon (θ_A=110°) submerged in RNS60. Imaging was performed on a Cypher AFM (Asylum Research) using an ORC8 cantilever (68 kHz, 0.38 N/m, Bruker). The black bands in the top image are an artifact from image processing and are not a feature of the surface. 94

Figure 33: AFM tapping mode images of two different 20×20 μm² regions of a hexadecanethiol on silicon (θ_A=100°) substrate submerged in ONS60. Imaging was performed on a Cypher AFM (Asylum Research) using an ORC8 cantilever (68 kHz, 0.38 N/m, Bruker). The black bands are artifacts from image processing. 95

Figure 34: AFM tapping mode images of a 3×3 μm² region of OTS-coated silicon submerged in RNS60 before (left) and after (right) the addition of sodium sulfite. Imaging was performed on a Cypher AFM (Asylum Research) using an ORC8 cantilever (68 kHz, 0.38 N/m, Bruker). Circles are used to give a reference scale for changes in size between the two images. 97

Figure 35: AFM tapping mode images of a 3×3 μm² region of OTS-coated silicon submerged in RNS60 before (left) and after (right) the addition of sodium sulfite. Imaging was performed on a Cypher AFM (Asylum Research) using an ORC8 cantilever (68 kHz, 0.38 N/m, Bruker). Circles are used to give a reference scale for changes in size between the two images. 98

Figure 36: AFM tapping (left) and contact (right) mode images of a 20×20 μm² region of OTS-coated silicon submerged in ONS60 with sodium sulfite. Imaging was performed on a Cypher AFM (Asylum Research) using an ORC8 cantilever (68 kHz, 0.38 N/m, Bruker). 100

Figure 37: AFM contact mode imaging of a 2.5×2.5 μm² region of OTS-coated silicon submerged in RNS60 after sodium sulfite had been added. Relative set points ($V_{rel} = V_{sp} - V_{zero}$) for each image were as follows: a) 120 mV, b) 80 mV, c) 350 mV, d) 250 mV and e) 120 mV. Imaging was performed on a Cypher AFM (Asylum Research) using an ORC8 cantilever (68 kHz, 0.38 N/m, Bruker). 102

Figure 38: Force vs separation curve for OTS-coated borosilicate glass surfaces submerged in 150 mM KCl at 23° C. The red curve represents the approach curve and the blue curve represents the withdraw curve. The photodiode is saturated from 0 to ~6 μm of separation on the withdraw curve. The sharp increase in slope is an artifact caused by the laser falling off of the photodiode, giving the illusion that the deflection is decreasing because the overall voltage reading on the photodiode is decreasing. The two surfaces separate at the point marked by the arrow. The ~6

μm of deflection on the cantilever propels it through the fluid passed the line of zero deflection. 106
Figure 39: Schematic of a sphere and plate in contact during constant compliance. At high deflections the sphere may slide down (or up) and inclined planar surface and give the illusion that separation is changing even when the two surfaces are in hard contact. 108

List of Tables

Table 1: Pull-off Force 55

I. Overview

Significance and Motivation

On the molecular scale the hydrophobic effect is a well understood phenomenon that plays a key function in industrial and biological processes such as detergency, emulsification, protein folding, and bilayer formation. However, at the macroscopic scale the interactions between hydrophobic materials in water are poorly understood and riddled with highly contradicting experimental results. The so called 'hydrophobic force' is the last known fundamental interaction that is not understood. The primary objective of this research is to characterize the hydrophobic force. Atomic force microscopy (AFM) will be used to study the interactions between apolar surfaces in aqueous media as a function of temperature and electrolyte concentration. The secondary objective will be to understand the nature of interfacial nanobubbles. These bubbles form on hydrophobic surfaces, and cause difficulties in the interpretation of force measurements.

The hydrophobic force has been widely studied through both experiment[1-42] and simulations[43-53] for the past thirty years. This activity began when Israelachvili and Pashley reported that there was an attractive force between hydrophobic solids with a range of approximately 10 nm[54]. This discovery was treated with great excitement because hydrophobicity was thought to be an effect of water structure and, at the time, there was no reason to believe that the structure of water would be perturbed over distances exceeding a few nanometers. Following the original findings, some have

reported forces ranging from 10 nm to well over 100 nm, and there are contradicting reports on the effects of electrolyte concentration. No single mechanism has been able to describe all of the results that have been published thus far. Several reviews of the literature[5, 55, 56] suggest that this is due to the wide variety of preparation techniques and insufficient characterization of hydrophobic surfaces. Additionally, only one group has measured of an *attractive* force[57]. In the work described here, only well-characterized hydrophobic surfaces will be used to measure the total force between hydrophobic surfaces using AFM, and the force will be compared to Lifshitz calculation of van der Waals forces. Only forces in excess of all known (electrostatic, van der Waals) forces will be considered to arise from hydrophobicity.

Overview of Sections

Section II, the literature review, will cover the findings of Israelachvili and Pashley as well as some of the mechanisms believed to be the cause of the wide variation in forces reported in the literature; sections III and IV will cover AFM force analysis and a brief overview of Lifshitz theory; sections V and VI will cover my progress in measuring the hydrophobic force and determining its origin; section VII will my work on the origins of a related phenomenon, interfacial nanobubbles; finally, section VIII will discuss proposed continuations of my research that aim to solve the mystery of the long-range hydrophobic force.

II. Literature Review

The Original Work by Israelachvili and Pashley

One of the earliest studies into the hydrophobic force was done in 1984 by Israelachvili & Pashley. Their work was among the earliest experiments to claim a strong attraction between hydrophobic surfaces in water that was not described by Derjaguin-Landau-Verwey-Overbeek (DLVO) theory[54, 58]. DLVO theory describes the major forces that govern colloidal stability: the van der Waals and the electric double-layer[59].

Israelachvili & Pashley measured the forces acting between centimeter-sized surfactant-coated curved mica surfaces submerged in a series of salt solutions. Considering the large impact of their work in the area of hydrophobic force measurements, I will review their system, procedure, results and the significance of their work in detail.

Mica sheets were coated in a monolayer of hexadecyltrimethylammonium bromide (CTAB), a cationic surfactant. The deposition was done by placing the sheets in a solution of CTAB just below the critical micelle concentration (CMC), the concentration at which a surfactant solution will form micelles in bulk solution. The two sheets were mounted into a surface force apparatus (SFA) and submerged in solutions of NaCl or KBr of varying concentrations (0–0.04 M) and varying pH (5.4–10.4) at 21° C and 50° C. Israelachvili and Pashley measured forces between bare mica and CTAB-coated mica to compare systems without and with hydrophobic interactions.

Israelachvili and Pashley compared their measured forces between bare mica sheets with calculations of DLVO theory that assumed that the mica either maintained a constant charge or a constant potential and interacted via a nonretarded van der Waals interaction (Figure 1). The charge or potential was a fitted parameter used to determine the double-layer force.

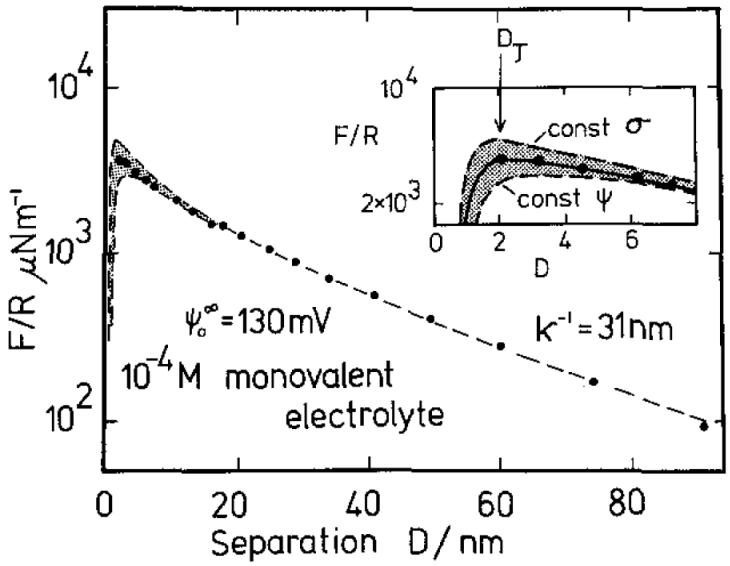

Figure 1: Force vs Separation measurements for a *bare mica* system in water plotted with DLVO fits for constant charge and constant potential conditions. *(Reprinted from Journal of Colloid and Interface Science, Vol. 98, Israelachvili, JN; Pashley, RM, Measurement of the Hydrophobic Interaction between 2 Hydrophobic Surfaces in Aqueous-Electrolyte Solutions, pp. 500–514. Copyright 1984, with permission from Elsevier)*[54]

The insert in Figure 1 shows that the measured interaction for *bare mica* agrees well with DLVO predictions all the way from large separation to the mechanical instability at approximately 2 nm of separation.

Force measurements for *CTAB-coated* mica were also plotted with DLVO fits (Figure 2). In Figure 2 it can be seen that their data fits to their DLVO calculations well from 10–30 nm but begins to deviate from the DLVO fit at separations less than 10 nm. The mechanical instability (D_J) occurred at a larger separation than would be expected for a nonretarded van der Waals attraction.

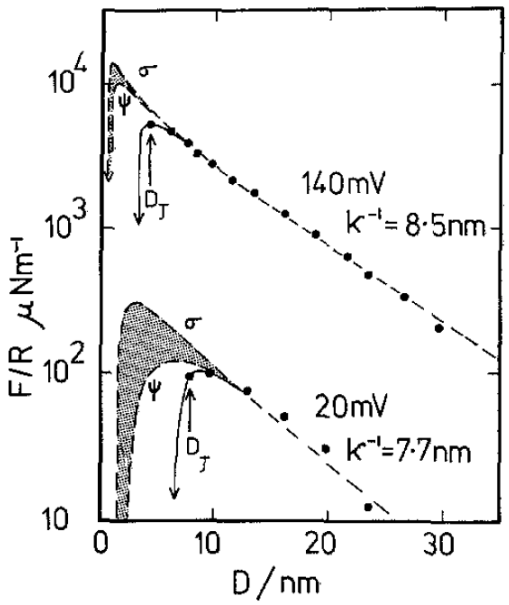

Figure 2: Force vs Separation measurements for a *CTAB-coated* mica system in water plotted with DLVO fits for constant charge, σ, and constant potential, , conditions. *(Reprinted from Journal of Colloid and Interface Science, Vol. 98, Israelachvili, JN; Pashley, RM, Measurement of the Hydrophobic Interaction between 2 Hydrophobic Surfaces in Aqueous-Electrolyte Solutions, pp. 500–514. Copyright 1984, with permission from Elsevier)*[54].

From Figure 2, it can be seen that the point labeled D_J in each case lies below the theoretical curve and therefore is less repulsive. Also, Israelachvili and Pashley observed that the point at D_J was the start of a mechanical instability. An instability occurs when the gradient

of an attractive force exceeds the gradient of the spring that is used to measure the force. Israelachvili and Pashley concluded that there was an attractive force causing these two effects. It is important to note that no actual attraction was measured before the jump-in and that an instability may occur even when the total measured force is repulsive: the instability is a function of the gradient of the force, not the sign or magnitude of the force.

Israelachvili and Pashley assumed that the total measured force, $F_{Measured}$, was the sum of van der Waals, F_{vdW}, electric double-layer, F_{EDL}, and hydrophobic forces, $F_{Hydrophobic}$. Estimates of DLVO forces were subtracted from the total force to reveal the underlying attractive force:

$$F_{Measured} = F_{EDL} + F_{vdW} + F_{Hydrophoic} \tag{1}$$

Figure 3 shows a plot of the resulting force (normalized by the radius) vs separation curve. They found that this hydrophobic force was well-described by an exponential-decay fit:

$$\frac{F_H}{R} = -0.14e^{-D/1.0nm}\ N/m \tag{2}$$

Equation (2) shows that the normalized hydrophobic force F_H/R varies exponentially with separation, D, with a decay length of 1 nm.

The critical difficulty in interpreting the work of Isrealachvili and Pashley is the accuracy of the double-layer force that was subtracted from the measured force. Isrealachvili and Pashley assumed that the minimum electrostatic interaction was at a fixed potential, the value of which was obtained at large separation. However, it is well known that the

adsorption of surfactant can cause a decrease and even a reversal of the surface potential. Lokar and Ducker used a thermodynamic argument derived by Hall [60] and by Ash et al. [61] to show that the surfactant does adsorb during the interaction, and this leads to neutralization of the surfaces, as is expected intuitively. Thus the "minimum" double-layer force that Isrealachvili and Pashley subtracted from their measured force to obtain the hydrophobic forces was not a minimum, but probably an overestimate. This means that the resultant hydrophobic force may be smaller in magnitude, which includes not existing at all!

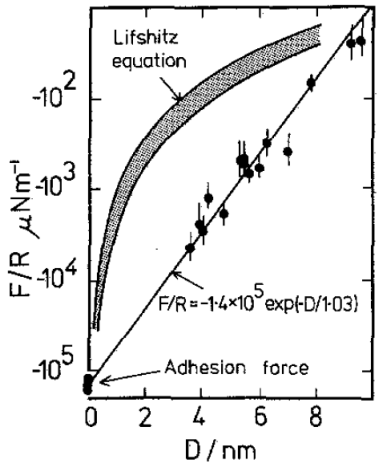

Figure 3: Force vs separation between hydrophobic surfaces plotted on a log-normal plot. Data points represent the difference between the total measured force (CTAB-coated mica in water) and predicted DLVO theory. Lifshitz predictions for mica-water-mica and hydrocarbon-water-hydrocarbon are also shown. *(Reprinted from Journal of Colloid and Interface Science, Vol. 98, Israelachvili, JN; Pashley, RM, Measurement of the Hydrophobic Interaction between 2 Hydrophobic Surfaces in Aqueous-Electrolyte Solutions, pp. 500–514. Copyright 1984, with permission from Elsevier)[54].*

Israelachvili and Pashley discussed a second approach to deriving a force law from their data that was based on the mechanical stability of the cantilever measurement system. Consider the criteria for mechanical stability:

$$\partial^2 E / \partial D^2 > 0 \tag{3}$$

Where E is the interaction energy between the two surfaces and D is separation. At the last mechanically stable point before an instability, the surface force is equal to the gradient of the spring force (the spring constant, k). When the gradient of the surface force exceeds the spring force, then the spring undergoes unstable motion (acceleration) until a new stable point is reached. In the context of a hydrophobic force measurement, at the point of mechanical instability, the gradient of the hydrophobic force, F_H is equal to the sum of the gradients of the two opposing forces F_{DLVO} and k:

$$\partial F_H / \partial D = \partial F_{DLVO} / \partial D + K \tag{4}$$

By varying spring constant for a given solution condition they were able to obtain $\partial F_H / \partial D$ as function of D which they found to fit an exponentially decaying functional form (Figure 4). An integration of this expression produced a force law for the additional surface force in their system:

$$\frac{F_H}{R} = -0.11 e^{-D/1.0nm} \; N/m \tag{5}$$

A comparison of the two force laws seen in eqns. (2) and (5) shows consistency, that is, the experimental uncertainty was small, but this did not overcome the fundamental issue of the inaccuracy of subtracting the extrapolated double-layer force with unproven assumptions.

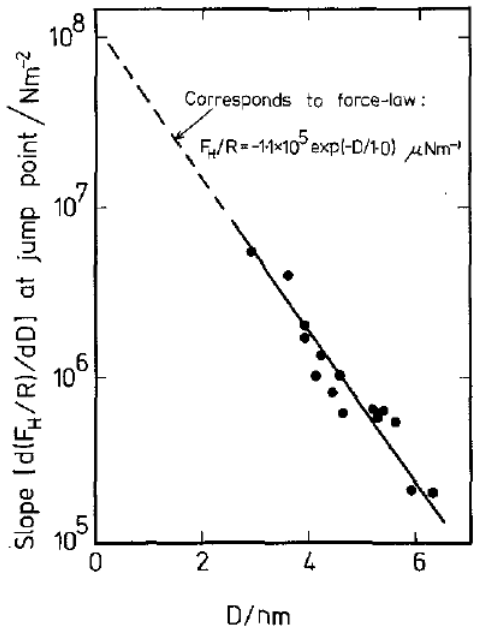

Figure 4: $\partial(F_H/R)/\partial D$ vs separation for CTAB-coated mica in water. Values for $\partial(F_H/R)/\partial D$ were determined by summing the spring constant of the cantilever and the value of the gradient of the predicted DLVO interaction $\partial(F_{DLVO}/R)/\partial D_J$. *(Reprinted from Journal of Colloid and Interface Science, Vol. 98, Israelachvili, JN; Pashley, RM, Measurement of the Hydrophobic Interaction between 2 Hydrophobic Surfaces in Aqueous-Electrolyte Solutions, pp. 500–514. Copyright 1984, with permission from Elsevier)*[54].

Israelachvili and Pashley also studied the effects of electrolyte type, electrolyte concentration and pH. These variables were found to have no effect on the interaction

within the range of error, although they did find that the strength of adhesion increased slightly as the electrostatic double-layer weakened.

Additionally, measurements were conducted with different concentrations of CTAB in solution as well as varying monolayer thickness from 0.8–1.8 nm to investigate the effect of the amount of CTAB on the system. These were also found to have no effect within the range of error though they do note that the thinner films show lower adhesion energies. These results show that the attraction was not caused by some mechanism related to excess surfactant being in solution.

Noting that the entropic contribution to the force is given by the temperature dependence of the force, they also did an experiment at 50° C. They found that the interaction decreased with temperature at small separation (D<5 nm) and the adhesion increased slightly, though the authors do point out that these results are only preliminary.

The key points are that no attraction was measured by Israelachvili and Pashley. Their reported exponentially decaying force law for the hydrophobic force was determined from subtracting DLVO estimations from their total measured force which contained an untested assumption.

Other Literature

Nearly thirty years after the earliest work on hydrophobic interactions[54] researchers have found themselves stricken with more questions than answers and every new publication finds itself telling a story slightly different than the last. Much of this is attributed to the fact that the hydrophobic interaction is incredibly sensitive to the surface preparation and

the details of the system. In recent years work has been done to compare and contrast the plethora of results in search of clues to why no single force law can fully describe all the reported data. Two notable reviews by Christenson & Claesson and Meyer et al. conclude that three regimes exist for hydrophobic attractions: I) an attraction of variable strength and range often displaying step-like behavior, II) a very long-range attraction with exponential decay, and III) a short-range, but very strong attraction[55, 56]. The majority of experimental data falls into type I[13, 14, 17, 27, 28, 62-64] and type II[1-8, 22, 27, 29, 31, 32, 38, 39, 54] while type III[17, 20, 26, 29, 33, 40] represents only a small fraction. Evidence suggests that type I and type II data are not actually hydrophobic forces but rather the result of bridging nanobubbles[13, 14, 35, 62, 65-69] and mobile surface groups[24, 31, 32, 42, 70], respectively. Type III forces are believed to be directly due to hydrophobic forces, however only a few experiments have shown purely Type III behavior. Thus, it is important to note that many forces described as "hydrophobic" by the authors may be due to indirect effects. For example, hydrophobic solids may be prone to "contamination" by bubbles, and the bubbles cause a force.

Nanobubbles and Hydrophobic Forces

It is now known that many claims of hydrophobic force measurement are actually due to the presence of nanobubbles adsorbed to a solid. Nanobubbles are thin patches of gas that reside at the interface between a hydrophobic solid and water and may be present on surfaces during force measurement.

The formation and longer-than-expected stability of nanobubbles is still not fully understood today. Many groups have reported systematic methods for producing nanobubbles by alcohol-water solvent exchange[69, 71, 72] with evidence showing that super-saturation of air in water encourages the formation of a gas-phase though it is not required. Contaminant is speculated to act as surfactant to lower the interfacial energy and stabilize the bubble[68]. This argument is difficult to prove as the amount of contamination required to stabilize a bubble would be difficult to detect.

Nanobubbles existing at the solid interface create cavitation forces that may greatly vary in range and magnitude. Many groups[13, 14, 17, 27, 28, 62-64] have found that the interactions reported between hydrophobic surfaces in aqueous solutions were actually the result of bridging bubbles that formed through the coalescence of preexisting nanobubbles. The nanobubbles themselves were not separated by a large distance, only the solids were separated by a large distance, so there was no need to invoke a very long range force. In fact, the force was not directly attributable to hydrophobicity, the presence of the bubbles was aided by the hydrophobicity. Figure 5 shows how nanobubbles create long-range interactions between solids when the nanobubbles are close together.

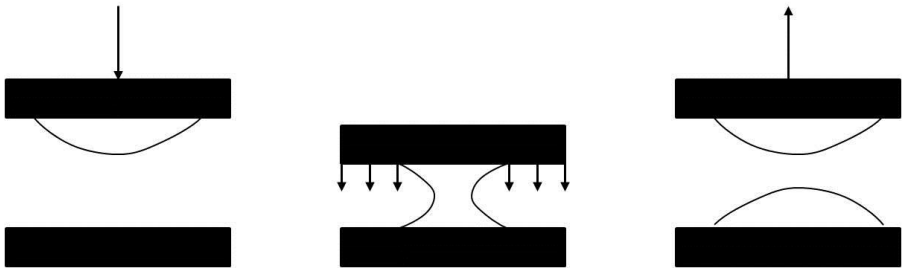

Figure 5: Schematic showing how nanobubbles create "long-range" attractions. The separation between the nanobubbles is much smaller than the separation between the actual surfaces. So, a short range force between two bubbles could look like a long range force between two solids. Additionally, the coalescence of the bubbles produces a very strong attraction. These two factors have led to many groups misinterpreting nanobubble coalescence or bridging forces as long-range hydrophobic forces.

Measurements in this thesis utilized degassed solutions, which limited the possibility of forming interfacial nanobubbles so that the effects of *hydrophobicity* on surface interactions in water could be properly investigated.

Mobile Surface Charge and Hydrophobic Forces

Other measurements of "hydrophobic" forces have been attributed to correlations between charge patches at the solid-water interface. Some techniques to produce hydrophobic surfaces using surfactant produce laterally mobile surface groups or allow for adsorption/desorption mechanisms. It has been found that such configurational freedom produces exponentially decaying forces between surfaces that are otherwise electrostatically neutral[70]. While most of these are found between surfaces formed by adsorption of cationic-surfactants or Langmuir-Blodgett deposition on glass or mica

sheets[1, 4, 6, 9, 22, 31, 32, 38, 39, 42] some glass and mica surfaces modified by vapor-deposition of silanes[27, 64] have also shown similar behavior.

Reviews of hydrophobic-force literature by Christenson & Yaminsky and Christenson & Claesson[5, 55] comment that surfaces modified by equilibrium adsorption undergo an equilibrium shift as separation changes. Monolayers formed by Langmuir-Blodgett, self-assembly from non-aqueous solvents or vapor-deposited silanes may allow for lateral mobility of surface groups which may result in heterogeneities or patch formation as separation changes[5, 55]. Statistical models have reported that configurations resulting in net attractions are favored for heterogeneous, net neutral surfaces (Figure 6)[70]. Christenson & Yaminsky go on to say that contact-angle hysteresis (indicative of the degree of surface homogeneity), rather than absolute contact-angle (indicative of the degree of hydrophobicity), can be correlated to the range of the hydrophobic force.

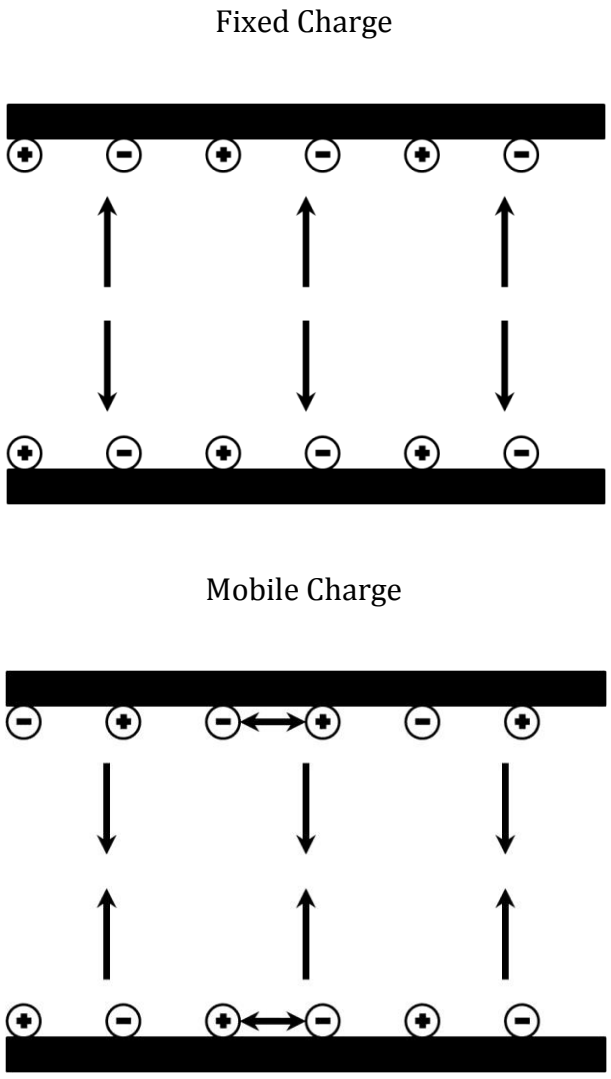

Figure 6: Schematic of how surface-charge mobility on neutral surfaces can produce an attraction. Well-anchored groups (top) maintain homogeneous charge distribution and result in a net repulsion (symmetric surfaces always produce a repulsive double-layer) while mobile charges (bottom) produce a heterogeneous charge distribution and result in a net attraction if the net charge is zero.

Some groups have also done studies for asymmetric surfaces (hydrophobic-hydrophilic) in water[27, 38] showing that hydrophobic-hydrophilic surfaces interact in a similar, albeit

quantitatively different, manner to hydrophobic-hydrophobic surfaces. For glass substrates the hydrophobic-hydrophilic interaction is found to be weaker than the hydrophobic-hydrophobic interaction for glass while mica substrates are found to have hydrophobic-hydrophilic interactions that are stronger than hydrophobic-hydrophobic interactions mica[27]. Such behavior helps support that lateral mobility or adsorption/desorption mechanisms may be the cause of long ranged interactions in these systems because mobile groups from the hydrophobic substrate could desorb and adsorb on the hydrophilic substrate creating two heterogeneous, partially hydrophobic surfaces, though some groups have reported that such mechanisms could not have taken place for their surfaces[8].

Several papers suggest that the measured force had a long-range contribution caused by the aforementioned monolayer instabilities and a short-range interaction caused by the hydrophobic properties of the surfaces[7, 15].

The works covered further emphasize the importance of surface preparation and characterization of modified surfaces both before and after experimentation to help assess whether the measured interactions are due to the hydrophobic nature of the surfaces or due to other properties of the monolayer, such as instability in water or the formation of surface heterogeneities. A combination of contact angle hysteresis and imaging of hydrophobic surfaces both before and after submersion in aqueous solutions should be sufficient evidence that the surface did not undergo any drastic change during force experiments.

Short-Range Forces between Hydrophobic Surfaces: The True Hydrophobic Force

The two covered sections of hydrophobic literature have shown that many papers that claimed to measure hydrophobic forces are actually measurements of forces that are not intrinsically due to hydrophobicity. The key question is: what is left when all these other forces are excluded? We will use the "true hydrophobic force" to describe such a force.

Some groups have also reported much shorter-ranged interactions in either the absence of[17, 20, 40] or presence of[7, 15] another longer-ranged force. The key features of this force are that it is stronger than van der Waals but of the same range and occurs between stable hydrophobic surfaces. Electrolyte has been found to have only a minor effect on the interaction while no conclusions could be drawn on pressure and temperature effects[20, 40, 55]. Several authors[29, 40] have attributed this short-range attraction to a spontaneous cavitation that has been discussed in theoretical simulations[46, 48, 49, 51, 52, 73, 74].

Surfaces that fit this category were very hydrophobic with high advancing contact angles ($\theta>90°$) and low contact angle hysteresis ($\Delta\theta<15°$) in addition to being smooth and robust. It has also been argued that these forces are much more sensitive to surface roughness and the chemical structure of the surface [citation].

It is very important to note that <u>none of the published work has directly measured an attractive force</u>. In some cases no interactions (repulsive or attractive) are measured before jump-in[20, 40] while others report a double-layer repulsion before jump-in[26, 29, 33, 37]. Although these experiments are in agreement with theoretical simulations of water confined between hydrophobic surfaces at small separations[44, 48, 49, 73, 74] it is difficult to

draw conclusions on the overall mechanism of the interaction without measuring an attraction because (a) it is not clear that there is an attractive force and (b) the functional form is unknown.

Lum et al.[48] argue that water confined between two hydrophobic plates will undergo cavitation at small separations. The hydrophobic effect causes disruption of the hydrogen bonding network near the hydrophobic interface for up to a few nanometers from the surface. When two plates draw near the density of water molecules in the gap becomes so low that a vapor phase is created to bridge the gap resulting in a strong cavitation[48]. Simulations by Lum et al. also show that cavitation occurred at about a separation of 10 nm, which is on par with the separation many groups[17, 20, 40] have reported their mechanical instabilities to occur.

It is clear that measuring the hydrophobic force is difficult due to the high susceptibility of nanobubble formation at the solid-water interface and the sensitivity of the interaction to the properties of the monolayer. Even in the case of a very stable surface most of the literature can only say that a mechanical instability occurred at separations larger than expected for a van der Waals force for a hydrocarbon-water-hydrocarbon system.

The hydrophobic effect (i.e. molecular scale hydrophobicity) is known to be entropic in origin. If the interaction between macroscopic surfaces has the same origin as the hydrophobic effect, then it should also be entropic and thus it is important to try to determine the entropy of the interaction. The change in entropy of an interaction can be

determined from the change in the Gibbs free energy of the interaction (which is determined from the measured force) with respect to temperature:

$$\left(\frac{\partial \Delta G}{\partial T}\right)_{D,P} = -\Delta S \tag{6}$$

Here the delta symbol represents the difference in the quantity at large separation and at small separation. Thus we can investigate the entropic contribution of a force by measuring the force distance relationship as a function of temperature. For example, the "true hydrophobic force" is expected to have a mechanism that depends on water ordering, in which case, the "true hydrophobic force" should be temperature dependent.

Water at Hydrophobic Solids

As mentioned above, the hydrogen bonding network of water is perturbed by neighboring hydrophobic surfaces. X-ray diffraction and ellipsometry for an *isolated* macroscopic hydrophobic surfaces both show that water structure is disturbed over only a very small distance from a hydrophobic surface: only the width of a few water molecules at most[75-78] . In fact, Mezger's work shows that the depletion layer of water molecules near a single hydrophobic surface is only a fraction of the size of a single water molecule. When water is confined in a thin film between two hydrophobic surfaces, the situation is qualitatively different because the existence of the thin water film can be thermodynamically unstable (depending on the geometry) and water may only exist in a kinetically trapped state[47]. However, simulation[43, 50, 79, 80] predicts diminished density and attractive forces that extend over only a few nanometers at most.

Wood and Sharma[40] measured the force in deaerated water between cm-sized mica surfaces coated in octadecyltriethoxysilane (OTE). They measured zero force at large separations, and a mechanical instability at about 17 nm separation; the mechanical instability indicated an attractive force with a gradient exceeding the stiffness of the measurement device, but the actual attractive force was not measured.

Meyer et al.[56] also measured the force between OTE-coated mica surfaces in water but without degassing the solution. Consistent with Sharma, they found that there was no force at separations greater than 15 nm. The authors report an instability at a distance of about 13 nm, but they determined the surface force in the unstable regime by an analysis of the dynamic motion of the surface attached to the measurement spring[23]. The authors report that because inertia and the spring force are essentially negligible, the surface force is roughly equal to the lubrication force, [23] which they calculate assuming that the slip-length is zero. At separations less than about 15 nm, they calculate an attractive force that is much greater (~100×) than the Lifshitz estimate of van der Waals forces. Note however, that the calculation of the surface forces is dependent on the boundary condition for lubrication flow. Cottin-Bizonne et al.[81] subsequently reported that the slip-length for very similar surfaces is *15 nm per surface*. Such a slip length would cause a large reduction in the estimated magnitude of the hydrodynamic force and a reduction in the hydrophobic force that is calculated from Meyer et al's data. Although Meyer et al. provides one of the best current estimates for the hydrophobic force, the estimate is again strongly affected by an assumed parameter. Hammer et al.[82] have repeated Meyer's work but with a slightly different OTE preparation and find roughly consistent results.

III. *Atomic Force Microscopy Background and Techniques*

The main technique used in this work is Atomic force microscopy (AFM), so the AFM force measuring technique will be briefly reviewed. Imaging with AFM is a technique used for characterizing chemical and physical surface properties, nanoscale topography, surface force measurement and metrology. First developed in 1986, the AFM was designed to characterize materials with the same level of force sensitivity and precision as a scanning tunneling microscope (STM) but without being limited to conductors and semi-conductors[83]. Similar in design to the STM, the AFM utilizes high-precision piezoactuators to displace a probe vertically and laterally (0.1 nm). The probe is attached to the tip of a cantilever which deflects towards or away from the surface as the probe experiences a force with the surface. The force is determined from the endslope of the cantilever, which is monitored by the deflection of a laser beam using a position-sensitive photodiode. The displacement of the cantilever is altered using a piezoactuator. This displacement is measured using a linear variable differential transformer (LVDT) (Figure **7**). The photodiode is split into four quadrants and deflection is measured from the difference in laser beam intensity between the upper and lower sections of the photodiode.

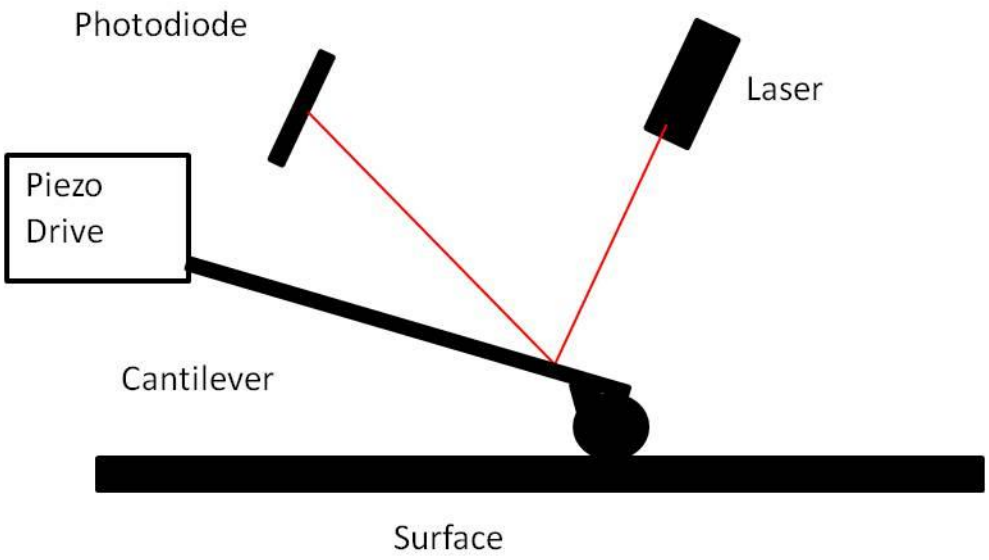

Figure 7: Schematic showing the method for detecting force in an atomic force microscope.

A feedback loop between the photodiode output and the vertical piezoactuator is used to maintain a constant deflection (force). Topographical images are produced by recording the z-position of the piezoactuator as a function of lateral position on the surface. This technique of AFM, known as contact mode, is restricted to hard surfaces. Soft materials or soft adsorbates may be studied using non-contact, or dynamic, mode AFM which feeds back on the amplitude or phase of an oscillating cantilever (e.g. Tapping Mode AFM). Dynamic mode AFM has a myriad of applications for material characterization, fluidics, and biological systems; however, the work presented here utilizes contact mode techniques for conducting force measurements and therefore the focus of this review will be limited to such techniques[84, 85].

AFM can also be used to measure forces, which is described in the next section.

Contact Mode Force Measurement

Probe Characterization

Production of force-separation plots (normalized to a plate-plate interaction) requires knowledge of the geometry of both surfaces and the elastic constant of the cantilever. One of the earliest obstacles for AFM force measurement was the ambiguity of probe geometries. Early treatments of this problem used transmission electron microscopy (TEM) to characterize the tip geometry for normalizing tip-sample interactions. In 1992 Ducker et al. developed a technique in which a spherical colloidal particle is glued to the tip of the cantilever[86] introducing a known geometry. A second advantage of the colloidal probe technique is that there is a simple way to transform the force measured between a sphere and a flat plate, F, to the Energy per unit Area, E_A, which is an intensive (material) property. The transformation is known as the Derjaguin Approximation[87]:

$$F/2\pi R = E_A \tag{7}$$

where R is the radius. The approximation is valid for similar transformations between two crossed cylinders, and a similar approximation applies for two spheres.

For my thesis work, the radius was measured from pictures taken with a digital camera mounted to a 50 times objective. A calibration grating with a known pitch was used to correlate the distance on the image to the actual distance.

Calibration gratings for tip characterization are used to image mounted spheres for artifacts, roughness, and asperities (Figure 8). The roughness of the sphere is determined by calculating the rms displacement of the AFM image.

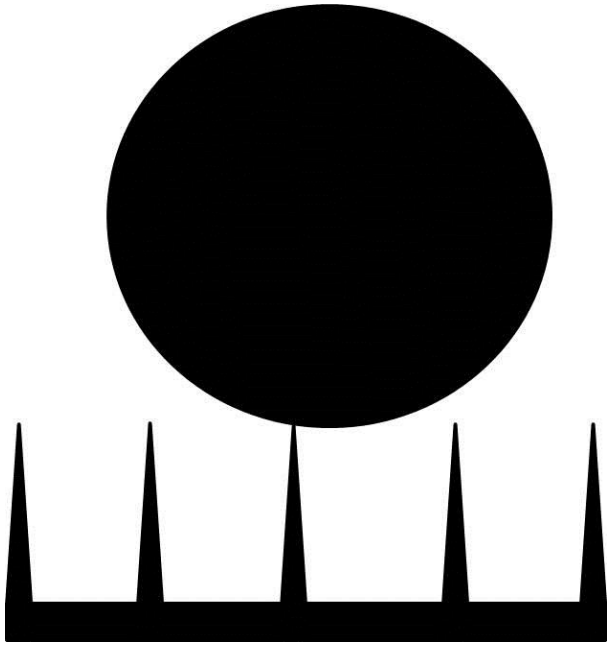

Figure 8: Scanning a sphere-mounted cantilever over a single tip on a characterization grating produces an image of the sphere topography.

Spring Constant Calibration

The force on the sphere is the product of the spring deflection and the spring constant. There are several methods of determining the cantilever spring constant. The thermal noise method, used in this work, is a non-destructive technique developed by Hutter et al.[88] that estimates the spring constant from the power spectral density of the deflection of the cantilever due to thermal fluctuations. When the cantilever is far away from other objects, (> 1 mm) the average energy of the spring is equal to the thermal energy:

$$\frac{1}{2}k\left\langle x^2\right\rangle = \frac{1}{2}k_B T \tag{8}$$

In equation (8) the left-hand side of the expression represents the energy of a cantilever of elastic constant k with mean-square displacement $\langle x^2 \rangle$ and the right-hand side of the expression represents the thermal energy with one degree of freedom at temperature T. k_B is the Boltzmann's constant. This expression is easily manipulated to solve for k (9):

$$k = \frac{k_B T}{\left\langle x^2\right\rangle} \tag{9}$$

The end slope of the cantilever is sampled over a range of frequencies near the resonant frequency of the cantilever and converted to a frequency domain using a Fast Fourier Transform (FFT) to obtain the power spectral density. Background noise, which is usually white and $1/f$ noise, is removed from the spectrum by creating a fit at the resonant peak. Contributions from other oscillatory modes are insignificant. Integrating the power spectrum of the cantilever yields the mean-square displacement of the cantilever due to thermal fluctuations and allows us to determine the elastic constant of the cantilever[88].

Force Curve Analysis

Force-separation curves are produced from deflection data and voltage outputs from the photodiode using a technique developed by Ducker et al.[86]. This technique assumes both the sphere and the plate are rigid, and that the cantilever experiences no surface forces at large separations. At this point it helps to divide deflection-displacement data into regimes (Figure 9).

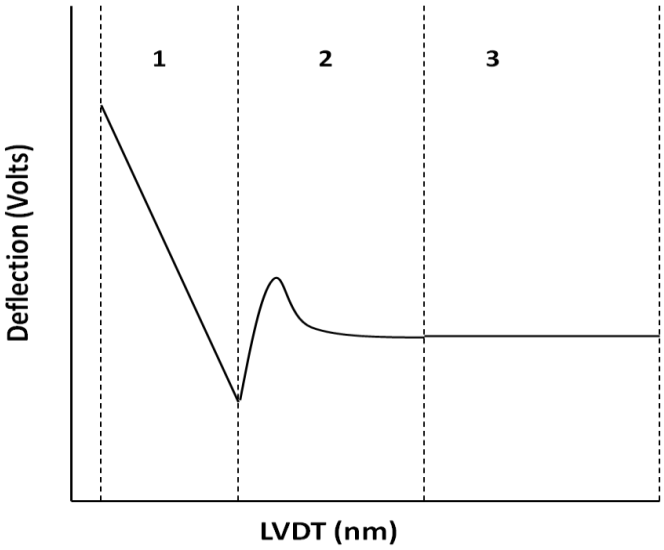

Figure 9: Schematic of the regions of a deflection-displacement curve

Region 1 is the contact, or constant compliance, region. If the sphere rests on the sample, then moving the piezoelectric transducer simply deflects the cantilever spring. Since the cantilever has a constant stiffness, then the deflection should be linear with the LVDT signal. Thus the linear section of Figure 9 is consistent with the sphere resting on the sample, i.e, zero separation. In Region 2, the slope is complicated, which suggests that the stiffness of the system is determined by at least two springs in series: the cantilever and the surface force. Thus Region 2 is the region where the surface forces are measured. Region 3 is the zero-deflection region, where the cantilever is under no influence of surface forces. Region 1 and Region 3 are necessary for the transformation of deflection-displacement to force-separation.

The first obstacle is converting deflection from arbitrary voltage outputs to standardized displacement values (generally nanometers of cantilever deflection). The slope of the

linear region 1, known as the optical-lever sensitivity (OLS), may be determined from the quotient of the change in voltage reading of the photodiode and the piezo displacement:

$$\frac{dD(Volts)}{dL(nm)} = OLS \tag{10}$$

The statement in (10) is only true if both surfaces are rigid. At zero separation, assuming neither the surface nor the sphere deform, the change in deflection of the cantilever D (in units of distance) should be equal in magnitude to the piezo displacement L, or $\frac{dD(nm)}{dL(nm)} = 1$.

Under this constraint, the inverse OLS (InvOLS) may therefore be used to convert voltage output from the photodiode (D(Volts)) to deflection of the cantilever (D(nm)):

$$D(nm) = InvOLS \times D(Volts) \tag{11}$$

The next step is to define zero deflection. As mentioned earlier, Region 3 represents the regime of the curve that is not under any influence of surface forces and therefore is used as zero deflection. This region is fit to a horizontal line which is subtracted from the total force curve so that $F \equiv 0$ at large separations.

Next LVDT displacement is converted to separation. In order to accomplish this separation must be defined in terms of the measured quantities, cantilever deflection and LVDT (12):

$$\Delta H = \Delta L + \Delta D \tag{12}$$

Figure 10 below helps to visualize how separation varies with both LVDT and deflection.

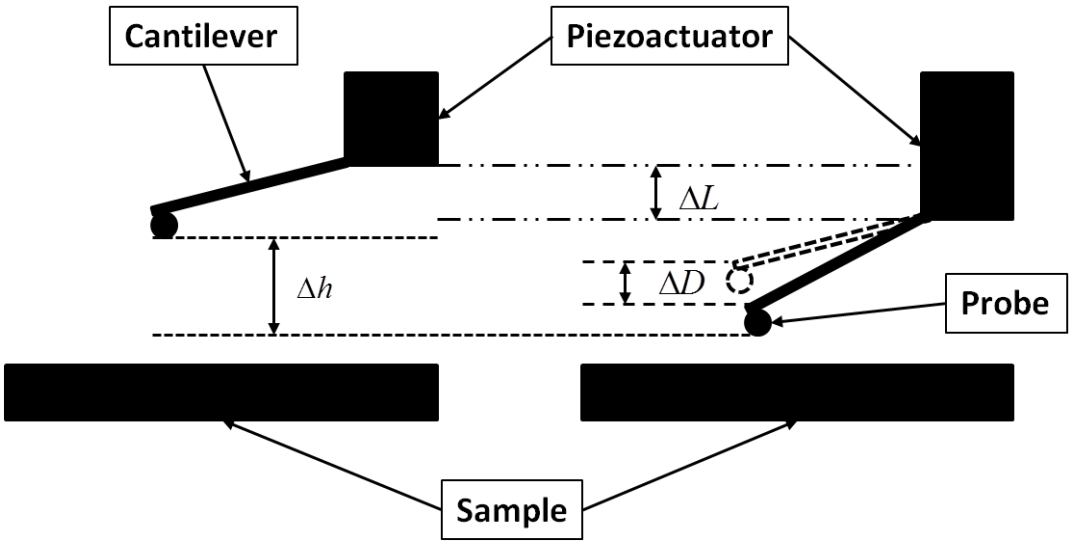

Figure 10: Schematic showing how separation depends on both deflection and the distance moved by the piezoactuator.

This relationship relates the measured quantities of cantilever deflection *D* and LVDT displacement *L* to the separation between the two surfaces *h* (Figure 10). The reference cantilever deflection and LVDT position are arbitrary, so this relationship simplifies (12) so that h may be given in terms the two measured quantities and one unknown constant (13):

$$h = D + L + h_o^{'} \tag{13}$$

The unknown $h_o^{'}$ may be determined from the constraint $h = 0$ in Region 1.

Another important step is the normalization of the force to the radii of curvature for the system using Derjaguin's approximation (7)[87].

Features of a Force Curve

Force curves show how the total force acting between the two surfaces changes with the separation between them. It has been explained how separation and force is determined from deflection-displacement data. A schematic force-separation curve is shown in Figure 11.

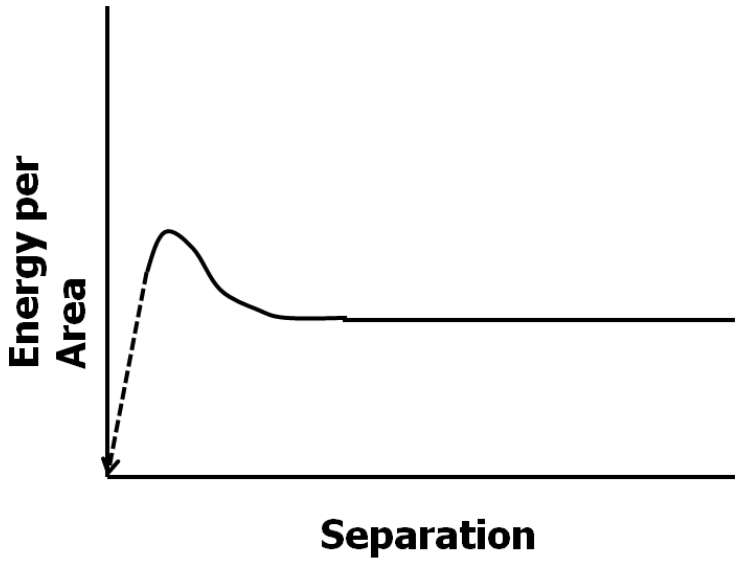

Figure 11: Schematic of a force-separation curve. The solid line represents the region of mechanically stable force measurements while the dashed line represents the region of mechanically unstable data points.

Another very important point to discuss is the concept of mechanical instability on the force curve. Consider the equation of motion:

$$m\ddot{x} + \gamma\dot{x} + kx = F_{surf}(D) \tag{14}$$

$F_{Surface}(D)$ is the surface force at separation D acting on a cantilever of mass m, damping coefficient γ , and spring constant *k* at an acceleration, velocity and deflection of $\ddot{x}, \dot{x}$, and x. A deflection detected by the photodiode may be equated to the surface force when there is mechanical equilibrium, or the first two terms of equation (14) are equal to zero. There are two points that need emphasis: mechanical equilibrium and stability. Mechanical equilibrium is satisfied when there is no net force or torque acting on the body which in this case is the cantilever. However, thermodynamic equilibrium does not exist because the cantilever is being driven toward the surface by the piezo actuator. Regardless, the acceleration and velocity are so small that the first two terms may be neglected. A measurement under these conditions is called quasistatic. Force is defined as the gradient of the potential energy:

$$F = \frac{\partial E}{\partial D} \tag{15}$$

Thus, mechanical equilibrium may also be defined at zero gradient of the potential energy-separation curve. From mathematics it is known that a fixed point (first-derivative equals zero) is stable when the second-derivative is greater than zero:

$$\left(\frac{\partial^2 E}{\partial D^2} = \frac{\partial F}{\partial D} \right) > 0 \tag{16}$$

The total gradient may be rewritten in terms of the gradient of the cantilever force (the elastic constant of the cantilever) and the gradient of the surface force:

$$K - \frac{\partial F_{surf}}{\partial D} > 0 \tag{17}$$

Thus our criterion for stability may be defined as:

$$K > \frac{\partial F_{surf}}{\partial D} \tag{18}$$

Conversely, a mechanical instability will occur when the gradient of an *attractive* $\left({\partial F_{surf}}/{\partial D} > 0 \right)$ surface force is greater than the spring constant of the cantilever.

Understanding mechanical instability is crucial when choosing a cantilever. If the cantilever spring constant is too weak then the cantilever will be unstable at greater separations; if the cantilever is too stiff then the cantilever will lack the sensitivity to measure weak surface forces or forces at larger separations. Clever use of relationship (18) may be used to circumvent these issues, such as those covered in the review of Israelachvili & Pashley[54].

IV. Lifshitz Theory

Background

My goal is to characterize the hydrophobic force, but the AFM experimental technique measures the total force. The basic assumption of my work is that the total (measured) force can be considered as the sum of independent forces. For example:

$$F_{Total} = F_{vdW} + F_{EDL} + F_{Hydrophobic} + F_{Other} \tag{19}$$

where F_{Total} is the total measured force, F_{vdW} is van der Waals force, F_{EDL} is the force due to overlapping electric double-layer, $F_{Hydrophobic}$ is the force caused by the hydrophobicity of the surfaces, and F_{Other} corresponds to all other forces that could act on the surfaces that are not of particular interest for this work, such as viscous forces or cavitation forces. By working in concentrated salt solutions, the electric double-layer can be reduced to insignificance, and by operating at low velocities to reduce hydrodynamic forces and in degassed solution to minimize adsorbed nanobubbles, the total force may be defined in terms of only the ubiquitous van der Waals force and the hydrophobic force:

$$F_{Total} = F_{vdW} + F_{Hydrophobic} \tag{20}$$

Thus, an accurate determination of the hydrophobic force depends on accurate knowledge of van der Waals and other forces. Here I describe how van der Waals forces were calculated.

Van der Waals

Van der Waals forces between individual molecules are well-understood interactions. At any instant in time, a neutral atom will have an instantaneous dipole that will induce a dipole on a neighboring molecule, thus resulting in a net attraction when all configurations are averaged over time. How does the molecular pair-wise interaction translate to the macro-scale many-body interaction?

In 1937, Hamaker published a model for estimating van der Waals forces between macro-scale bodies by summing the pair-wise dipole interactions of all the molecules between the bodies[89]. This approach assumes that each interacting pair acts independent of the surrounding molecules. This is an accurate assumption for dilute gases where the nearest neighboring molecules are very far away, but is erroneous for condensed phases where a pair of interacting molecules are highly influenced by their neighbors. Regardless, the Hamaker model is still useful today as a rough estimate when a Hamaker coefficient can be estimated and a rigorous model is unnecessary.

Lifshitz Theory

By assuming pair-wise additivity, Hamaker theory neglects the fact that every molecule in a material polarizes every other molecule, and therefore each interaction between any two molecules is affected by all other molecules. Unfortunately, it is not possible to directly solve the many-body problem to calculate van der Waals forces starting from the interaction between two molecules. Lifshitz theory is an alternative method for solving van der Waals, based on two things: (1) electromagnetic forces are mediated by photons and

(2) it is relatively easy to measure the interaction between photons and a condensed phase via spectroscopy.

Consider two materials, A and B, separated by medium m. Material A and B are net neutral but because they are made up of moving charges they have an electromagnetic field associated with the configuration of charges throughout the body at any instance in time[90]. These electromagnetic fields propagate through space indefinitely. When these bodies are far apart they cannot feel the field of the other body, but at smaller separations the electromagnetic fields of each material distort each other.

Consider the two molecules discussed before. The configuration of the electrons of molecule A will induce a favorable configuration (one that minimizes the interaction energy between the molecules) on molecule B. An analogy can be drawn to the large bodies discussed here. Material A and B will attempt to increase or decrease their separation from one another such that this distortion minimizes the energy. The driving force for this is the relative difference of their susceptibility to electromagnetic fields, or dielectric response of each material. For material A in medium, m:

$$\bar{\Delta}_{Am} = \frac{\varepsilon_A(i\xi) - \varepsilon_m(i\xi)}{\varepsilon_A(i\xi) + \varepsilon_m(i\xi)} \tag{21}$$

where the dielectric responses, ε_m and ε_A, are both a function of imaginary frequency $i\xi$. Note that the dielectric response is a function of frequency.

The dielectric response can be obtained from the absorption spectrum, including the microwave, infrared, and UV/vis[90]. However, absorption spectra for all but the most

common of materials (ea: mica, gold, water etc.) can only be found for a limited range of the full spectrum. Fortunately the microwave, visible and IR regions contribute very little to the overall interaction for many materials and may often be neglected. Also, the absorption frequencies and oscillator strengths from a limited data set can be used to estimate the full spectrum by fitting to a linear oscillator model. For example, the van der Waals force of most non-polar (low dielectric constant) materials are described very well from the UV region alone[90].

Additionally, the zero frequency term (static polarization) is greatly affected by the addition of salts: it experiences Debye screening similar to the electrostatic double-layer, but with half of the decay length:

$$A_0(\kappa)/A_0(0) \approx (1+2D\kappa)e^{-2D\kappa} \tag{22}$$

where $A_0(\kappa)$ is the zero frequency term for a solution with a Debye parameter of κ, $A_0(0)$ is the zero frequency term of the pure liquid, and D is separation.

Determination of Parameters from Absorption Data

Hough & White simplified the modeling process by estimating parameters for the UV region based on refractive-index vs frequency data in the visible region using a Cauchy plot[91]. The UV regime may be constructed from visible spectral data assuming that the UV absorption has only one important relaxation peak. The dielectric response function for imaginary frequencies may be written as:

$$\varepsilon(i\xi) = 1 + \frac{C_{UV}}{1 + \left(\xi / \omega_{UV} \right)^2} \tag{23}$$

where C_{UV} is the oscillator strength and ω_{UV} is the absorption frequency. However, absorption data is not measured in imaginary frequencies so the Kramers-Kronig relation is used to transform (23) to the real frequency regime:

$$\varepsilon'(\omega) = \varepsilon(\omega) = n^2(\omega) = 1 + \frac{C_{UV}}{1 - \left(\omega / \omega_{UV} \right)^2} \tag{24}$$

Where $n(\omega)$ is the refractive index in the visible spectra. Equation (24) may be manipulated to a linear form:

$$\left(n^2 - 1\right) = \left(n^2 - 1\right)\frac{\omega^2}{\omega_{UV}^2} + C_{UV} \tag{25}$$

The two parameters for the dielectric response are easily obtained from the slope and y-intercept:

$$\begin{aligned} \omega_{UV} &= 1/\sqrt{m} \\ C_{UV} &= n^2 - 1 \end{aligned} \tag{26}$$

In this work, it was necessary to accurately estimate the van der Waals force in concentrated salt solution, so I measured the refractive index of salt solutions, and made a Cauchy plot to determine the oscillator strength and resonant frequency for use in van der Waals calculations. This plot is shown in Figure 12.

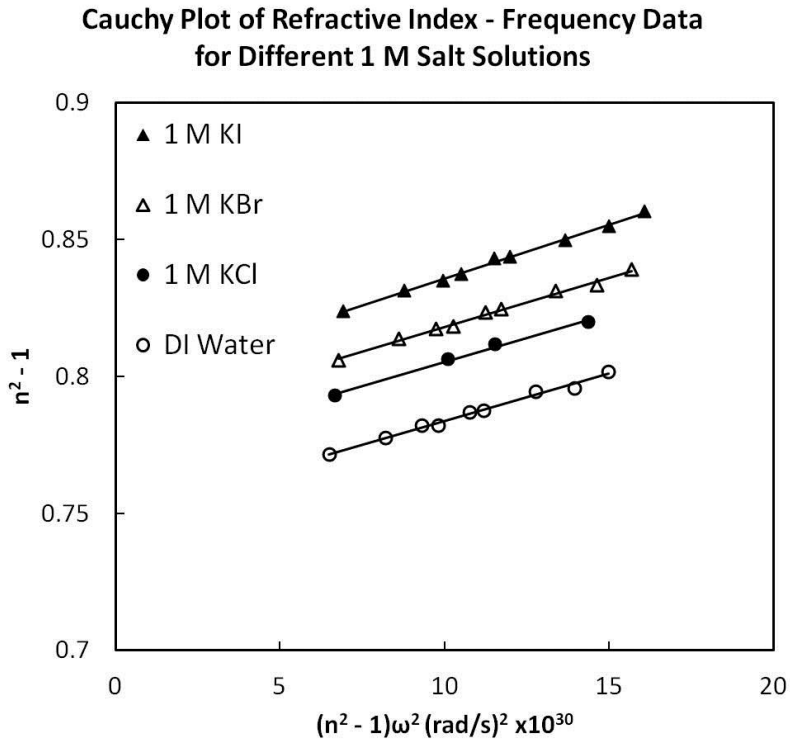

Figure 12: Cauchy plot demonstrating the effect different dissolved salts have on the spectral properties of water. Note that only the intercept (oscillator strength) varies with added solute.

The oscillator strength C_{UV} may be estimated to equal the difference between the dielectric responses at frequencies in the visible region (n^2) and the far ultraviolet region (~ 1).

Parsegian also provides methods for predicting data if none is available. The ionization potential multiplied by the energy of a single electron may be used to estimate the absorption frequency ω_{UV} while oscillator strength C_{UV} may be estimated as n^2-1 where the refractive index n is for low frequencies[90].

Note that it is not the dielectric response of a particular material but rather the differences in the dielectric responses of each of the materials that dictate the strength of the

interaction. However, these parameters alone tell very little about the final interaction. These parameters must be used in Lifshitz model to determine the interaction energy per area.

Layered Bodies

Surfaces are often hydrophobized by adsorption of a thin layer of organic material. Consider Figure 13 where there is a thin coating of material A_1 covering substrate A with a thickness of a_1. At separation l is much greater than the thickness of A_1 $\left(l \gg a_1\right)$ the thin coatings are effectively invisible with respect to the overall interaction. The reason for this is that contributions from the layers decay at a rate relative to the ratio of the layer thickness and the separation. Thus as the materials approach one another $\left(l \to a_1\right)$ the contributions from the layer become more significant until they eventually dominate near contact $\left(l \to 0\right)$.

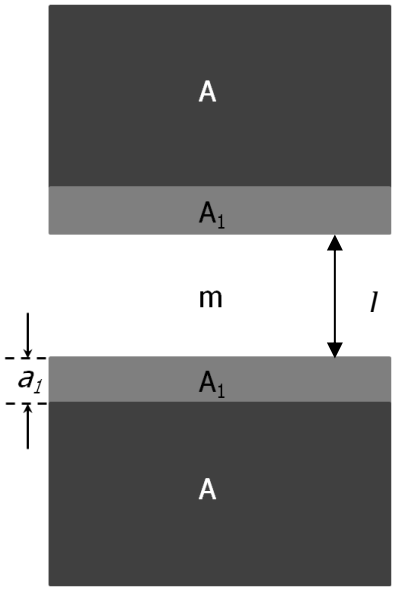

Figure 13: Schematic of two half-spaces of material *A* coated with a layer of material A_1 of thickness a_1 and separated by a distance of *l* with an intervening medium *m*.

The main complication that arises here is not so much in the increased complexity of the model but rather the increased uncertainty in the measurement of the layer thickness that is required as an input to the calculation.

V. Effect of Temperature on the Hydrophobic Force

Introduction

Here I describe what I believe to be the first force measurements between hydrophobic surfaces that (a) show a net attractive force in a quasi-static measurement, and (b) are uncomplicated by estimates of forces other than the ubiquitous van der Waals force. This work has been published as Mastropietro and Ducker, 2012 in Physical Review Letters[92]. Our selected system consists of smooth borosilicate-glass solids coated in polymerized octadecyltrichlorosilane (OTS) that are immersed in degassed aqueous 1 M roasted KCl solution. The salt screens electrostatic forces, the degassing minimizes bubble formation, and the system has weak van der Waals forces so that hydrophobic forces are more easily discerned. Together, these conditions combine to enable us to measure the hydrophobic force in the absence of larger interactions. However, it is important to note that the addition of salt may affect the force, so the results may not apply to all other salt concentrations. In 1 M KCl there are approximately 55 water molecules for each KCl ion pair. In the next chapter I describe measurements in lower salt concentrations.

As mentioned earlier, estimation of the hydrophobic force relies on accurate estimation of the van der Waals forces. I calculated theoretical van der Waals interactions per unit area for the planar 5-layer glass–OTS–aqueous salt–OTS–glass system using Lifshitz theory[90] (see Fig. 1).

The effect of screening on the zero frequency term was accounted for using Equation (22). Microwave and UV absorption data for water were found in Parsegian[90]. However, the addition of salt also affects the UV absorption spectrum for water.

Cauchy plots were used to determine UV absorption parameters for 1 M KCl solutions. Figure 12 shows Cauchy plots for deionized water and 1 M solutions of KCl, KBr, and KI. Absorption data was measured using an Abbe 60/ED refractometer (Bellingham+Stanley, United Kingdom) to measure the refractive index of each solution for wave lengths from 450–625 nm. Ultraviolet absorption parameters C_{UV} and ω_{UV} for BK7 borosilicate glass were approximated using "Cauchy plots" as outlined in Hough & White[91]. Coefficients for borosilicate crown glass (BK7)[93] [94] were used with Sellmeier's equation for creating the Cauchy plots. Although the plots show significant differences in different salts, these cause only small changes in the calculated van der Waals force. Spectral data for OTS were not available in the literature, so I considered using spectral properties of octadecane (the alkane portion of OTS), but these also could not be located. So absorption parameters for hexadecane were used in the modeling[91]; I assumed that the dielectric properties of the OTS film were approximated by alkane. Clearly the length of the chain varies between 16 and 18 carbon atoms, but this is accounted for in the thickness of the layer, it is unlikely that the absorption spectrum changes greatly.

The actual film thickness was measured using ellipsometry and found to be 2.7 nm., so the force was calculated for a 2.7 nm layer of hexadecane on glass as shown in Figure 14. The main point is that the force is very small, much smaller than the hydrophobic force originally measured by Pashley and Israelachvili, and thus there is only a small

"background" force on which the hydorophobic force must be measured. Furthermore, the force is even small for a van der Waals force. To examine the effect of the alkane chain length, I also calculated the force using the dielectric properties of tetradecane, and found negligible difference.) More significant errors in the calculated van der Waals force arise from errors in the thickness of the film, and properties of the glass. Figure 14 shows a range of calculations of the van der Waals force. First, the extreme limits of zero alkane thickness and infinite thickness shows that the hydrocarbon film make a difference of about 50%, but still the force is small. Second, a change in composition from glass to fused silica also makes a significant difference but the force remains small.

Finally, the effect of temperature was investigated. In this calculation, I ignored the effect of temperature on the dielectric properties; however, absolute temperature does appear in the Lifshitz calculation for van der Waals (26):

$$G_{AA_1mA_1A}(l;a_1) = \frac{k_B T}{8\pi l^2} \sum_{n=0}^{\infty}{}' \int_{r_n}^{\infty} x \ln\left[\left(1-\left(\bar{\Delta}_{Am}^{eff}\right)^2 e^{-x}\right)\right] dx \qquad (26)$$

$G_{AA_1mA_1A}(l;a_1)$ is the interaction energy per unit area between two materials at separation l where A is the substrate, m is the medium, A_1 is the layered coating and a_1 is the thickness of the layer. In the integral, r_n is the ratio between the time required for an electromagnetic wave to travel between the two materials and the characteristic time of the frequency being sampled. The components of the wave vector are contained in the x term while the dielectric permittivities of the materials are contained in the $\bar{\Delta}_{Am}^{eff}$ term. The ' in the summation means that the first term (n=0) is multiplied by ½. The sampled frequencies ξ_n

correspond to those where the thermal fluctuations k_BT are proportional to the energy of a photon:

$$\hbar\xi_n = 2\pi k_B T n \tag{27}$$

Where $\hbar$ is Planck's constant. From equation (26) it would appear that van der Waals increasing linearly with absolute temperature; however this temperature term is deceiving. The summation term can be approximated to an integral of *n*:

$$\sum_{n=0}^{\infty}{}' = \int_0^{\infty} dn \tag{28}$$

Solving equation (27) in terms of *n* and differentiating reveals that the summation is inversely proportional to temperature:

$$dn = \frac{\hbar}{2\pi k_B T} d\xi_n \tag{29}$$

A comparison of equation (26) and equation (29) shows that there is no temperature dependence. In summary, the van der Waals forces are weak compared to prior measurements of the hydrophobic force and , independent of temperature, whereas the hydrophobic effect depends on the temperature.

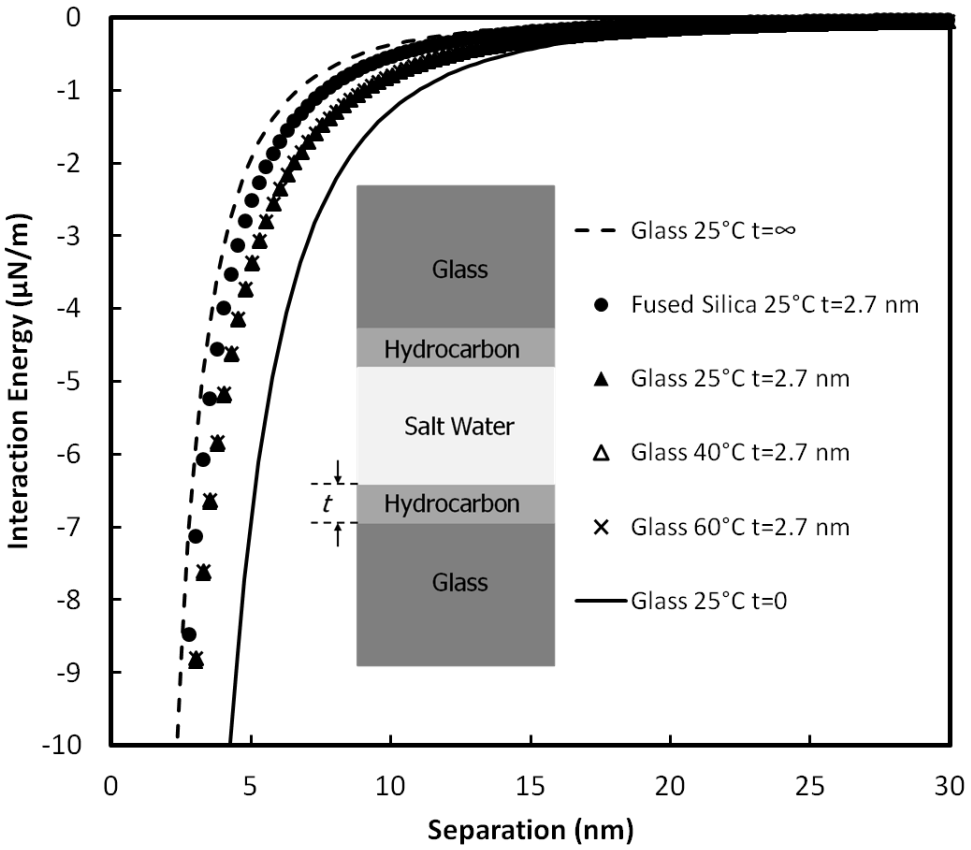

Figure 14: Lifshitz calculation for van der Waals interactions between two semi-infinite half spaces coated in a layer of hexadecane, thickness *t*, across 1 M aqueous salt solutions. The hexadecane is our model compound for OTS. The hydrocarbon film weakens the interactions. Variations in interaction energy with temperature are small.

Experimental

Force-Distance data was obtained from measurements using an MFP-3D atomic force microscope (Asylum Research, Santa Barbara), which measures cantilever deflection (and thus force) as a function of displacement by a piezoelectric translation device at a rate of 50 kHz. Forces were measured between a 20-μm glass sphere and a glass plate, each coated with a self-assembled monolayer of octadecyltrichlorosilane (OTS) in a large reservoir (~ 2 mL) of 1.0 M KCl. During measurement, the volume of the chamber decreases by about 10^{-6} mL for every nm decrease in separation, but the presence of air in the chamber limits the increase in pressure. In any case, the seal on the chamber allows the exit of air when the pressure is a little over 1 atm. Force-separation plots were obtained using the analysis method outlined in Ducker et. al.[86, 95] with the following variations: (1) the translation was measured using a linear variable differential translation sensor (LVDT) and (2) virtual deflection was removed from the raw deflection voltage – LVDT signal.[96] There was negligible effect of the virtual deflection correction because the LVDT range was so small. The stiffness of each cantilever was measured by the thermal method,[88] and ranged from 0.49–0.77 N/m.

Aqueous salt solutions were prepared by combining Milli-Q water with roasted KCl, and degassed by three freeze-pump (~0.1 mmHg)-thaw cycles. Degassed solutions were used to decrease the likelihood of nanobubble nucleation at the solid-liquid interface. Glass spheres were purchased from Duke Scientific Corporation and glass plates were Fischer Finest coverslips. Well-anchored OTS monolayers were used to produce hydrophobic solids. OTS coatings were prepared by submerging O_2-plasma (250 mTorr, 2 min, 100 W)

treated glass plates or cantilevers with mounted spheres in 3–5 mM OTS in hexadecane solutions overnight (~15 hours). OTS-coated films were dipped in fresh chloroform to remove excess solvent and unattached OTS to produce smooth, uniform monolayers free of asperities. AFM contact mode images of a typical OTS-coated glass plate are shown in Figure 15. OTS monolayers prepared in this manner were found to have advancing angles of 108° and receding contact angles of 95° in 1.0 M KCl solution and angles of 107° and 95° in pure water. Contact mode AFM scans showed an RMS roughness of <0.5 nm for plates over 20 μm^2 and <1.0 nm for spheres over 1 μm^2, while ellipsometry measured a thickness of approximately 2.7 nm, assuming a dielectric constant of 2.40 at 633 nm for the hydrocarbon layer.

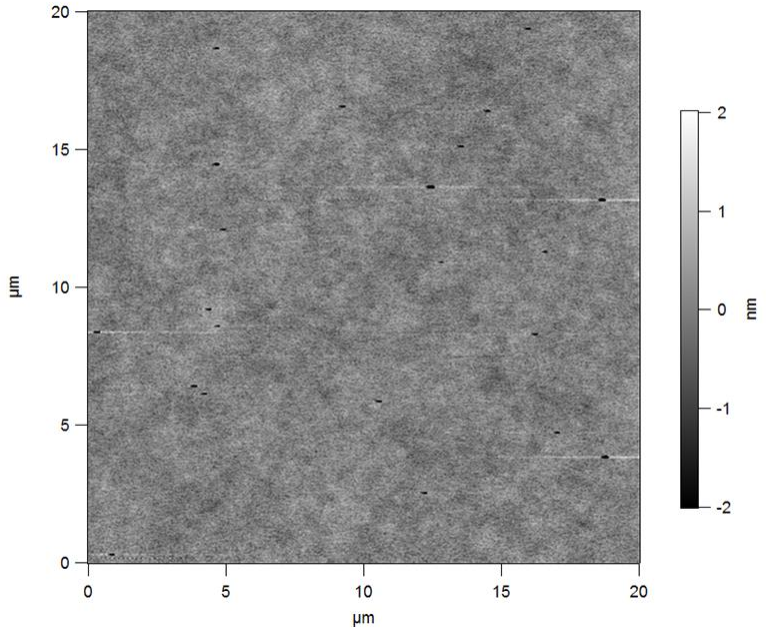

Figure 15: Contact mode AFM image of a typical OTS-coated glass plate

The Total Force Between Hydrophobic Surfaces is Not Temperature Dependent

Surface force measurements show the attractive force between the hydrophobic surfaces (Figure 16). The measurements are noisy because thermal noise is similar in amplitude to the DC force for separations greater than about 10 nm. A 101-point average (2 ms) removes much of the noise and reveals the net attraction at separations less than about 12 nm; this averaged curve is labeled "smoothed" in Figure 15. When the gradient of the surface force exceeds the spring constant, the sphere position is mechanically unstable. This occurs at about 6 nm in Figure 16, and it is not possible to make equilibrium measurements at smaller separations.

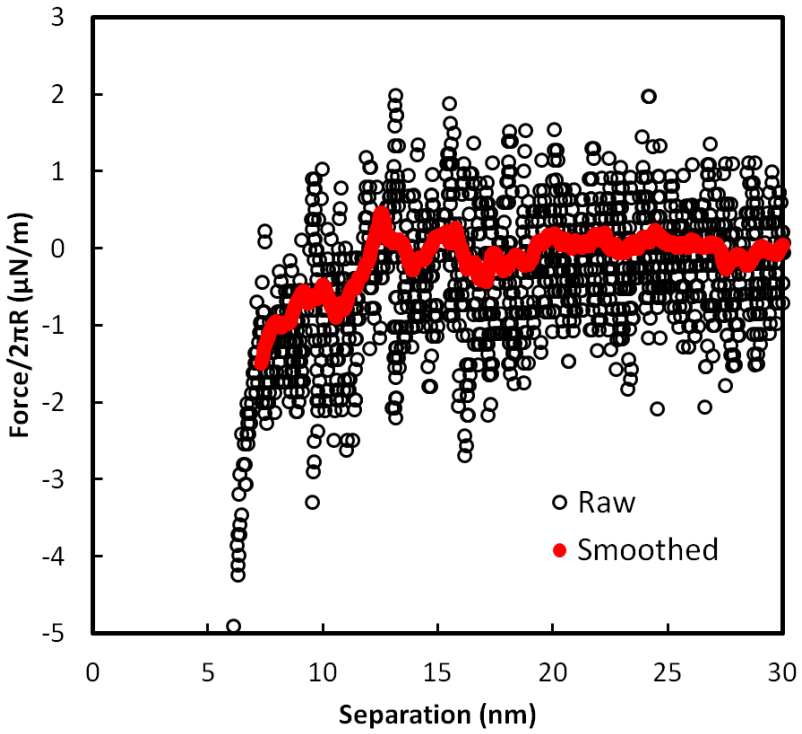

Figure 16: Measured force vs separation for OTS-coated borosilicate glass interacting across aqueous 1.0 M KCl solution. The force has been normalized by $2\pi R$, which for a sphere-plate geometry is equal to the energy per unit area for flat plates (the Derjaguin approximation)[97]. Open circles show measured points at separations greater than the point of mechanical instability for the sphere (which occurs when the gradient of the attractive force equals the spring constant). The red (filled) circles represent smoothed data: the raw deflection data was smoothed using a 101-point moving average before conversion to force-distance. The smoothed curve was truncated 50 points (~0.50 nm) before the mechanical instability so that data from the instability is not included in the smoothing. In this data the mechanical instability occurred at about 6 nm, and in a series of repeat runs, instabilities occurred at 8.5 nm, 10.9 nm, 6.5 nm, 6.7 nm, 7.5 nm, 6.8 nm, 6.2 nm, 6.2 nm, 6.7 nm, and 7.0 nm.

Figure 17 shows results in which data from several runs are averaged into 0.5 nm bins to reduce noise. Results for two different experiments are shown. At small separations (<6 nm) there are too few data points for averaging and the gradient is large, so individual measurements are shown. This averaged data is shown together with the calculated van der Waals force from Figure 1 for the 2.7 nm hydrocarbon film. Extreme limits of the calculated force for zero and infinite thickness films are also shown.

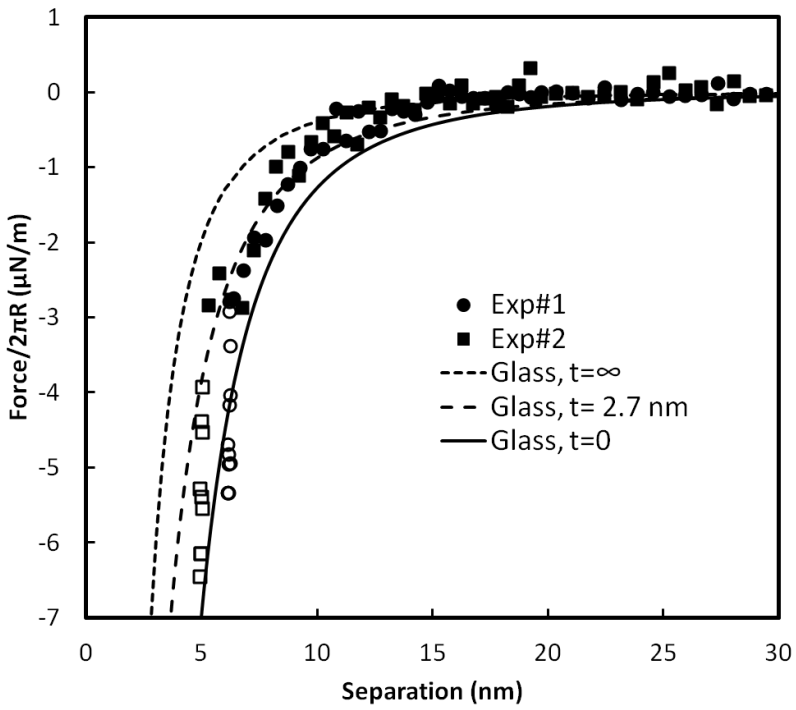

Figure 17: Comparison between measured forces and Lifshitz calculation for borosilicate glass coated in OTS immersed in 1 M aqueous salt at 23°C. Circles and Squares represent data from different experiments. Lifshitz calculations represent the limiting cases of infinite and zero hydrocarbon thickness as well as the measured thickness of 2.7 nm. Closed symbols represent data averaged from several force runs. The random error in the force is about ±0.06 μN/m (i.e. about the point size) and in separation is ±0.1 nm. There is a systematic error of ±20% in the force arising from errors in the spring constant, the radius and the calibration of the spring deflection ("invols"). At small separations, there are fewer data points, so the data is not averaged. These unaveraged data points are shown as open symbols. The measured interactions agree with the calculated van der Waals interaction at separation greater than about 6 nm. Comparison at smaller separations is difficult because there are fewer measured points and greater error in the theoretical force.

The measured force agrees very well with the Lifshitz calculation for separations greater than 6 nm. From 5–6 nm the fit is worse, but also the error is greater for both the Lifshitz theory (large effect of material properties and thickness) and the measured force (few measured points). Note also that there is a significant error in determining the zero of separation for the theory and the experiment. The theory assumes a mathematical plane between layers whereas the real materials have combined rms roughness of 1.5 nm. In addition, the systematic error in determining the measured zero of separation is about 1 nm in our experiments. (Note the ~ 1 nm shift in the data between two experiments with different spheres and plates that could be due to a single extra 1 nm asperity on one surface.) Implementation of the theory also has some error because we used incomplete optical data. Considering these errors, the agreement between van der Waals force and measurement in the range 6–∞ nm is good. Given the good agreement, it seems unnecessary at this point to invoke the existence of an additional theoretical force to describe the results. In other words, the hydrophobic force in 1.0 M salt at separations greater than 6 nm is zero.

The functional form and magnitude of the measured force suggest that the force can be explained entirely in terms of Lifshitz theory. Another approach to understanding the force between hydrophobic surfaces is to examine its dependence on temperature. The term "hydrophobicity" is usually associated with an increase in entropy arising from changes in water structure. The entropic contribution to the attractive force can be extracted from measurements of force as a function of temperature at fixed separation, D, and pressure, P:

$$\left(\frac{\partial \Delta G}{\partial T}\right)_{D,P} = -\Delta S \tag{30}$$

where ΔG is the difference between the Gibbs free energy of the film at separation, D, and infinity and ΔS is the difference in the entropy of the film at separation D and infinity.

Forces between hydrophobic solids in 1.0 M KCl as a function of temperature are shown in Figure 18. We cannot resolve differences in force over the range 23–60° C and therefore we conclude that the entropic contributions are a very small contribution to the total interaction. Thus it is difficult to associate the measured force with changes in water structure as a film thins.

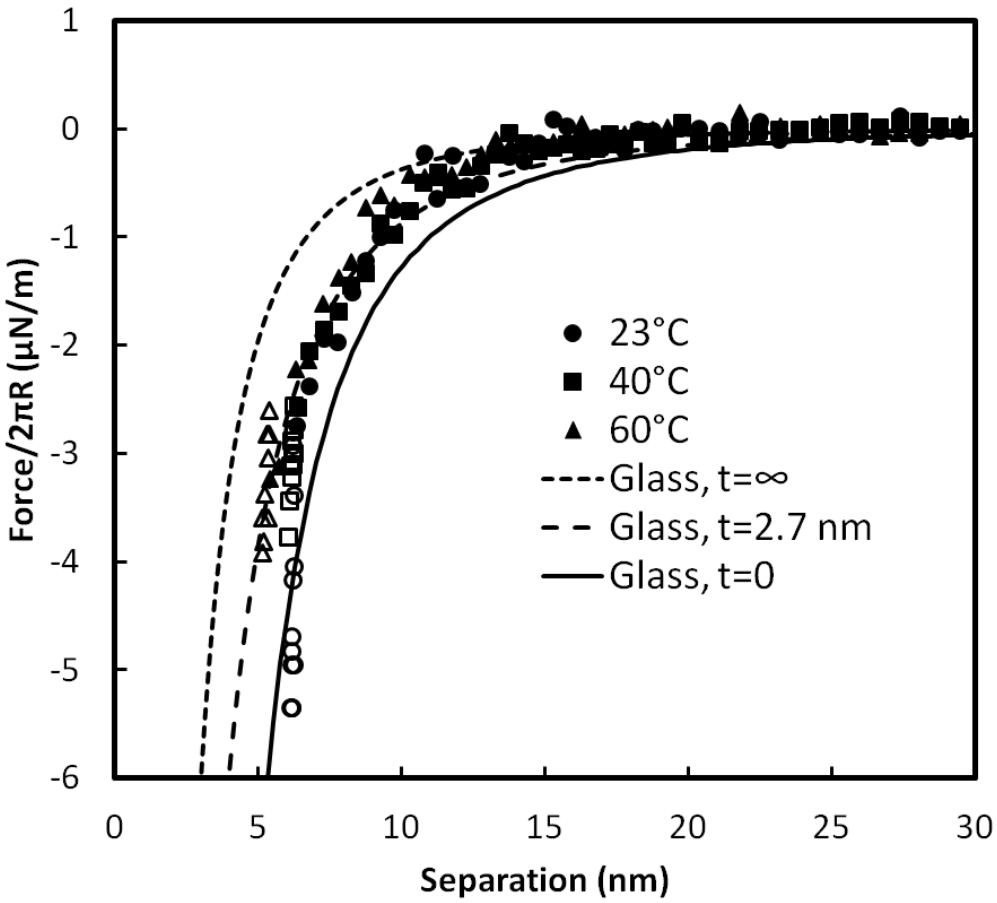

Figure 18: Force as a function of temperature for OTS-coated borosilicate glass interacting across 1.0 M KCl. The measurements cannot resolve differences as a function of temperature. Lifshitz calculations represent the limiting cases of infinite and zero hydrocarbon thickness as well as the measured thickness of 2.7 nm. Filled markers represent averaged data points while open markers represent single measured data points.

In contrast to measurements at separations greater than 5 nm, measurements of the pull-off force (force to separate surfaces from contact) do show a small temperature dependence, as shown in Table 1. The force decreases with temperature, as expected for an entropic force which is consistent with the origin of the hydrophobic interaction, and is much stronger than predicted by Lifshitz theory. Note that there is a very large error associated with Lifshitz theory because (a) our implementation does not account for film roughness and (b) uncertainty in how to treat van der Waals forces at small separations[98]. JKR theory can be used to estimate the solid–liquid surface tension, which is about 20 mJm^{-2}. This is lower than expected for a hydrocarbon–water interface ($\sim$ 50 mJm^{-2}), but not surprising for surfaces with nanometer-scale roughness.

Table 1: Pull-off Force

Temperature °C	Energy per Area+ (mJ/m^2)	Liftshitz Energy* (s=1.0 nm) (mJ/m^2)	Liftshitz Energy* (s=0.5 nm) (mJ/m^2)	γ_{SL} (JKR)++ (mJ/m^2)
23	37.1±0.6	0.07	0.30	24.7±0.4
40	34.9±0.2	0.07	0.30	23.2±0.2
60	30.5±0.2	0.07	0.30	20.3±0.1

+ calculated from $F/2\pi R$

++From JKR theory from $\gamma_{SL} = F/3\pi R$. [99]

*Lifshitz energy is the energy for two surfaces

Simulation suggests that capillary evaporation should occur between hydrophobic plates at small separation,[80] and the instabilities that we measure are at about the same separation

as predicted by simulation (~ 6 nm). Mechanical instabilities begin when the gradient of the surface force exceeds the spring constant. The gradient of the force at separations slightly greater than the instability are very similar to the spring constant so it is not obvious whether the instability is caused simply by the local van der Waals force, or by a dewetting transition. We note that as the gradient of the surface force approaches the spring constant, the net gradient in force approaches zero and thermally-driven fluctuations in sphere position rise rapidly in magnitude even in the absence of a dewetting transition.

Conclusion of Temperature Effects

In conclusion, the measured force between smooth hydrophobic solids (θ_{adv} = 108°, θ_{rec} = 95°) in degassed concentrated aqueous salt solution (1 M KCl) agrees with the van der Waals force calculated from Lifshitz theory for separations greater than 5 nm. Measurements at smaller separations were complicated by mechanical instabilities in the spring so are not discussed here. The good agreement between the measured force and the calculated van der Waals force renders it unnecessary to invoke the existence of a long-range "hydrophobic force" that extends beyond 5 nm in concentrated salt solution. Furthermore, the lack of measurable variation in the force with temperature in the range 25–60° C is consistent with an enthalpic force, and at odds with customary descriptions of hydrophobicity that are based on changes in water structure.

Compared to measurements in pure water, the measurements in salt (1M KCl) have relevance to interactions in sea water (~0.5 M Cl^-) and biological conditions (~0.15 M Cl^-),

and also screens electrostatic forces, thereby removing ambiguity in whether to attribute forces to water-structural or electrostatic origins. The addition of salt and the removal of gas may affect water structure, so these results cannot be used to exclude the possibility that a long-range hydrophobic force does exist in pure water with an equilibrium concentration of dissolved gas. However, arguments for a long range force in water would need to be based on differences in water structure that occur as a result of dissolved salt or gas.

Significance of this Work

There are few examples reported in literature of hydrophobic forces in the absence of nanobubbles and mobile surface groups and even fewer that do not have other large forces that complicate analysis when the force must be estimated and removed. The work presented here is probably the "clearest" measurement of forces between hydrophobic forces in the sense that it has the fewest interfering phenomenon. The very good agreement with the van der Waals force shows that in this particular case, there is no need to invoke a hydrophobic force for separations greater than 5 nm, which calls into question whether a long-range hydrophobic force exists at all. Such a force would now need to be shown to depend strongly on the salt concentration.

VI. Effect of Salt Concentration on the Hydrophobic Force

Introduction

My work described in Chapter V shows that a hydrophobic force has a range of less than 6 nm in concentrated salt solution. It is still possible that the hydrophobic force is somehow mediated by the salt concentration, and that it only exists in dilute salt solution. The purpose of this chapter is to determine the magnitude in salt solution.

Experimental

Preparation of Colloidal Probes

Colloidal glass particles (Duke Scientific) were mounted on ORC-8 cantilevers using a custom built colloidal probe mount. Glass particles and Epikote 1004F (Hexion Specialty Chemicals) epoxy were dispersed on separate sheets of freshly cleaved mica. A 50x objective (Mitutoyo) was used to position the cantilever and to select colloidal particles. Colloidal probes were dipped in deionized water and inspected under an optical microscope to ensure the spheres were properly adhered to the cantilever.

Preparation of OTS-coated Glass Plates

Fisher Finest glass coverslips (Fisher Scientific) were rinsed with absolute ethanol and Milipore water and dried with a stream of ultra-high purity nitrogen. Glass substrates were placed in a Plasma Prep III Solid State (SPI) and treated with O_2 plasma at 100 Watts for 2 minutes. Substrates were placed overnight in a 5 mM solution of octadecyltrichlorosilane

(OTS) (Sigma-Aldrich) in hexadecane (Alfa-Aesar). Substrates were removed and sonicated twice for 15 minutes in chloroform, or pentane, followed by rinsing with absolute ethanol and Milipore water and drying with ultra-high purity nitrogen.

Preparation of OTS-coated Glass Spheres

Colloidal probes were placed in a Plasma Prep III Solid State and treated with O_2 plasma at 100 Watts for 2 minutes. Probes were placed overnight in a 5 mM solution of OTS in hexadecane. Probes were removed and dipped twice in fresh chloroform, or pentane, followed by ethanol, and Milipore water and allowed to dry in a laminar flow cabinet.

Preparation of Solutions

Potassium chloride was roasted at 500° C for 4 hours to oxidize organic contamination into gaseous componenets. Solutions were prepared with Milipore water in volumetric flasks and transferred to a Schlenk flask for degassing. Dissolved gas was removed by freeze-pump-thaw (two cycle minimum). Frozen solutions were pumped for approximately 15 minutes before starting the thaw step. Solutions were used within two days of degassing.

Goniometry

Advancing and receding contact angles were measured on hydrophobized planar glass substrates. Measurements were taken at least three times at different locations on a given substrate. Both pristine surfaces and those used in experiments were used to check if values were affected by probing. Advancing contact angles for OTS-coated surfaces were 109.1±1.2° and receding contact angles were 91.8±0.8°. These values were obtained from

samples from five separate experiments. Measurements from pristine samples and those taken after an AFM experiment showed little difference in advancing contact angle, but in some cases the receding angle was lower after an AFM experiment. We found no significant difference in contact angle for different salt concentrations.

Surface Imaaging

OTS-coated borosilicate glass substrates and probes were imaged in air using an MFP-3D or Cypher AFM (Asylum Research) to ensure smooth, uniform monolayers were present before use in experiments. Probes were imaged using an inverted tip grating (TGT01, NT-MDT). Planar surfaces generally had a rms roughness less than 400 pm for a 20x20 μm^2 while probes generally had a rms roughness of no more than 1 nm for a 1x1 μm^2 region at the apex.

Cantilever Calibration

Cantilever spring constants were obtained using the thermal noise method[100]. The ORC8 cantilevers (k_{nom}=0.71 N/m) used in these experiments were found to have spring constants falling between 0.5–0.75 N/m.

Atomic Force Microscopy

The OTS coated cantilever and glass substrate were loaded into a closed fluid cell for an MFP-3D AFM (Asylum Research). For a typical experiment, the feedback loop would be engaged and the surfaces would be brought into contact before proceeding with the experiment.

For experiments aimed at studying the force when no prior contact is made between the surfaces, the cantilever was moved to approximately 250–500 μm of separation from the plate and force curves were taken over the full range of the z-piezo, moving the head downward in 10 μm increments between each curve. This process was repeated until the first contact force curve was measured. Subsequent force curves were taken for comparison.

DLVO Predictions

Lifshitz theory is required to accurately predict the van der Waals force for complicated systems, such the OTS-coated surfaces presented in this work. Lifshitz theory requires absorption spectra of each material in order to compute the van der Waals force. It has been shown that, for most substances, only the ultra-violet regime of the absorption is necessary for an accurate calculation, which is easily obtained from literature, empirical formulae or refractive index measurements[91].

The glass substrates were modeled as BK7 crown glass. Refractive index and frequency were obtained from the Sellmeier equation and used to determine the absorption frequency and oscillator strength using a Cauchy plot. The OTS monolayers were assumed to have optical properties similar to hexadecane[91]. The absorption parameters for the aqueous salt solutions were modeled as pure water with a damped-oscillator form[90], however, the effect of ionic screening of the zero frequency term was accounted for with the following relationship[90]:

$$A_0(\kappa)/A_0(0) = (1+2D\kappa)e^{-2D\kappa} \tag{31}$$

Where A_0 is the zero frequency term, D is the separation, and κ^{-1} is the Debye length. Lifshitz theory was then used to produce an array of Hamaker coefficients for separations from 0.0001–50 nm at ~0.25 nm increments. This matrix of separations and Hamaker coefficients was used to produce the predicted van der Waals force:

$$E_A(D) = \frac{-A(D)}{12\pi D^2} \tag{32}$$

Where E_A is the energy between two planar plates and $A(D)$ is the Hamaker coefficient at a separation D between the two plates.

Debye-Hückel theory was used to model the electrostatic double layer for the system:

$$E_A(D) = 2\varepsilon\varepsilon_o\kappa(\psi_o)^2 e^{-D\kappa} \tag{33}$$

Where ε is the relative permittivity, ε_o is the permittivity of a vacuum, and ψ_o is the electrostatic surface potential. This is a low potential approximation. Literature values of 60 mV at pH 6 and 10 mV at pH 2 were used for the surface potential for this estimate[101].

Force Analysis

Force vs separation curves were obtained by converting deflection vs displacement data through the procedure presented by Ducker et al.[86]. Poor determination of the constant compliance region can produce error in both the calculation of the force (improper InvOLS) and in the location of zero separation. Constant compliance is the region where the deflection of the cantilever is equal to the displacement of the z-piezo, which by definition will be linear; however, not all linear regions represent constant compliance[102]. For

example, some experiments we found two linear regions on the deflection vs displacement curves. I conclused that the second (higher load) linear region was caused by the sliding of the colloidal probe across the planar substrate[103] after a critical load was exceeded (Figure 19). When the sphere slides along the surface, the deflction of the cantilever per unit of LVDT is lower. For cases with two linear sections, the first linear region was used to calibrate the cantilever deflection in units of nanometers..

An eighty-point moving average was used to reduce the total number of points on individual curves. This was done purely for visual clarity when plotting multiple curves on an individual plot. Averages were plotted with the original data to ensure they gave an accurate representation of the original force curve (Figure 20).

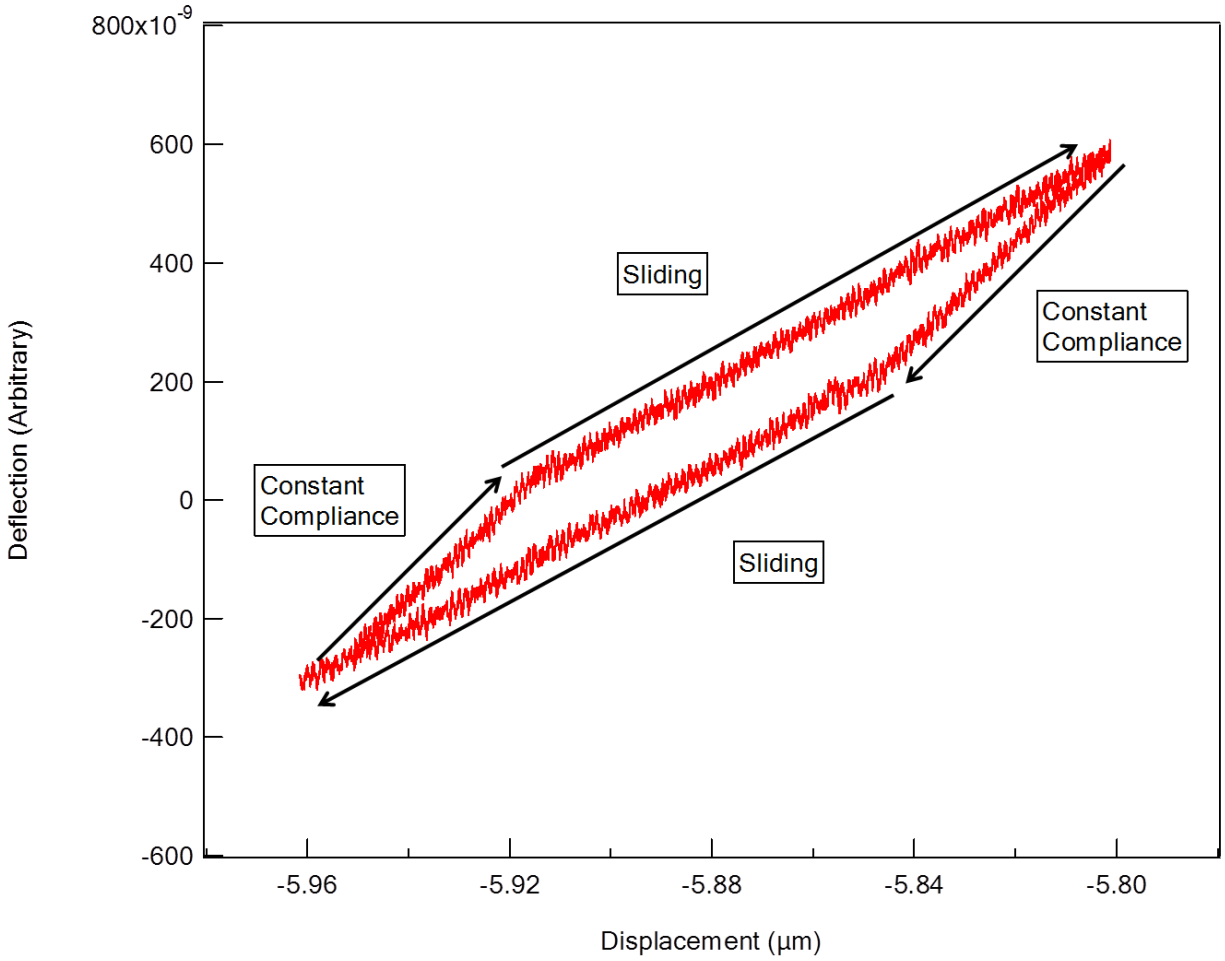

Figure 19: Displacement vs deflection of an OTS-coated sphere and plate. Data was collected at 25 kHz at an approach/withdraw velocity of 20 nm/s. Contact was established prior to friction force measurement. The first linear-region (constant compliance) extends roughly 40 nm on both the approach and the withdraw. After the applied force overcomes the static friction force the probe slides across the surface manifesting as a change in the slope of the linear-compliance region.

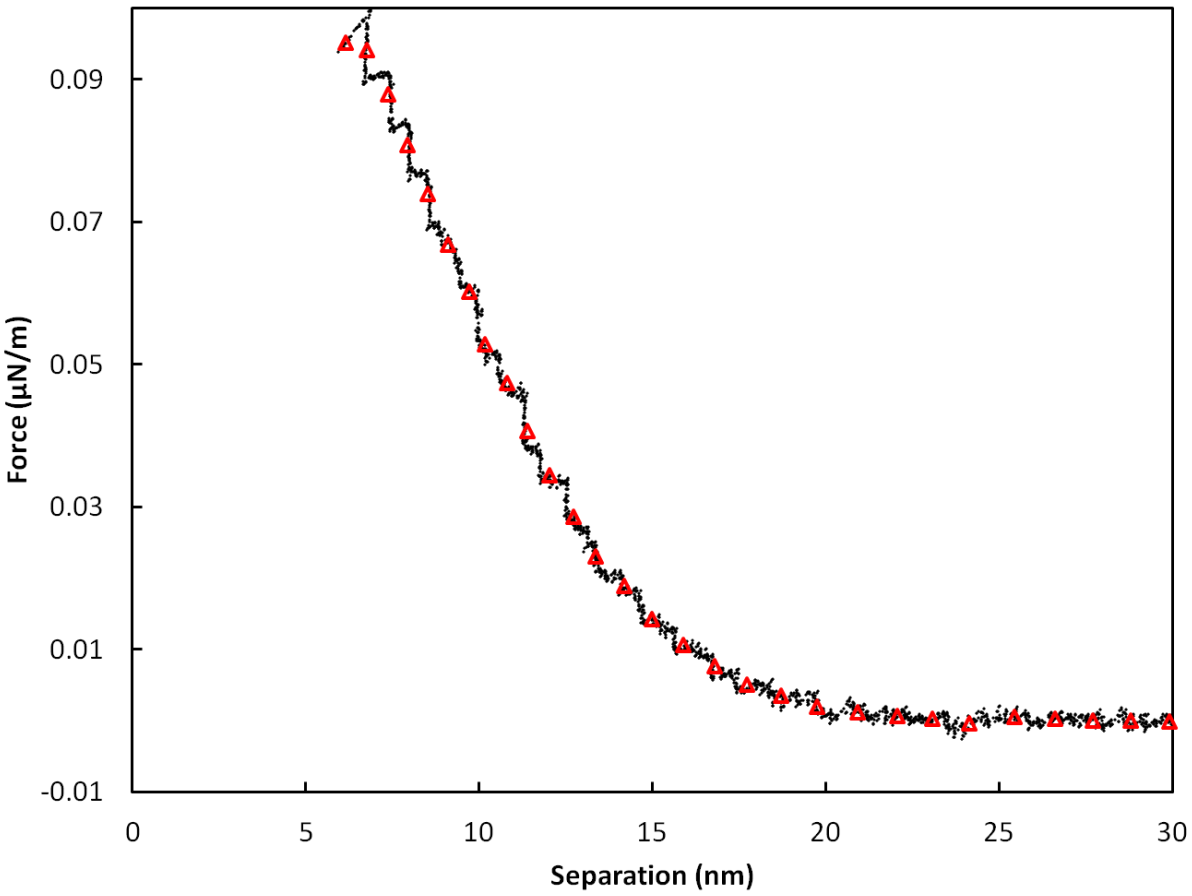

Figure 20: Force vs separation curves for OTS-coated borosilicate glass surfaces immersed in aqueous 15 mM KCl solution. Force is normalized by 2πR, which for a sphere-plate geometry is the interaction energy per unit area for flat-parallel plates (the Derjaguin approximation)[104, 105]. The original force data (black dots) was truncated up to the mechanical instability so that data from the instability were not included in the average. The averaged data (red triangles) is an 80-point running average.

Force Between Hydrophobic Surfaces in Aqueous Solutions has the Form of a DLVO Force at Separations > 5-10 nm

The forces at various salt concentrations, 0.015 M, 0.15 M, and 1 M KCl are shown in Figure 22, Figure 23 and Figure 24. Figures 20 also shows the theoretically calculated DLVO force using a literature value of the potential, 60 mV,[101] and the theoretical Debye-length, 2.5 nm, for this concentration. The reported zeta potentials were obtained by electrophoresis of hexadecane droplets in water.[101] At separations greater than about 5–10 nm, there is good agreement between DLVO and the measured forces for both 15 mM and 1 M KCl solutions. The most striking feature is that there is a strong repulsive double-layer force at low salt, which has been measured previously, and attributed to the adsorption of OH^- ions.[106] Note that our results are consistent with a surface charge, but we cannot determine the sign or necessarily attribute it to the adsorption of OH^- ions. The force in 15 mM varies from experiment to experiment (Figure 22) which is likely due to small variations in the potential for different sample preparations.

The force in 150 mM has the form of a double-layer force, but appears to be offset by approximately 3 nm of separation. The decay length of the force matches the expected Debye length of ~0.78 nm. Figure 25 shows that the mechanical instability does not vary with increasing salt concentration.

Figure 22 and Figure 23 show some variation between experiments; however, this is likely due to minor differences in concentration, differences in sphere topography, or differences in monolayer. The important point is that the measured forces presented here are still much smaller than the strong, long ranged interactions measured in other systems.

The Position Of The Instability Is Independent Of Salt Concentration

Comparison of the forces at 0.015 M, 0.15 M, and 1 M shows that the position of the mechanical instability is always at a separation of 5–10 nm. We can predict the separation at which the instability *would occur if the force were exclusively due to DLVO force:* it is where the gradient of an attractive surface force exceeding the magnitude of the cantilever spring constant, k. The gradient of the surface force at discrete separations is determined by differentiating the functional form of the van der Waals force (34) and the double-layer force (35) with respect to separation:

$$\frac{dF_{sp}}{dD} = \frac{AR}{3D^3} \tag{34}$$

$$\frac{dF_{sp}}{dD} = -4\pi R\varepsilon\varepsilon_o\kappa^2{\psi_o}^2 e^{-\kappa D} \tag{35}$$

The gradient of DLVO forces was taken to be the sum of equation (34) and equation (35). Using the fitted values of the potential at large separation, we find that instability should occur at approximately 2.5 nm for 1 M and less than 1 nm for 15 mM and 150 mM. So, the measured values of the points of instability do not agree with the DLVO values and even the qualitative trends are incorrect. This suggests that DLVO forces alone are not enough to explain the measured forces: it is highly likely that there is another force.

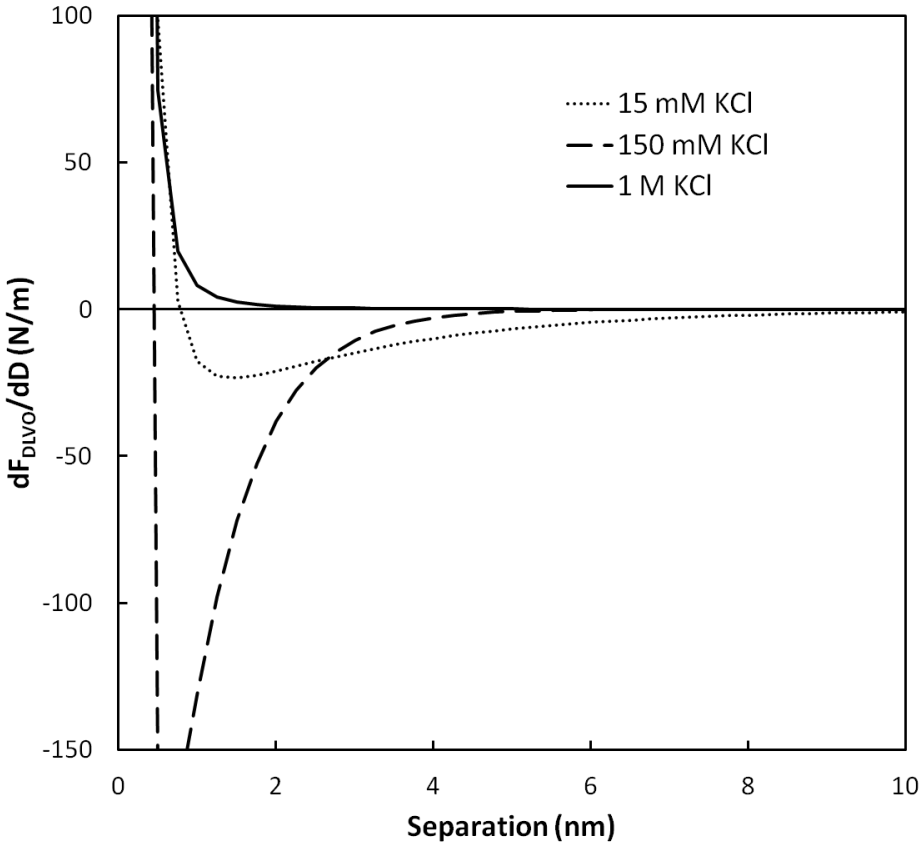

Figure 21: Gradient of the DLVO force with respect to separation for 15 mM, 150 mM and 1 M KCl. The theoretical electrostatic double layer force is calculated from Debye-Hückel theory using a surface potential of 60 mV and a Debye length of 2.5, 0.8, and 0.3 nm for 15 mM, 150 mM and 1 M KCl, respectively. Lifshitz theory was used to predict the van der Waals force between OTS-coated glass surfaces separated by aqueous salt solution.

What is this other force? The other force causes a "sudden" instability in the cantilever, at a separation that is independent of the salt concentration. The most likely explanation is cavitation of a bubble in the thin film separating the hydrophobic surfaces, as has been predicted to occur at the range of 5–10 nm[48].

An alternate explanation is that there is a hydrophobic force that has a range of about 5–10 nm. Such a force could not be independent of salt concentration, because it would need to have a large enough gradient to overcome the double-layer force at ~7 nm in 15 mM salt and at ~ 7 nm in 150 mM salt, yet not have this gradient in the 1 M experiment. Figure 21 shows the gradient of the DLVO force as a function of separation for 15 mM, 150 mM and 1 M KCl. Notice that the gradient of the DLVO force for 150 mM and 1 M KCl is close to zero at approximately 6 nm (the separation of the jump-in for the experimental data). However, the gradient for 15 mM is slightly negative. In the 15 mM KCl we would expect this opposing gradient to decrease the separation that the mechanical instability occurs. Thus, a putative "hydrophobic force" would need to decrease greatly with increasing salt concentration, something that is unlikely.

Note that in the introduction, we stated that the potential could decrease with separation, so there is a danger in interpolating curves fitted at large distance to smaller distances. In the introduction, the discussion was about surfactants, which self associate, because the hydrophobic effects are stronger than electrostatic effects. Here there are no surfactants, just simple monovalent ions. We are unaware of any case where a simple monovalent ion causes the potential to decrease with separation.

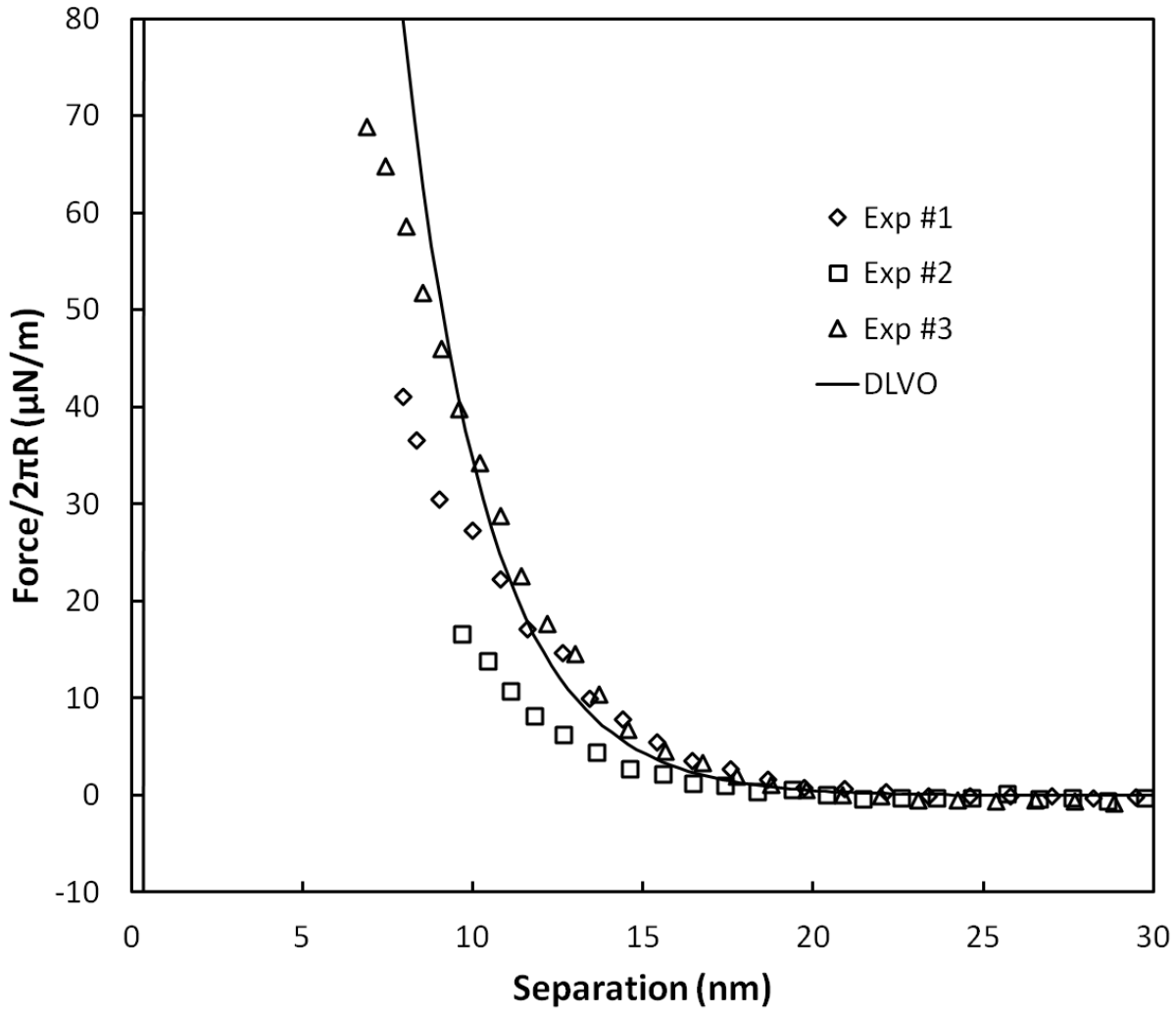

Figure 22: Force vs separation curves for OTS-coated borosilicate glass surfaces in 15 mM KCl at 23° C. Triangles, diamonds, and squares represent different experiments. Each curve is an average of a single, typical curve from the data set. A mechanical instability occurs at 7–10 nm in all experiments. The solid line is the sum of the electrostatic double layer and the van der Waals prediction for the system. The theoretical electrostatic double layer force is calculated from Debye-Hückel theory using a surface potential of 60 mV and a Debye length of 2.5 nm. Lifshitz theory was used to predict the van der Waals force between OTS-coated glass surfaces separated by aqueous salt solution.

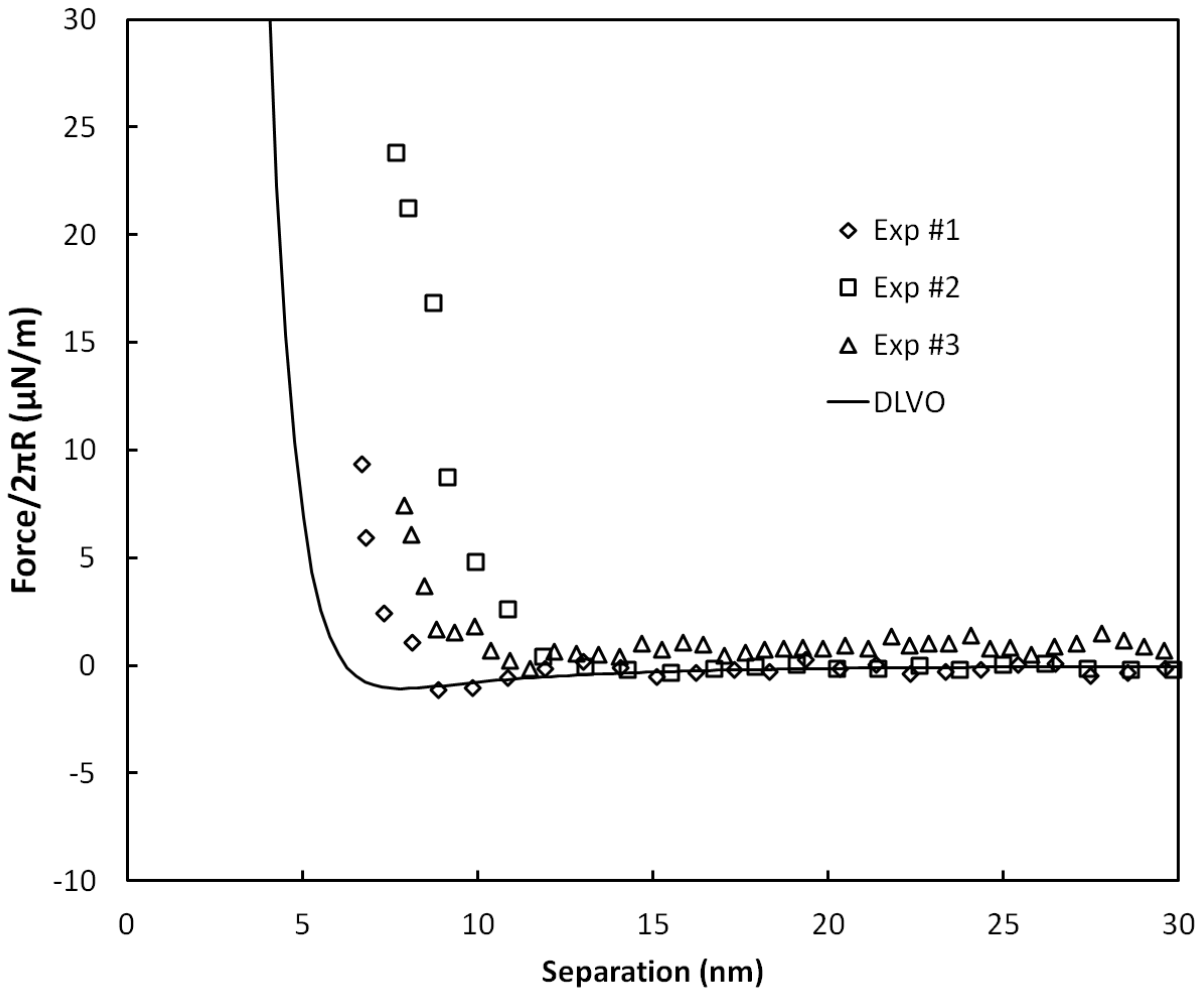

Figure 23: Force vs separation curves for OTS-coated borosilicate glass surfaces in 150 mM KCl at 23° C. Triangles, diamonds, and squares represent different experiments. Each curve is an average of a single, typical curve from the data set. A mechanical instability occurs at 7–10 nm over all experiments. The solid line is the sum of the electrostatic double layer and the van der Waals prediction for the system. The theoretical electrostatic double layer force is calculated from Debye-Hückel theory using a surface potential of 60 mV and a Debye length of 0.8 nm. Lifshitz theory was used to predict the van der Waals force between OTS-coated glass surfaces separated by aqueous salt solution.

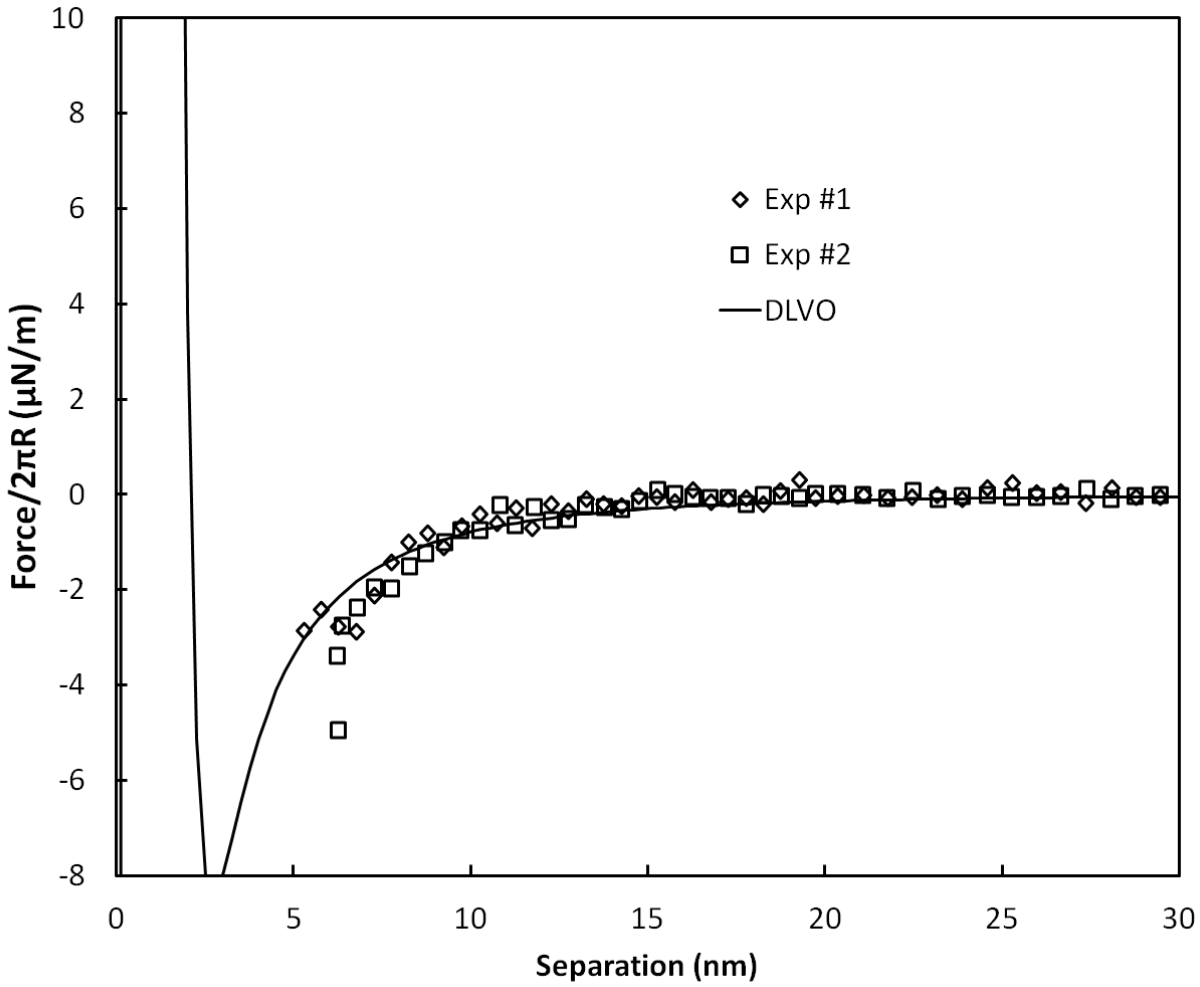

Figure 24: Force vs separation curves for OTS-coated borosilicate glass surfaces in 1 M KCl at 23° C. Diamonds and squares represent different experiments. Each curve is an average of a single, typical curve from the data set. A mechanical instability occurs at 5–10 nm over all experiments. The solid line is the sum of the electrostatic double layer and the van der Waals prediction for the system. The theoretical electrostatic double layer force is calculated from Debye-Hückel theory using a surface potential of 60 mV and a Debye length of 0.3 nm. Lifshitz theory was used to predict the van der Waals force between OTS-coated glass surfaces separated by aqueous salt solution.

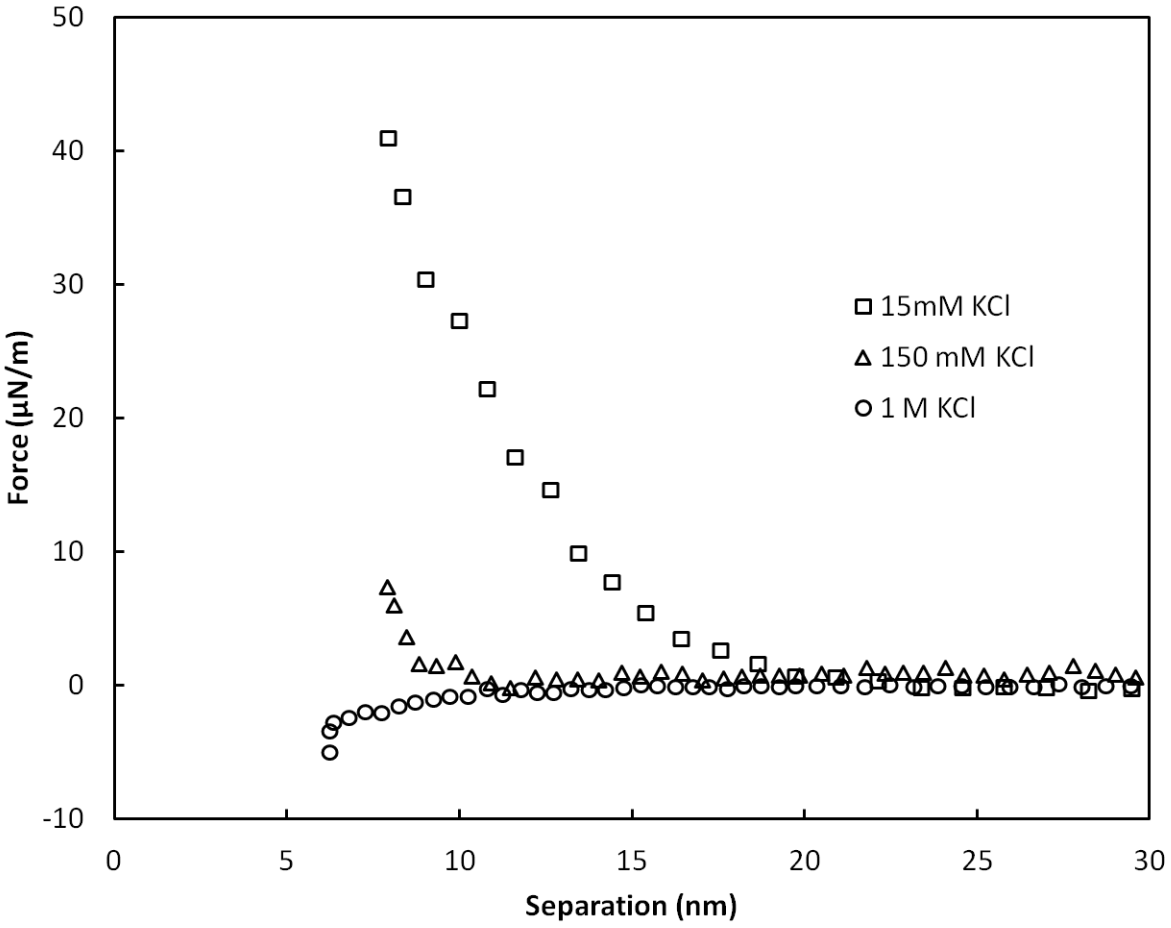

Figure 25: Force vs separation curves for OTS-coated borosilicate glass surfaces in 15 mM, 150 mM and 1 M KCl at 23° C. Squares, triangles, and circles represent KCl concentrations of 15 mM, 150 mM, and 1 M, respectively. Each curve is an average of a single, typical curve from the data set. A mechanical instability occurs at 5–10 nm over all experiments.

Force Between Hydrophobic Surfaces in Aqueous Solutions at Low pH

Although Figure 24 shows excellent agreement between Lifshitz predictions and the total measured force, arguments have been made that high salt concentrations may affect the hydrogen bonding network of water[107]. It is possible that the strength of the hydrophobic

force wanes with increasing salt concentration due to the disruption of the water structure, so studying the effect of salt concentration may reveal any correlation between these two phenomena. The measurements in low concentrations of KCl showed no evidence of a long-range hydrophobic force, but were complicated by the existence of a large double-layer force. In this section, I describe measurements in an acidic solution. By experiment, I find that a lower concentration of H^+ (HCl) is required compared to K^+ ions to remove the double-layer force (i.e. the proton is a potential determining ion), so it allows me to search for the hydrophobic force at both low salt and low double layer.

By experiment, I found that there was still a residual double-layer force at pH 3 solution, but there is negligible double-layer force at pH 2. Thus the experiments were done pH 2 and with two salt concentrations, 1 and 10 mM KCl. About 10 mM HCl was required to reach pH 2, so the experiments were done in a total salt concentration of 11 mM and 20 mM salt, with a theoretical Debye length of 2.89 nm and 2.14 nm respectively.

Figure 26 shows the total force vs separation curve for pH 2 solutions at 1 and 10 mM KCl. The theoretical curves are for 5 mV and 10 mV, clearly the measured force is for a surface with a very low potential, allowing resolution of a putative hydrophobic force. However, there is little or no force at separations greater than 10 nm, again consistent with the idea that there is no long-range hydrophobic force. As for the pH 6 solutions, the jump-in occurred between 5–10 nm. This is again consistent with the idea of nucleation of a vapor cavity. It is difficult to envisage a hydrophobic force which exactly varies with salt or pH in each case such that the instability always occurs in the range 5–10 nm. This again supports

the idea that there is no hydrophobic force and merely nucleation of a bubble at a critical separation due the hydrophobicity.

As an aside note that the small difference in force between the measurements in high salt and low pH are probably not significant. As can be seen from the theoretical curve in Figure 24, only a very residual potential is required to produce a double-layer force that has a similar magnitude to the van der Waals force and it is likely that the measurement is not exactly at the point of zero charge (PZC). This reinforces an important point: that we have now shown that even if a very weak hydrophobic force should exist, it is so weak that it would be dominated by double-layer forces except exactly at the PZC or at very high salt concentrations.

The Force Between Pristine Hydrophobic Surfaces in Aqueous Solutions is Not Unique

In the previous section, we described how water vapor could form when two hydrophobic solids are very close. We would expect that this water vapor cavity would dissolve when the surfaces are separated. It has been suggested that nanobubbles may form when a hydrophobic surface in probed, such as a hydrophobic colloidal particle probing a hydrophobic surface[108]. If the bubbles are stable, then subsequent approaches will be different because of the presence of the bubble on the solid, and this would manifest as a different force curve on the first compared to subsequent measurements. More specifically, we would likely see an increase in the strength of the attractive force, an increase in the separation that the mechanical instability occurs at due to bridging

nanobubbles, and the onset of step-like jump-ins on the approach curves of the subsequent forces.

Figure 27 shows the first, second, third, sixth and tenth consecutive forces of a single experiment. Although the measured force does vary from curve to curve, the curves are qualitatively similar. Most importantly, the initial force curve is almost quantitatively identical to the sixth force curve demonstrating that prior contact between the surfaces had no effect on the resulting force curve. However, it is possible that a nanobubble formed at the interface by some other mechanism before any contact was made between the two surfaces, but we do not see step-like instabilities which are often indicative of coalescing nanobubbles at the interface.

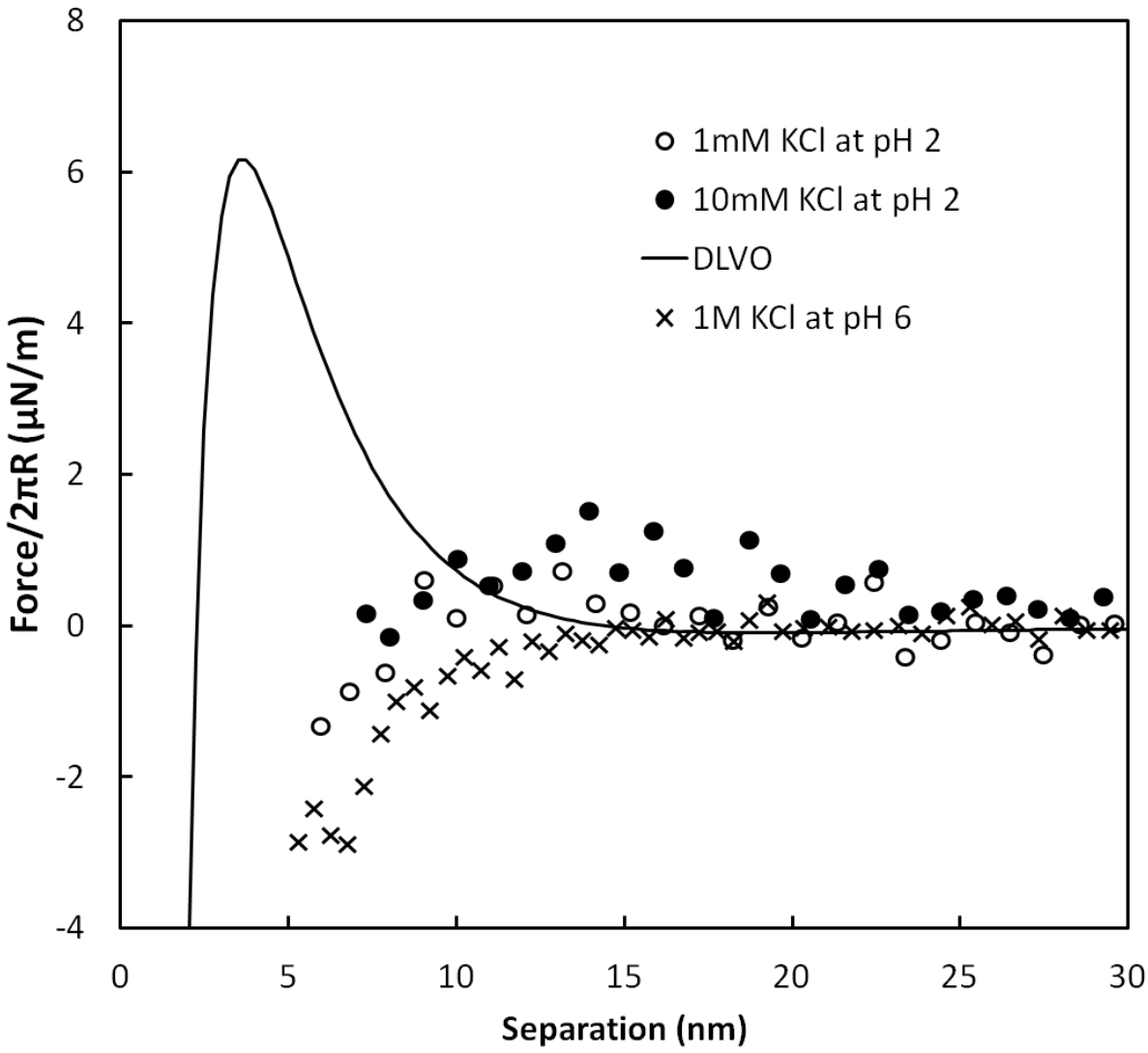

Figure 26: Force vs separation curves for OTS-coated borosilicate glass surfaces in 1 mM and 10 mM KCl solutions at pH 2 and 23° C. Open and closed circles represent KCl concentrations of 1 mM and 10 mM, respectively. Each curve is an average of a single, typical curve from the data set. A mechanical instability occurs at 5–10 nm for both concentrations. The dashed line is a Lifshitz theory prediction of the van der Waals force between OTS-coated glass surfaces separated by aqueous salt solution. The '×' symbols are the 1 M KCl data found in Figure 17.

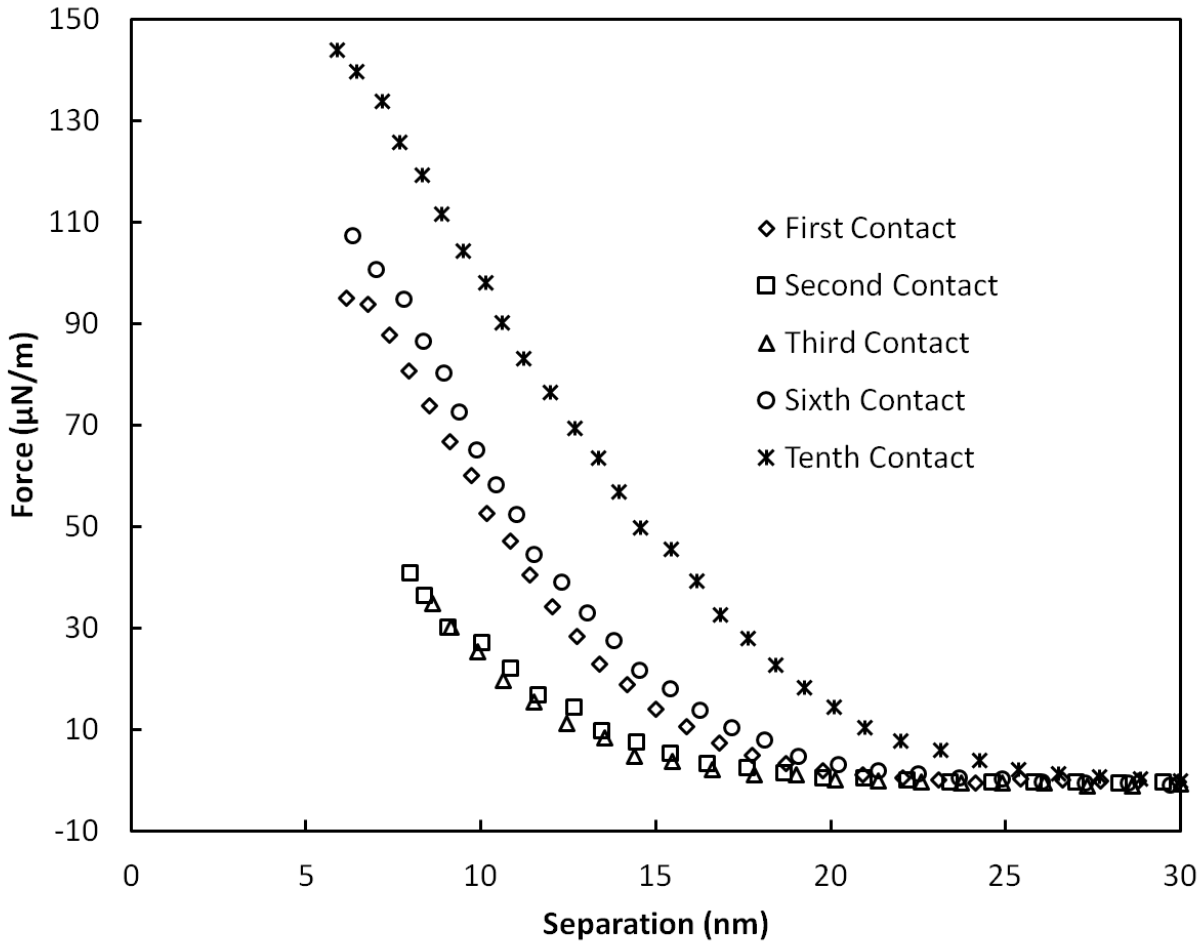

Figure 27: Force vs separation curves for OTS-coated borosilicate glass surfaces in 15 mM KCl at 23° C. Different symbols represent different approaches in the same experiment. An 80-point moving average is taken of each curve to reduce the number of points. The "First Contact" curve was measured without any prior contact between the sphere and the plate.

Conclusions of Salt Concentration Effects

In conclusion, we found that the force between hydrophobic solids in aqueous salt solutions agrees with DLVO predictions up until approximately 5 nm of separation. Furthermore, the gradient of the total force exceeded the magnitude of the cantilever

spring constant at 5–10 nm, both in the presence and absence of the repulsive double layer, which does not agree with predictions for a purely DLVO interaction. This implies that the gradient of the force is much larger in magnitude than the double layer. Such a strong, spontaneous attraction could be the result of a cavitation force and has been predicted to occur at the range of 5–10 nm[48]. Similar behavior was observed near the isoelectric point, where both electrolyte concentration and electrostatic repulsion are low. The agreement between measurements near the isoelectric point and at high (1 M) salt concentration supports the conclusion that the force between hydrophobic surfaces is unaffected by salt concentration[109]. The double-layer force varies greatly among all the conditions measured here, yet the mechanical instability remains at the same location. It is difficult to imagine a force law that would accommodate all these changes, and it seems easy to explain the results in terms of spontaneous cavitation.

We also show that the force between pristine (no prior contact) surfaces is qualitatively the same, in terms of the separation of the mechanical instability and decay length, after subsequent contacts. Assuming that no nanobubbles formed prior to solid–solid contact, we could conclude that the separation of two hydrophobic surfaces submerged in water did not initiate the formation of nanobubbles.

As mentioned earlier, high concentrations of salt is believed to disrupt the hydrogen bonding network of water[107]. However, if the measured force was related to the disruption of the hydrogen bonding network we would expect the strong, short-ranged attraction to change with salt concentration. Previous work also shows that this interaction is

independent of temperature, which further supports that it is unrelated to the entropy driven hydrophobic effect.

There still remains the unanswered question: is there a "hydrophobic force", or a force induced by hydrophobicity? The lack of dependence on temperature and salt concentration would suggest that the hydrophobicity of the surface does not directly create a force between the two surfaces for separations greater than about 6 nm. However, these findings have not ruled out bubble coalescence or cavitation, both of which are a consequence of the high interfacial energy of the solid-liquid interface, as a possible cause of the strong, short-ranged attraction. The reproducible nature of the mechanical instability would agree with the behavior of water confined between two hydrophobic surfaces[43, 48] while the limited understanding of nanobubble formation and stability makes it difficult to fully rule out nanobubbles even in degassed solutions[108].

Significance of this Work

The results presented in this section make it very difficult to propose the existence of "hydrophobic force" for separations greater than about 6 nm in the sense of a force due to water structure or destructuring. This is even for quite hydrophobic solids (contact angle ~110°). The force would need to have a complex response to salt and pH. In addition, should such a force exist, it is almost irrelevant because it is so weak that it is obscured by double layer forces and even by van der Waals forces in a situation where van der Waals forces are very weak. Thus, there is no need to invoke a long-range hydrophobic force. The effects of hydrophobicity are better interpreted in terms of spontaneous cavitation.

VII. Nanobubble Stability

Introduction

It was mentioned in Chapter II that previous work on the hydrophobic force showed long-range attractions that were later found to be coalescing nanobubbles. Though my force measurements presented in Chapters V and VI were performed in degassed solutions, I found that many of my experiments still presented obvious characteristics of coalescing bubbles (step-like force and very long-range attractions). This of course begs the question: why do bubbles still form in the absence of dissolved gas?

It is widely known that nanoscale vapor phases, known as nanobubbles, readily form at the interface between hydrophobic solids and aqueous liquids[108]. It is accepted that much of the literature that claim a very long-range "hydrophobic" force exists is in fact due to coalescing interfacial nanobubbles[55, 56]. However, thermodynamics shows that bubbles at this scale should be highly unstable due to a large Laplace pressure[108, 110]. On the contrary, nanobubbles have been shown to be stable for days due to their radii of curvature being on the micro-scale despite their name[110]. Several groups have studied the effects of electrolyte concentration[62, 63, 111], dissolved gas, temperature[112], and roughness[72, 113, 114] on the stability and behavior of interfacial bubbles. Furthermore it is not fully understood how they form or if they exist in bulk.

The Laplace pressure of a nanoscale bubble in bulk is approximately 15 atm. This high pressure should drive a large flux of gas out the small volume in only microseconds[108]. The boundary condition for the dissolution of bubbles is important. If the three phase line is

pinned, then the radius of curvature will increase as the bubble dissolves, leading to a slowing of bubble dissolution[115]. The main goal of this work is to investigate the effect of the bulk liquid phase on the formation of bubbles at the solid-liquid interface using atomic force microscopy, and the secondary goal is understand whether the surfaces are pinned. The effect of solution exchange, dissolved gas concentration and changes in properties of the initial solution is studied.

In addition to studying interfacial nanobubbles we collaborated with Revalesio to investigate the existence of bulk nanobubbles. Revalesio has found a process for oxygenating saline solutions that provides therapeutic benefits for certain inflammatory diseases. They hypothesize that these benefits arise from bulk phase nanobubbles. Our goal is to compare interfacial nanobubble formation between Revalesio's therapeutic solution, RNS60, and a control solution, ONS60, and relate this to nanobubble formation from the bulk.

Literature Review

The phenomenon of bridging vapor cavities or coalescence of nanobubbles was first proposed as an explanation for very long range attractive forces between hydrophobic surfaces[17]. Ishida et al. used tapping mode atomic force microscopy imaging to acquire the first evidence of interfacial nanobubbles on OTS-coated silicon wafer[116]. Since then numerous groups have investigated nanobubbles at the solid-liquid interface of hydrophobic surfaces[69, 71, 72, 112, 117-120]. This literature review will briefly cover the theoretical and experimental findings on interfacial nanobubbles, including the various techniques for nanobubble formation and proposed theories for nanobubble formation and stability.

Nanobubble Stability

There are several theories for the unexpected stability of nanobubbles; however, many of these are debunked by the large Laplace pressure that would be expected for a nanoscale bubble. The dynamic equilibrium model proposed by Brenner and Lohse[121] suggests that stability may be achieved through the diffusion of gas at the three phase line. Although the dynamic equilibrium model is able to account for many of the phenomena seen in various studies it requires an energy source. It is not clear how a mechanism that requires an energy source can be described as a mechanism of stability. Furthermore, this model is unable to explain why nanobubbles are able to form on mica.

Ducker et al. suggest that nanobubble stability could arise from contamination that may arise from the solvent transfer process[72, 110]. While this would certainly explain the long

lifetimes of nanobubbles, it is unable to explain the origin of contamination in system when no solvent exchange takes place, for example nanobubbles can form spontaneously from pure water on a hydrophobic surface.

Nanobubble Formation

Nanobubbles have been found to be formed by various means depending on the properties of the substrate, such as roughness and contact angle, as well as the properties of the liquid and temperature of the system. Here I will briefly cover the most common means of forming nanobubbles: spontaneously on high contact angle surfaces, from solvent exchange, gas captured in surface roughness and surface perturbation.

Spontaneous formation of nanobubbles is most common on surfaces with a high water contact angle (>90°). These types of bubbles are most often the cause of many long ranged "hydrophobic" forces reported on silanized glass surfaces.

Several groups have shown bubble formation after solvent exchange between two liquid with differing gas solubilities[69, 72, 112, 122-125]. For example, replacing ethanol with water creates a gas super saturated environment near the hydrophobic surface which encourages bubble formation. Although some groups have found that a degree of hydrophobicity is not required to produce nanobubbles by this technique[122, 124, 126], lower contact angles do produce noticeably smaller and fewer nanobubbles than a higher contact angle surface.

Another mechanism for bubble formation is surface roughness. Small cracks on hydrophobic surfaces can prevent water from entering and trap gas[108, 112]. This gas can nucleate and form surface nanobubbles. This mechanism for nanobubble formation is very

useful, and important, when considering hydrophobic force measurements done by AFM. However, much of the nanobubble imaging that has been studied is generally done on HOPG, mica or other very smooth surfaces to avoid this type of bubble formation.

In an earlier section it was mentioned that the separation of two hydrophobic surfaces could result in the formation of a vapor capillary, which could in turn leave behind a nanobubble at either of the two solid-liquid interfaces. However, some research has speculated that simply probing a surface with an AFM tip (as with contact mode imaging) can disturb the interface enough to produce interfacial nanobubbles[108, 127-129].

Materials and Methods

Surface Imaging

Atomic force microscopy imaging was performed on a Cypher AFM (Asylum Research, Santa Barbara, CA) using ORC8 cantilevers (Bruker) with a nominal spring constant of 0.71 N/m. Cantilevers were treated with ozone for approximately one hour prior to imaging. Substrates were loaded into the AFM and a capillary was formed by carefully placing 100 – 150 μL of solution on the substrate. Normal saline (NS), saline pressured with oxygen (ONS60), and saline pressurized by means of Taylor-Couette-Poiseuille (RNS60) flow were provided by Revalesio, who were our collaborators on this project. ONS60 and RNS60 were both pressurized with O_2 to a concentration of 60±5 ppm at 5° C. Solution exchange was done by gently adding and removing ~30 μL (approximately 20–35% of the capillary volume) of solution 2 – 3 times. Surfaces were imaged 30 – 60 mins before and after exchanges to ensure the concentration was homogeneous. Tapping mode imaging was used to image the interfacial nanobubbles and contact mode imaging was used to verify that features present in the tapping mode image were not part of the substrate topography. For some experiments very low set point contact mode imaging was used to image interfacial nanobubbles.

Substrate Preparation

Various substrates were chemically modified and characterized: Bare-mica (Ruby Mica, India), amine-terminated silane on silicon, highly ordered pyrolytic graphite (HOPG, MikroMasch), alkyl-terminated silane on silicon, alkyl-terminated gold-thiols on silicon,

and alkyl-terminated silane on glass. All silicon and glass substrates were exposed to O_2 plasma for 2 minutes at 100 Watts using a Plasma Prep III Solid State (SPI) to remove contaminants and prepare surfaces reactive to silane. Silicon wafers were obtained from Wafer World (West Palm Beach, FL). Glass samples were either smooth coverslips (Fisher Finest, Fisher Scientific) or standard glass slides (VWR).

Bare Mica and HOPG

Bare mica and HOPG were freshly cleaved and mounted to a metal sample disk. Care was taken to ensure that the surfaces were smooth and uniform.

Amine-terminated Silicon

Activated silicon samples were placed overnight in a 5 mM solution of 3-aminopropyltriethoxysilane (APTES, Sigma-Aldrich) in dry toluene (Spectrum). Samples were sonicated in fresh toluene for 15 minutes, rinsed thoroughly with absolute ethanol and Millipore water, and blown dry with ultra-high purity nitrogen (Airgas).

Alkyl-terminated Glass and Silicon

Activated silicon or glass samples were placed overnight in a 5 mM solution of octadecyltrichlorosilane (OTS, Sigma-Aldrich) in hexadecane (Alfa-Aesar). Samples were sonicated in fresh chloroform *twice* for 15 minutes each, rinsed thoroughly with absolute ethanol and Millipore water, and blown dry with ultra-high purity nitrogen.

Gold-Thiol

Gold-coated silicon substrates were treated with ozone for 10 minutes and then placed in a 5:1:1 mixture of Millipore water, ammonia and hydrogen peroxide at 75 °C for 5 minutes. Samples were thoroughly rinsed with Millipore water and dried under a stream of ultra-high purity nitrogen.

Cleaned samples were placed overnight in a 5 mM solution of undecanethiol (Sigma-Aldrich), or hexadecanethiol (Alfa-Aesar), in absolute ethanol. Samples were rinsed with absolute ethanol, Millipore water, and blown dry with ultra-high purity nitrogen.

Solution Preparation

All saline solutions were allowed to reach room temperature in order to reduce imaging effects due to temperature fluctuations and time-dependent changes in dissolved oxygen (DO) concentration due to the decrease in solubility with increasing temperature. For some studies the solutions were degassed by freeze-pump-thawing or by the addition of sodium sulfite (Sigma-Aldrich), an oxygen scavenging agent.

Dissolved Oxygen (DO) Measurements

Dissolved oxygen concentrations were obtained using a fluorescence-based oxygen sensor (Ocean Optics). Measurements were taken at constant temperature for chilled (~5 °C) and room temperature (~23 °C) vials. Measurements were taken at 5 minute intervals to ensure steady readings.

Results and Discussion

Selecting a Surface for Use as a Metric for Distinguishing ONS60 and RNS60

Our criteria for a proper surface for distinguishing the two solutions ONS60 and RNS60 was that it readily forms nanobubbles. Surfaces varied in terms of advancing contact angle, functionalized vs native hydrophobicity, and surface roughness. Atomic force microscopy images were taken of each surface in the presence of NS, ONS60 and RNS60. Surfaces with advancing contact angles of less than 90° (bare mica, APTES on silicon and HOPG) were found to produce smaller and fewer interfacial bubbles than those with advancing contact angles above 90° (OTS on silicon and C11/C16 gold thiol).

Atomic force microscopy tapping mode images of bare mica submerged in oxygen-saturated saline solution RNS60 show no signs of nanobubbles (Figure 28). This is explicable because mica is hydrophilic (contact angle <10°). The size and quantity of nanobubbles increased with increasing contact angle. Images of APTES (Figure 29), HOPG (Figure 30), alkanethiol (Figure 31), and OTS (Figure 32) support this trend. Alkanethiol and OTS-coated silicon were selected to discriminate between RNS60 and ONS60 because they were the only two surfaces to readily form enough nanobubbles to draw a comparison with.

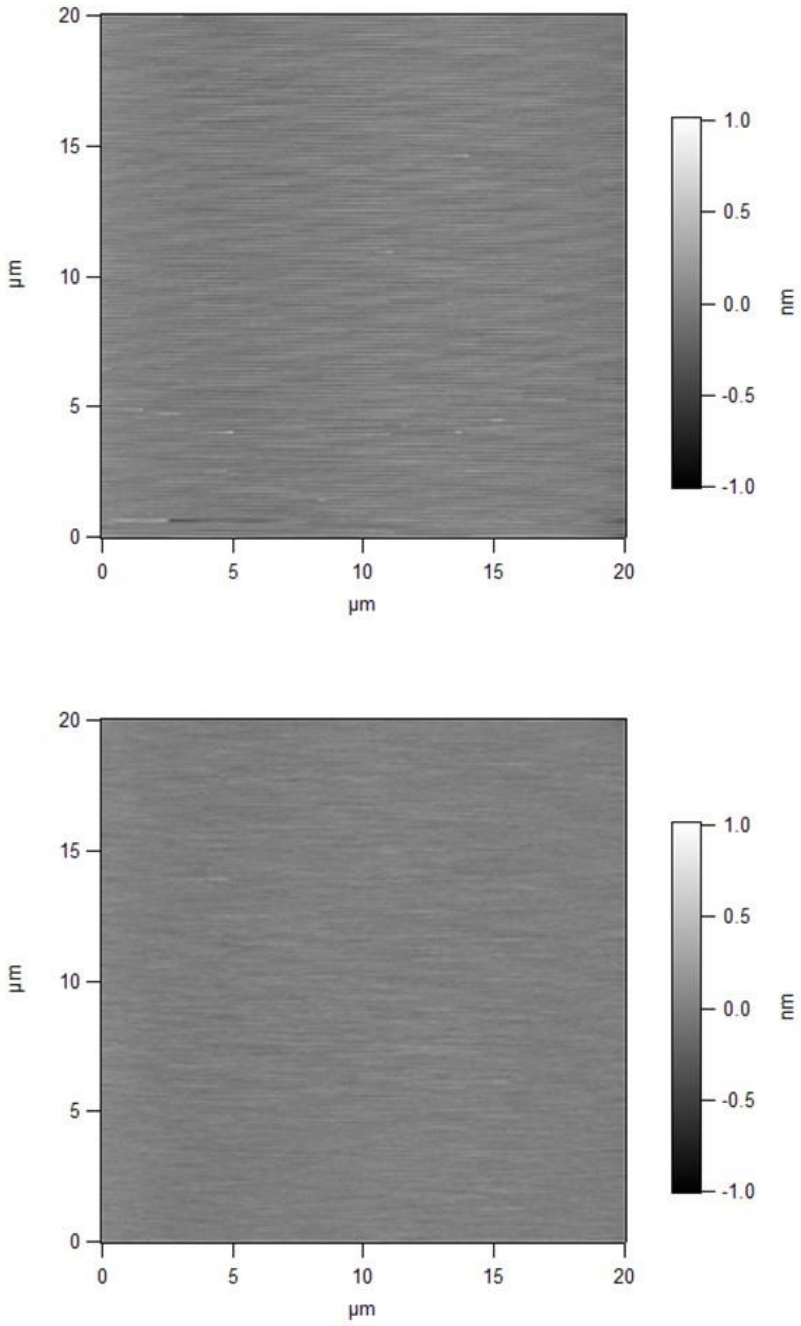

Figure 28: AFM tapping (top) and contact (bottom) mode images of a 20×20 µm² region of bare mica (θ_A<10°) submerged in RNS60. Imaging was performed on a Cypher AFM (Asylum Research) using an ORC8 cantilever (68 kHz, 0.38 N/m, Bruker).

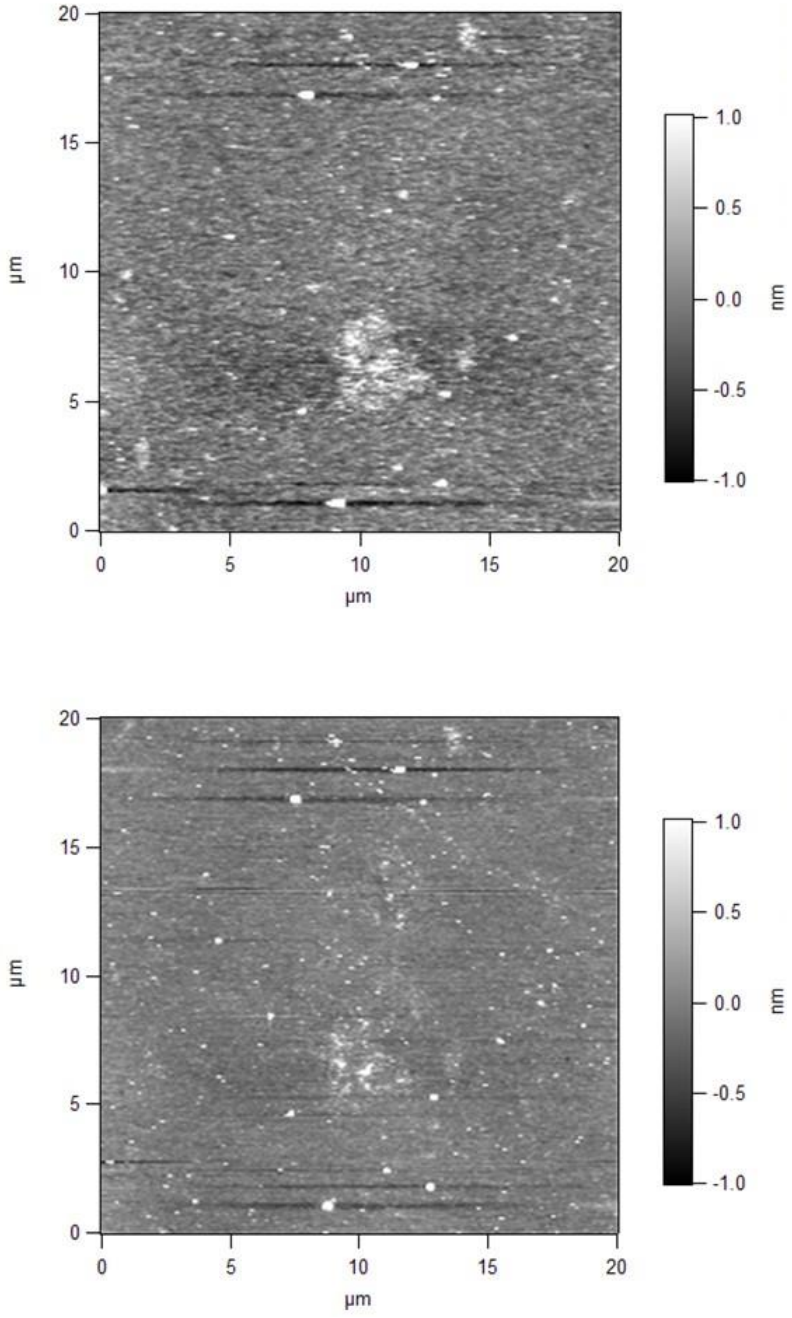

Figure 29: AFM tapping (top) and contact (bottom) mode images of a 20×20 µm^2 region of APTES-coated (θ_A=60°) silicon submerged in RNS60. Imaging was performed on a Cypher AFM (Asylum Research) using an ORC8 cantilever (68 kHz, 0.38 N/m, Bruker).

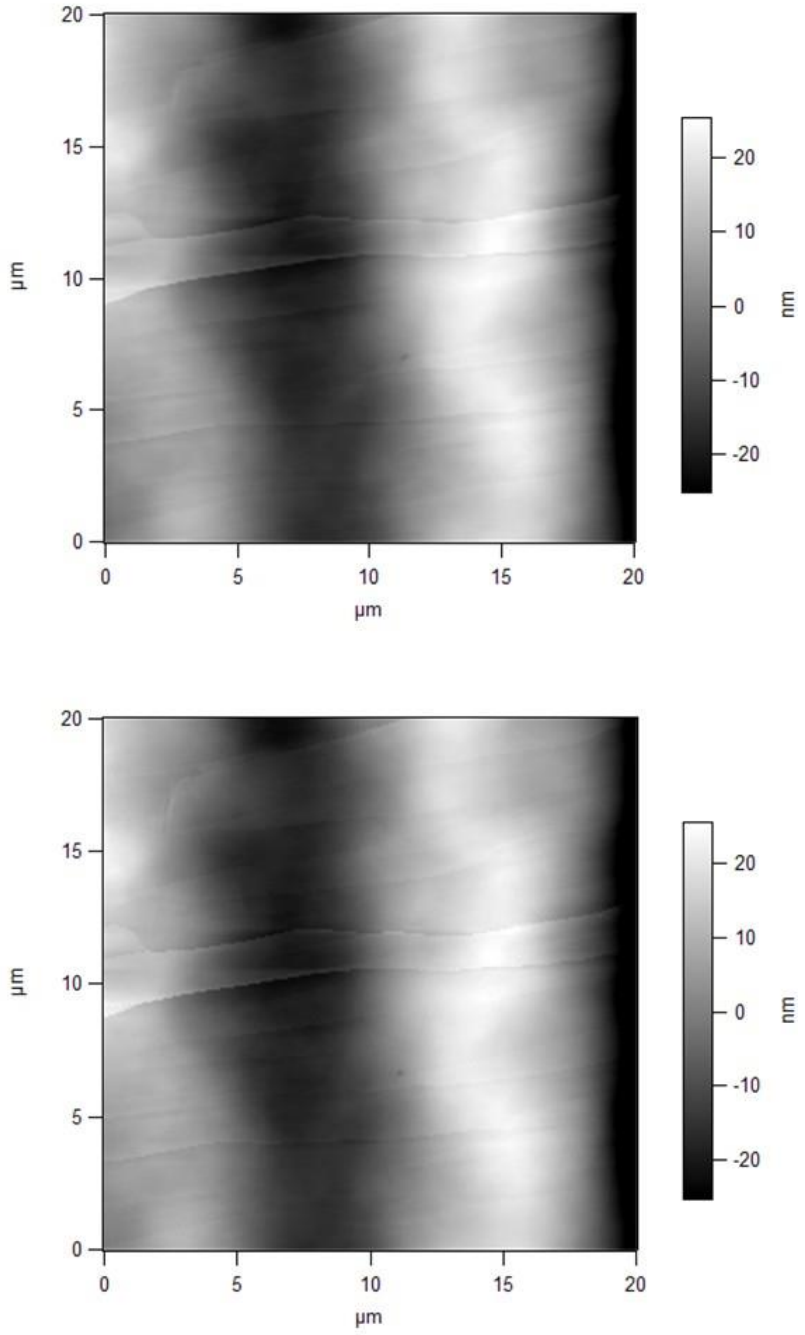

Figure 30: AFM tapping (top) and contact (bottom) mode images of a 20×20 µm² region of HOPG (θ_A=85°) submerged in RNS60. Imaging was performed on a Cypher AFM (Asylum Research) using an ORC8 cantilever (68 kHz, 0.38 N/m, Bruker).

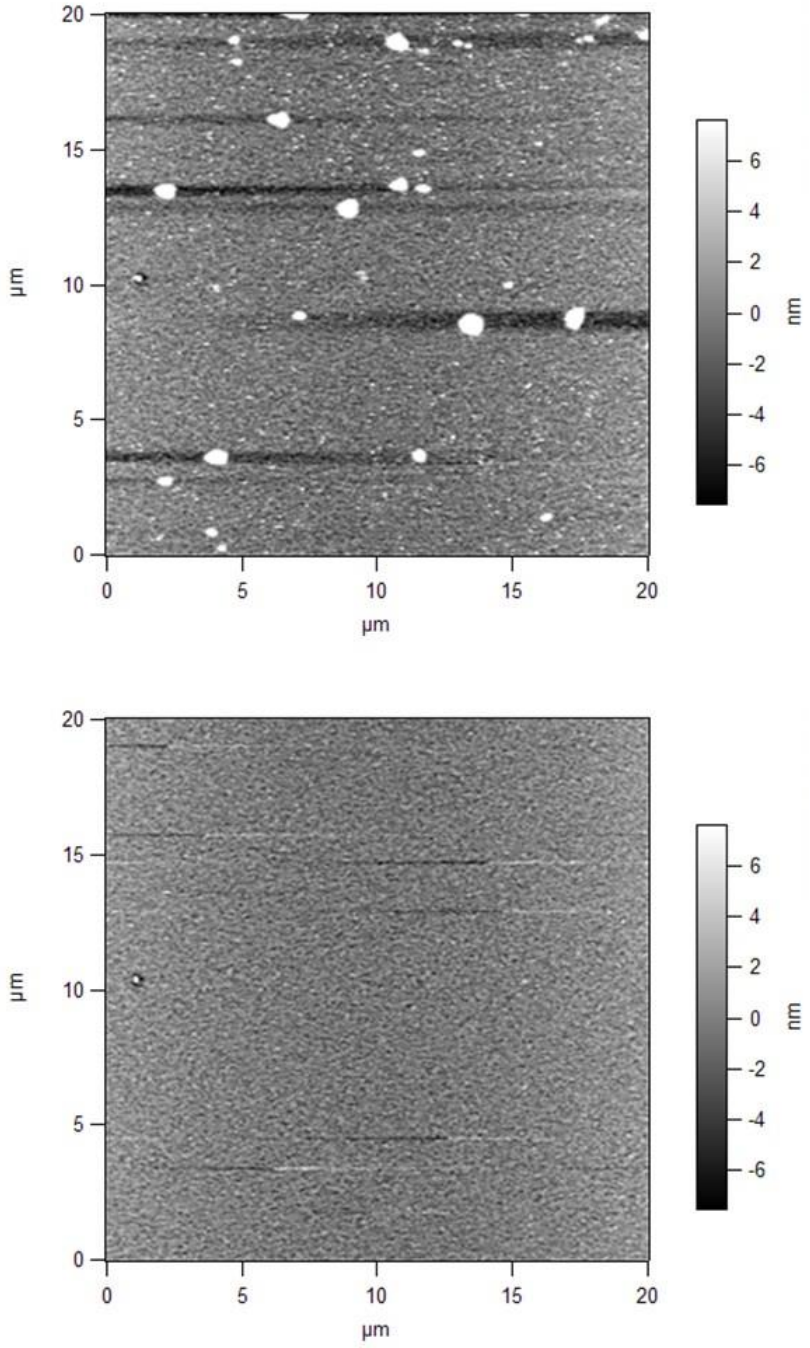

Figure 31: AFM tapping (top) and contact (bottom) mode images of a 20×20 µm² region of undecanethiol on silicon (θ_A=100°) submerged in PNS60. Imaging was performed on a Cypher AFM (Asylum Research) using an ORC8 cantilever (68 kHz, 0.38 N/m, Bruker).

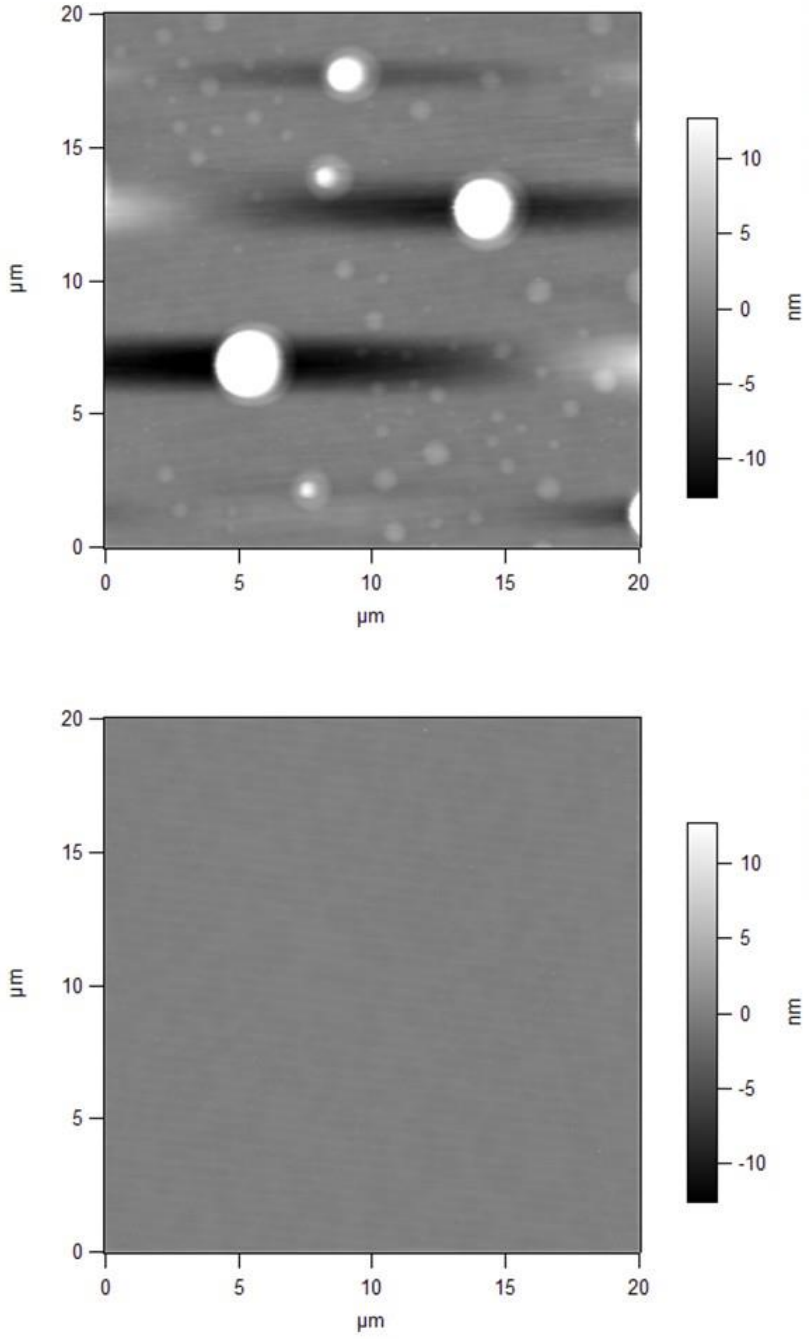

Figure 32: AFM tapping (top) and contact (bottom) mode images of a 20×20 µm² region of OTS-coated silicon (θ_A=110°) submerged in RNS60. Imaging was performed on a Cypher AFM (Asylum Research) using an ORC8 cantilever (68 kHz, 0.38 N/m, Bruker). The black bands in the top image are an artifact from image processing and are not a feature of the surface.

It is important to note that a great deal of variation was seen not only between separate experiments of the same surface-solution combination but also between different regions on the same surface for a given experiment. That being said, the AFM images shown in Figure 28–Figure 32 were selected to be representantive. A comparison of two regions of on a single alkanethiol-coated silicon substrate submerged in ONS60 (Figure 33) shows the level of variation that can occur during the nucleation of the gas bubbles.

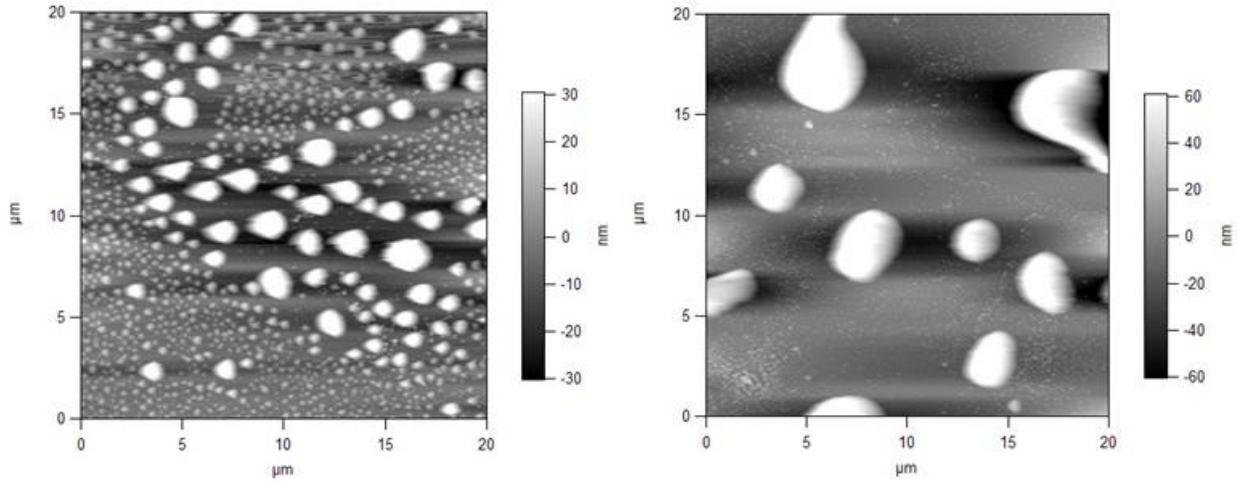

Figure 33: AFM tapping mode images of two different 20×20 µm² regions of a hexadecanethiol on silicon (θ_A=100°) substrate submerged in ONS60. Imaging was performed on a Cypher AFM (Asylum Research) using an ORC8 cantilever (68 kHz, 0.38 N/m, Bruker). The black bands are artifacts from image processing.

While two regions may show very little difference, the variation in size and bubble quantity shown in Figure 33 is not uncommon. It is paramount that any comparison study between ONS60 and RNS60 be done over the same region to ensure any differences are due to the solution and not slight topographical variation in sampling regions.

Effect of Solution Exchange and the Impact of the Initial Solution

It was shown in the previous section that the bubble size and quantity between regions of a given surface could vary quite a bit, thus it would be dubious to compare the bubble formation of ONS60 and RNS60 on two different regions of a surface. By exchanging solutions without changing the position of the cantilever on the substrate we were able to compare ONS60 and RNS60 at a specific region of the surface and ensure that any differences seen were due to differences in the solutions and not differences in the substrate topography. After comparing numerous AFM images we concluded that no difference could be found between ONS60 and RNS60.

Are Nanobubbles Permeable to Gas?

Sodium sulfite, an oxygen scavenger agent, reacts readily with dissolved oxygen to produce sulfate ions as seen in the following reaction:

$$2Na_2SO_3 + O_2 \rightarrow 2Na_2SO_4 \tag{35}$$

By decreasing the concentration of dissolved oxygen in the liquid phase we would expect a large decrease in bubble size due to the diffusion of oxygen from the gas bubble to the liquid phase.

We have shown that changing the gas concentration had no obvious effect on already formed nanobubbles, so the next step was to test the concentration of the initial solution. By adding sodium sulfite to ONS60 we were able to obtain a dissolved oxygen concentration of approximately 0 ppm.

Figure 34 and Figure 35 show two different regions of the same OTS-coated surface submerged in pure RNS60 (initially, left) and after the addition of a concentrated sodium sulfite solution in RNS60 (right). The most obvious difference between Figure 34 and Figure 35 is the density of bubbles present over the same 3x3 μm^2 region. However, the more important feature is that bubble size is unaffected by the addition of sodium sulfite.

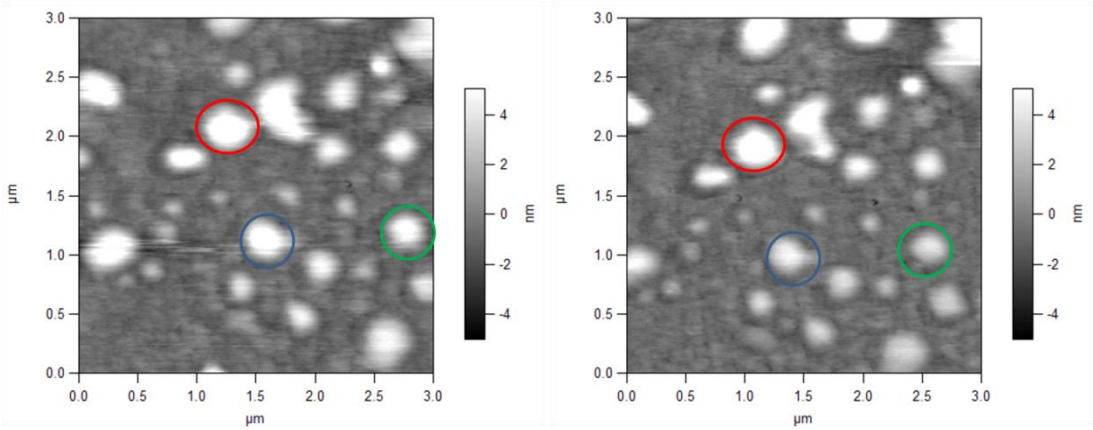

Figure 34: AFM tapping mode images of a 3×3 μm^2 region of OTS-coated silicon submerged in RNS60 before (left) and after (right) the addition of sodium sulfite. Imaging was performed on a Cypher AFM (Asylum Research) using an ORC8 cantilever (68 kHz, 0.38 N/m, Bruker). Circles are used to give a reference scale for changes in size between the two images.

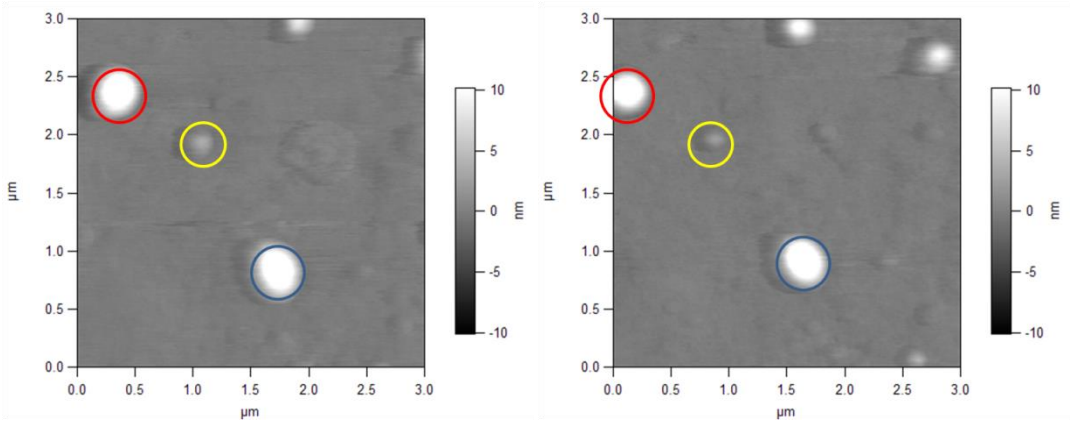

Figure 35: AFM tapping mode images of a 3×3 μm^2 region of OTS-coated silicon submerged in RNS60 before (left) and after (right) the addition of sodium sulfite. Imaging was performed on a Cypher AFM (Asylum Research) using an ORC8 cantilever (68 kHz, 0.38 N/m, Bruker). Circles are used to give a reference scale for changes in size between the two images.

This would imply that these nanobubbles did not contain oxygen, or that gas is unable to diffuse across the gas-liquid interface of the bubble, possibly due to contamination at the interface. One mechanism for nanobubble stability suggests that a steady state exists from the gas flowing in and out of the bubble that prevents collapse[121], however these results would suggest that this not be possible.

Do Nanobubbles Without Oxygen Present?

Figure 36 shows the tapping (left) and contact (right) mode image for an OTS-coated sample submerged in ONS60 with sodium sulfite. We can see that nanobubbles readily formed even in the absence of dissolved oxygen. This implies that the nanobubbles present did not contain oxygen; however it is unclear from these results if the nanobubbles were formed by air being trapped in surface roughness during wetting or water vapor. The tapping and contact mode images in Figure 36 show evidence supporting that surface roughness may have been to blame for many of these bubbles. Note that the dark regions of the substrate tend to have bubbles present in the tapping mode image, but not always. Though these OTS-coated surfaces are quite smooth (<500 pm RMS roughness) there were shallow pits that formed on the substrate, likely due to the plasma etching prior to self-assembly with OTS.

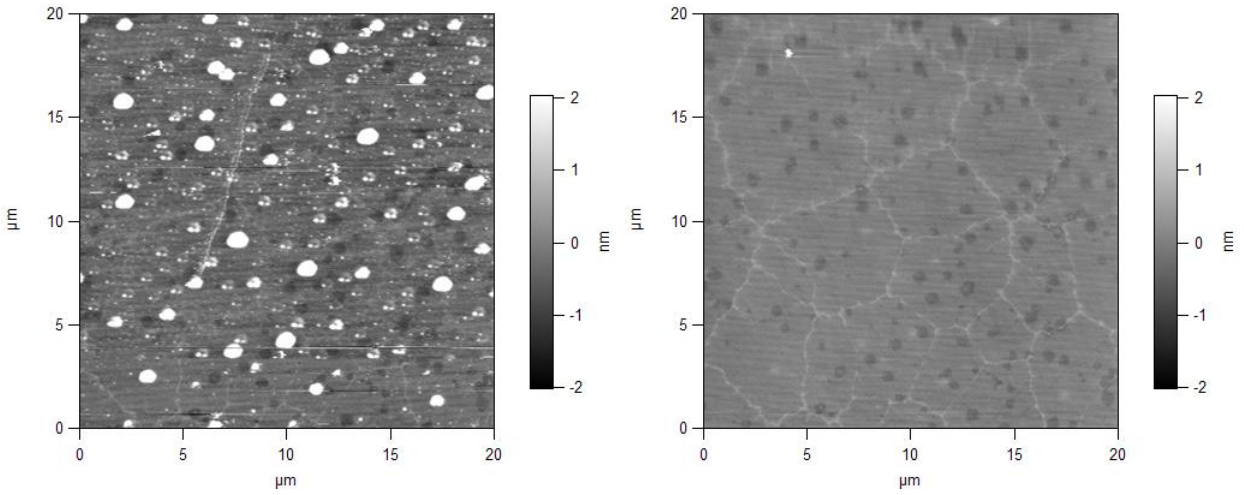

Figure 36: AFM tapping (left) and contact (right) mode images of a 20×20 µm² region of OTS-coated silicon submerged in ONS60 with sodium sulfite. Imaging was performed on a Cypher AFM (Asylum Research) using an ORC8 cantilever (68 kHz, 0.38 N/m, Bruker).

Overall, the presented images show evidence that spontaneously formed bubbles do not depend on the concentration of dissolved gas in the neighboring fluid, but are heavily dependent on the surface topography and water contact angle. In addition, even surfaces that appear mostly uniform can show large variation in bubble size and quantity between different regions in a given experiment. Furthermore the size and quantity of the bubbles appears to be determined during the initial wetting of the surface and is largely unaffected by changes to the solution.

Pinning of Nanobubbles at the Three Phase Line

We have shown that nanobubbles are very stable and resilient to changes in the surrounding system. However, there still remains the question of whether nanobubbles are mechanically pinned at the three phase line. For a pinned bubble, the radius of curvature will increase as gas diffuses out of the bubble, causing a lower Laplace pressure. Understanding if the bubbles are pinned on our OTS surfaces is therefore relevant to our gas diffusion studies.

The objective of these experiments was to see whether a mechanical force could be used to move the surface nanobubbles. i.e. are the bubbles pinned in one position, or can they be moved by applying a force? The force was applied with the AFM tip by changing the set-point. A greater set point corresponds to a greater force. A series of AFM contact mode images is presented in Figure 35. The relative set point was decreased from a start value of 120 mV (a) to 80 mV (b) then increased to 350 mV (c) and finally decreased to 250 mV (d) and back to the start value of 120 mV (e). The applied force at 350 mV (~150 nN) is large enough that the tip pushes all the way to the solid and the bubble in that location is completely flattened. The magnitude of the set point and the force that the tip is pressing against the substrate (and bubble) are directly related: a lower set point value will image the surface more gently and make a bubble look larger. On the contrary, imaging with a higher set point value will image the surface with a greater load and make a bubble look smaller. It should be no surprise that the bubbles in image b) look larger than those in image a).

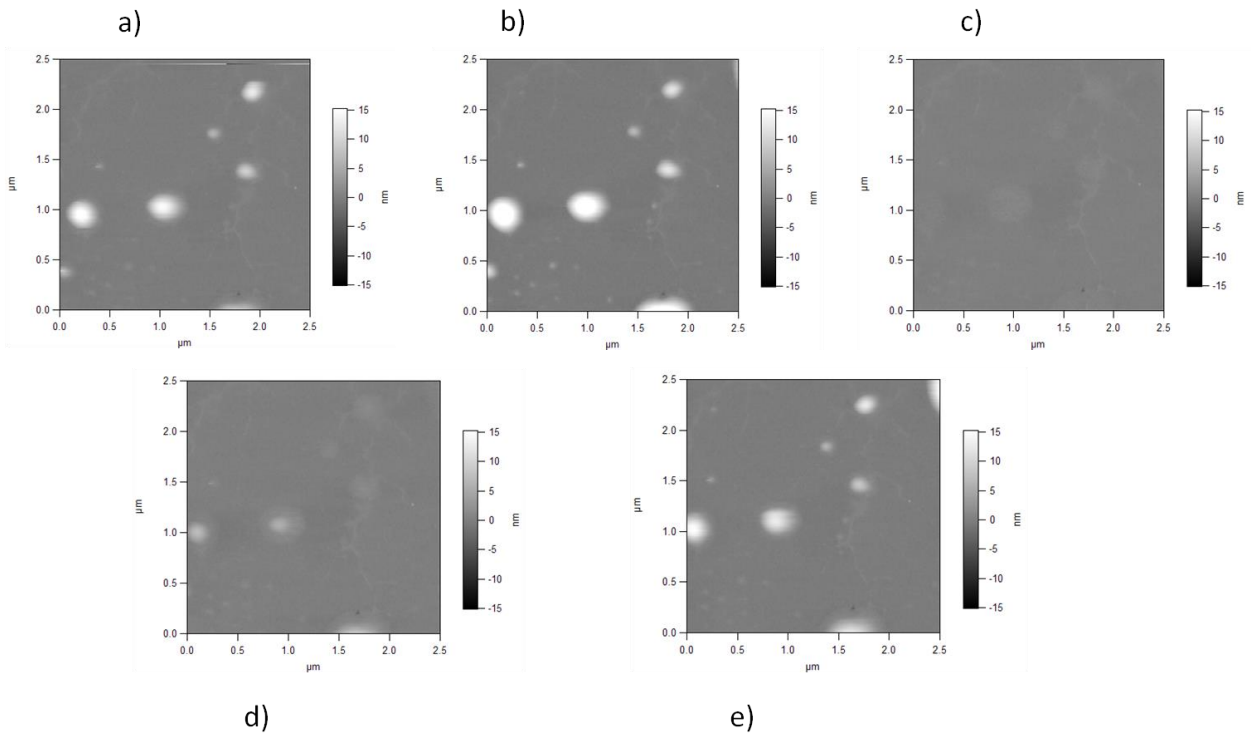

Figure 37: AFM contact mode imaging of a 2.5×2.5 μm² region of OTS-coated silicon submerged in RNS60 after sodium sulfite had been added. Relative set points ($V_{rel} = V_{sp} - V_{zero}$) for each image were as follows: a) 120 mV, b) 80 mV, c) 350 mV, d) 250 mV and e) 120 mV. Imaging was performed on a Cypher AFM (Asylum Research) using an ORC8 cantilever (68 kHz, 0.38 N/m, Bruker).

The interesting note here is that a comparison of image a) and e) show that the position and size of the bubbles was the same after applying a high force and moving the tip sideways through the bubble: the bubble edges remaining in the same place means that they are pinned.

As a side note, these images also demonstrate the sensitivity of the image to the parameters used. A mere 40 mV decrease in the relative set point from a) to b) produced a very noticeable increase in apparent bubble size. Drift in the set point of the course of an

experiment is not uncommon and this is important to keep in mind when interpreting differences in bubble heights in two different images.

Conclusions

In conclusion, nanobubbles formed on hydrophobic surfaces even in the absence of dissolved gas. These results are not in agreement with other findings that degassing, or reducing dissolved gas concentration, remove or greatly decrease the likelihood of bubble formation. This may simply suggest that the mechanism of bubble formation in the present work is not governed by the same variables as in other works.

Furthermore, bubble formation was far more dependent on the topography and hydrophobicity of the surface than on any pre-treatment of the solution or solution exchange. This issue made it difficult to draw comparisons with different data sets.

I also show that the two saline solutions, RNS60 and ONS60, did not show any difference in the number or size of nanobubbles formed at hydrophobic surfaces. Combined with the other conclusions, it is possible that differences are present between the two solutions but the solid-liquid interface is unaffected by these bulk differences. Finally, removing all of the dissolved gas from the solution did not collapse the bubbles, or noticeably change the bubble size. This suggests that the bubbles in this work were impermeable to oxygen or did not contain oxygen.

VIII. Future Work

The work presented shows that the interaction between hydrophobic surfaces in aqueous salt solutions is measureable down to ~5 nanometers, where a mechanical instability occurs. The measured attraction fits very well with Lifshitz-van der Waals calculation for a layered system up to the mechanical instability and Debye-Hückel theory for electric double layers. Furthermore, this mechanical instability was neither a function of temperature or electrolyte concentration. The hydrophobic effect is known to be temperature dependent and water structure is known to be disrupted at high salt concentrations which would lead to the conclusion that the origin of the measured force is unrelated to either of these phenomena. However, a number of additional experiments could help verify this hypothesis.

Characterization of the unstable region

As mentioned earlier, theoretical studies have related the strong, short-ranged attraction to cavitation caused by the transition of the liquid phase to a vapor phase. Lum et. al. [48] found that the lower limit of this transition is at ~5 nm of separation. However, the gradient of this cavitation force far exceeds the elastic constant of the cantilever used in my preliminary work. There are two approaches to solving this problem: increase the spring constant or decrease the force (by decreasing the radius of the sphere).

Appropriate cantilevers have been found with spring constants of ~45 N/m. These cantilevers are also tipless which will allow for much smaller spheres (R = 5 μm) to be used. My previous work utilized a spring constant of about 0.7 N/m and a sphere radius of

20 μm. Thus, we would be able to measure forces ~250 times stronger. Though this will reduce sensitivity to weak forces (such as the van der Waals interaction shown in my preliminary results) it will allow for measurement at separations of less than 5 nm on the approach force curve and the characterization of behavior during pull-off (the point at which the two surfaces separate).

Pull-off Force between Hydrophobic Surfaces

A phenomenon that has appeared in some of the force vs separation data is a bend in the withdraw curve. An example is presented in Figure 38 (circle).

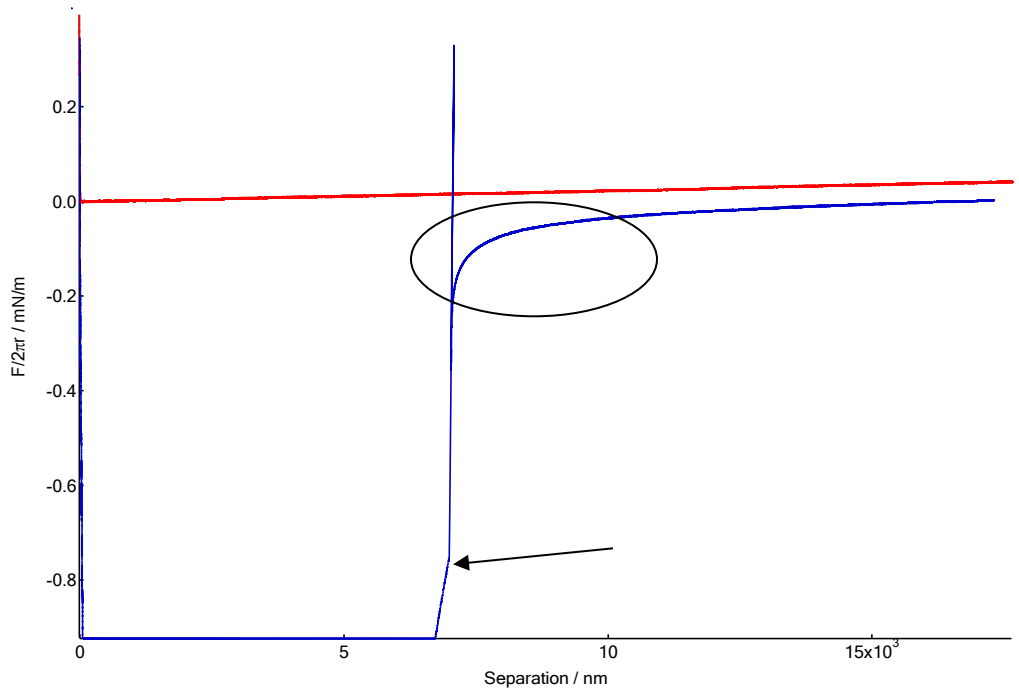

Figure 38: Force vs separation curve for OTS-coated borosilicate glass surfaces submerged in 150 mM KCl at 23° C. The red curve represents the approach curve and the blue curve represents the withdraw curve. The photodiode is saturated from 0 to ~6 μm of separation on the withdraw curve. The sharp increase in slope is an artifact caused by the laser falling off of the photodiode, giving the illusion that the deflection is decreasing because the overall voltage reading on the photodiode is decreasing. The two surfaces separate at the point marked by the arrow. The ~6 μm of deflection on the cantilever propels it through the fluid passed the line of zero deflection.

The key features of the withdraw curve is the bend that occurs. In a low viscosity fluid, like water, we would expect the slight ringing that occurs in the cantilever; however, the bend that appears after the ringing is something that is characteristic of an over-damped system.

One explanation for this phenomenon is a capillary is bridging the gap between the sphere and plate. However, if a capillary were to be the cause we would expect to see a second discontinuity in the force data where the cavity is ruptured. Another possibility would be that it is merely an artifact in the data collection, as with the other features present in Figure 38.

Linear Compliance from a Sliding Sphere

Another artifact present in several hydrophobic force measurements was briefly mentioned earlier (Figure 19). Recall that the constant compliance region represents hard contact between the two surfaces and is used for calibrating the light-lever sensitivity. However, linear compliance does not imply constant compliance. For example, a sphere sliding across a plate at a constant velocity will show linear compliance on a deflection vs displacement plot, but the change in deflection does not necessarily equal the change in displacement. This is possible because the planar surface is (most likely) not orthogonal to the z-axis that the sphere is approaching at, which allows the sphere to slide up or down the incline of the surface. This results in an apparent change in the zero separation (Figure 39).

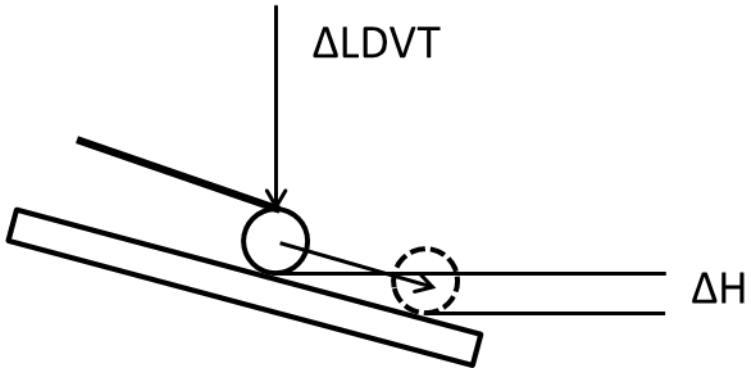

Figure 39: Schematic of a sphere and plate in contact during constant compliance. At high deflections the sphere may slide down (or up) and inclined planar surface and give the illusion that separation is changing even when the two surfaces are in hard contact.

It should be possible to back out the incline of the plate relative to the piezo from the slope of the 2nd linear compliance region after the deflection-displacement data is converted to force-separation.

Do Bubbles Contain Gas?

The sodium sulfite work presented here suggested that bubbles were impermeable to oxygen or did not contain oxygen. One argument for this is that the bubbles were formed by gas trapping in surface cracks. This would imply that the bubbles contain atmospheric gas rather than the pure oxygen that is dissolved in the saline solutions. It is reasonable to assume that sodium sulfite had no appreciable effect on bubble size because only about 20% of the gas would be oxygen.

To rememdy this issue we could wet the surface in an oxygen purged environment, for example a glove box filled with oxygen. If these bubbles were formed by gas trapping then

preparation of surfaces in this manner would ensure that bubbles contain oxygen. If sodium sulfite still does not affect bubble size then this procedure would suggest bubbles are gaseous, but impermeable or contain water vapor.

References

1. Christenson, H. K.; Claesson, P. M.; Berg, J.; Herder, P. C., Forces between Fluorocarbon Surfactant Monolayers - Salt Effects on the Hydrophobic Interaction. *J Phys Chem-Us* **1989,** *93* (4), 1472-1478.
2. Christenson, H. K.; Claesson, P. M.; Parker, J. L., Hydrophobic Attraction - a Reexamination of Electrolyte Effects. *J Phys Chem-Us* **1992,** *96* (16), 6725-6728.
3. Christenson, H. K.; Claesson, P. M.; Pashley, R. M., The Hydrophobic Interaction between Macroscopic Surfaces. *P Indian as-Chem Sci* **1987,** *98* (5-6), 379-389.
4. Christenson, H. K.; Fang, J. F.; Ninham, B. W.; Parker, J. L., Effect of Divalent Electrolyte on the Hydrophobic Attraction. *J Phys Chem-Us* **1990,** *94* (21), 8004-8006.
5. Christenson, H. K.; Yaminsky, V. V., Is the long-range hydrophobic attraction related to the mobility of hydrophobic surface groups? *Colloid Surface A* **1997,** *130*, 67-74.
6. Claesson, P. M.; Blom, C. E.; Herder, P. C.; Ninham, B. W., Interactions between Water-Stable Hydrophobic Langmuir-Blodgett Monolayers on Mica. *Journal of Colloid and Interface Science* **1986,** *114* (1), 234-242.
7. Claesson, P. M.; Christenson, H. K., Very Long-Range Attractive Forces between Uncharged Hydrocarbon and Fluorocarbon Surfaces in Water. *J Phys Chem-Us* **1988,** *92* (6), 1650-1655.
8. Claesson, P. M.; Herder, P. C.; Blom, C. E.; Ninham, B. W., Interactions between a Positively Charged Hydrophobic Surface and a Negatively Charged Bare Mica Surface. *Journal of Colloid and Interface Science* **1987,** *118* (1), 68-79.
9. Craig, V. S. J.; Ninham, B. W.; Pashley, R. M., Study of the long-range hydrophobic attraction in concentrated salt solutions and its implications for electrostatic models. *Langmuir* **1998,** *14* (12), 3326-3332.
10. Craig, V. S. J.; Ninham, B. W.; Pashley, R. M., Direct measurement of hydrophobic forces: A study of dissolved gas, approach rate, and neutron irradiation. *Langmuir* **1999,** *15* (4), 1562-1569.
11. Ederth, T., Substrate and solution effects on the long-range "hydrophobic" interactions between hydrophobized gold surfaces. *Journal of Physical Chemistry B* **2000,** *104* (41), 9704-9712.
12. Ederth, T., Computation of Lifshitz-van der Waals forces between alkylthiol monolayers on gold films. *Langmuir* **2001,** *17* (11), 3329-3340.
13. Ederth, T.; Claesson, P.; Liedberg, B., Self-assembled monolayers of alkanethiolates on thin gold films as substrates for surface force measurements. Long-range hydrophobic interactions and electrostatic double-layer interactions. *Langmuir* **1998,** *14* (17), 4782-4789.
14. Ederth, T.; Liedberg, B., Influence of wetting properties on the long-range "hydrophobic" interaction between self-assembled alkylthiolate monolayers. *Langmuir* **2000,** *16* (5), 2177-2184.
15. Hato, M., Attractive forces between surfaces of controlled ''hydrophobicity'' across water: A possible range of ''hydrophobic interactions'' between macroscopic hydrophobic surfaces across water. *J Phys Chem-Us* **1996,** *100* (47), 18530-18538.

16. Ishida, N.; Kinoshita, N.; Miyahara, M.; Higashitani, K., Effects of hydrophobizing methods of surfaces on the interaction in aqueous solutions. *Journal of Colloid and Interface Science* **1999,** *216* (2), 387-393.
17. Ishida, N.; Sakamoto, M.; Miyahara, M.; Higashitani, K., Attraction between hydrophobic surfaces with and without gas phase. *Langmuir* **2000,** *16* (13), 5681-5687.
18. Kim, S.; Christenson, H. K.; Curry, J. E., The effect of humidity on the stability of an octadecyltriethoxysilane monolayer self-assembled on untreated and plasma-treated mica. *Langmuir* **2002,** *18* (6), 2125-2129.
19. Kim, S.; Christenson, H. K.; Curry, J. E., n-octadecyltriethoxysilane monolayer coated surfaces in humid atmospheres: Influence of capillary condensation on surface deformation and adhesion. *Journal of Physical Chemistry B* **2003,** *107* (16), 3774-3781.
20. Kokkoli, E.; Zukoski, C. F., Interactions between hydrophobic self-assembled monolayers. Effect of salt and the chemical potential of water on adhesion. *Langmuir* **1998,** *14* (5), 1189-1195.
21. Kokkoli, E.; Zukoski, C. F., Effect of solvents on interactions between hydrophobic self-assembled monolayers. *Journal of Colloid and Interface Science* **1999,** *209* (1), 60-65.
22. Kurihara, K.; Kunitake, T., Submicron-Range Attraction between Hydrophobic Surfaces of Monolayer-Modified Mica in Water. *J Am Chem Soc* **1992,** *114* (27), 10927-10933.
23. Lin, Q.; Meyer, E. E.; Tadmor, M.; Israelachvili, J. N.; Kuhl, T. L., Measurement of the long- and short-range hydrophobic attraction between surfactant-coated surfaces. *Langmuir* **2005,** *21* (1), 251-255.
24. Meyer, E. E.; Lin, Q.; Hassenkam, T.; Oroudjev, E.; Israelachvili, J. N., Origin of the long-range attraction between surfactant-coated surfaces. *Proceedings of the National Academy of Sciences of the United States of America* **2005,** *102* (19), 6839-6842.
25. Ohnishi, S.; Ishida, T.; Yaminsky, V. V.; Christenson, H. K., Characterization of fluorocarbon monolayer surfaces for direct force measurements. *Langmuir* **2000,** *16* (6), 2722-2730.
26. Ohnishi, S.; Yaminsky, V. V.; Christenson, H. K., Measurements of the force between fluorocarbon monolayer surfaces in air and water. *Langmuir* **2000,** *16* (22), 8360-8367.
27. Parker, J. L.; Claesson, P. M., Forces between Hydrophobic Silanated Glass Surfaces. *Langmuir* **1994,** *10* (3), 635-639.
28. Parker, J. L.; Claesson, P. M.; Cho, D. L.; Ahlberg, A.; Tidblad, J.; Blomberg, E., Plasma Modification of Mica. *Journal of Colloid and Interface Science* **1990,** *134* (2), 449-458.
29. Parker, J. L.; Claesson, P. M.; Wang, J. H.; Yasuda, H. K., Surface Forces between Plasma Polymer-Films. *Langmuir* **1994,** *10* (8), 2766-2773.
30. Parker, J. L.; Yaminsky, V. V.; Claesson, P. M., Surface Forces between Glass Surfaces in Cetyltrimethylammonium Bromide Solutions. *J Phys Chem-Us* **1993,** *97* (29), 7706-7710.
31. Podgornik, R.; Parsegian, V. A., An Electrostatic-Surface Stability Interpretation of the Hydrophobic Force Inferred to Occur between Mica Plates in Solutions of Soluble Surfactants. *Chem Phys* **1991,** *154* (3), 477-483.
32. Podgornik, R.; Parsegian, V. A., Forces between Ctab-Covered Glass Surfaces Interpreted as an Interaction-Driven Surface Instability. *J Phys Chem-Us* **1995,** *99* (23), 9491-9496.
33. Proust, J. E.; Perez, E.; Segui, Y.; Montalan, D., Formation and Characterization of an Ultrathin Polysiloxane Film onto Mica. *Journal of Colloid and Interface Science* **1988,** *126* (2), 629-633.
34. Rabinovich, Y. I.; Guzonas, D. A.; Yoon, R. H., Role of Chain Order in the Long-Range Attractive Force between Hydrophobic Surfaces. *Langmuir* **1993,** *9* (5), 1168-1170.
35. Rabinovich, Y. I.; Yoon, R. H., Use of Atomic-Force Microscope for the Measurements of Hydrophobic Forces. *Colloid Surface A* **1994,** *93*, 263-273.

36. Rabinovich, Y. I.; Yoon, R. H., Use of Atomic-Force Microscope for the Measurements of Hydrophobic Forces between Silanated Silica Plate and Glass Sphere. *Langmuir* **1994,** *10* (6), 1903-1909.
37. Schmitt, F. J.; Ederth, T.; Weidenhammer, P.; Claesson, P.; Jacobasch, H. J., Direct force measurements on bulk polystyrene using the bimorph surface forces apparatus. *J Adhes Sci Technol* **1999,** *13* (1), 79-96.
38. Tsao, Y. H.; Evans, D. F.; Wennerstrom, H., Long-Range Attraction between a Hydrophobic Surface and a Polar Surface Is Stronger Than That between 2 Hydrophobic Surfaces. *Langmuir* **1993,** *9* (3), 779-785.
39. Tsao, Y. H.; Yang, S. X.; Evans, D. F.; Wennerstrom, H., Interactions between Hydrophobic Surfaces - Dependence on Temperature and Alkyl Chain-Length. *Langmuir* **1991,** *7* (12), 3154-3159.
40. Wood, J.; Sharma, R., How Long Is the Long-Range Hydrophobic Interaction? *Langmuir* **1995,** *11*, 4797-4802.
41. Yaminsky, V. V.; Ninham, B. W., Remarks on the limitation of the range of the hydrophobic force. *Langmuir* **1996,** *12* (20), 4969-4970.
42. Yaminsky, V. V.; Ninham, B. W.; Christenson, H. K.; Pashley, R. M., Adsorption forces between hydrophobic monolayers. *Langmuir* **1996,** *12* (8), 1936-1943.
43. Bratko, D.; Luzar, A., Attractive surface force in the presence of dissolved gas: A molecular approach. *Langmuir* **2008,** *24* (4), 1247-1253.
44. Forsman, J.; Jonsson, B.; Woodward, C. E., Computer simulations of water between hydrophobic surfaces: The hydrophobic force. *J Phys Chem-Us* **1996,** *100* (36), 15005-15010.
45. Jensen, T.; Østergaard Jensen, M.; Reitzel, N.; Balashev, K.; Peters, G.; Kjaer, K.; Bjørnholm, T., Water in Contact with Extended Hydrophobic Surfaces: Direct Evidence of Weak Dewetting. *Physical Review Letters* **2003,** *90* (8).
46. Lee, C. Y.; Mccammon, J. A.; Rossky, P. J., The Structure of Liquid Water at an Extended Hydrophobic Surface. *J. Chem. Phys.* **1984,** *80* (9), 4448-4455.
47. Leung, K.; Luzar, A.; Bratko, D., Dynamics of capillary drying in water. *Physical Review Letters* **2003,** *90* (6), 065502.
48. Lum, K.; Chandler, D.; Weeks, J. D., Hydrophobicity at Small and Large Length Scales. *J Phys. Chem. B* **1999,** *103*, 4570-4577.
49. Lum, K.; Luzar, A., Pathway to surface-induced phase transition of a confined fluid. *Phys Rev E* **1997,** *56* (6), R6283-R6286.
50. Luzar, A.; Bratko, D.; Blum, L., Monte-Carlo Simulation of Hydrophobic Interaction. *J. Chem. Phys.* **1987,** *86* (5), 2955-2959.
51. Patel, A. J.; Varilly, P.; Chandler, D., Fluctuations of Water near Extended Hydrophobic and Hydrophilic Surfaces. *Journal of Physical Chemistry B* **2010,** *114* (4), 1632-1637.
52. Patel, A. J.; Varilly, P.; Jamadagni, S. N.; Acharya, H.; Garde, S.; Chandler, D., Extended surfaces modulate hydrophobic interactions of neighboring solutes. *Proceedings of the National Academy of Sciences of the United States of America* **2011,** *108* (43), 17678-17683.
53. Pratt, L. R.; Chandler, D., Theory of Hydrophobic Effect. *J. Chem. Phys.* **1977,** *67* (8), 3683-3704.
54. Israelachvili, J. N.; Pashley, R. M., Measurement of the Hydrophobic Interaction between 2 Hydrophobic Surfaces in Aqueous-Electrolyte Solutions. *Journal of Colloid and Interface Science* **1984,** *98* (2), 500-514.
55. Christenson, H. K.; Claesson, P. M., Direct measurements of the force between hydrophobic surfaces in water. *Advances in Colloid and Interface Science* **2001,** *91* (3), 391-436.
56. Meyer, E. E.; Rosenberg, K. J.; Israelachvili, J., Recent progress in understanding hydrophobic interactions. *Proceedings of the National Academy of Sciences of the United States of America* **2006,** *103* (43), 15739-15746.

57. Meagher, L.; Craig, V. S. J., Effect of Dissolved-Gas and Salt on the Hydrophobic Force between Polypropylene Surfaces. *Langmuir* **1994,** *10* (8), 2736-2742.
58. Blake, T. D. K., J. A., Stability of aqueous films on hydrophobic methylated silica. *J Chem Soc Farad T 1* **1972,** *68*, 1435-1442.
59. Verwey, E. J. W.; Overbeek, J. T. G., *Theory of the Stability of Lyophobic Colloids*. Dover Publications: 1999; p 218.
60. Hall, D. G., *J Chem Soc Farad T 2* **1972,** *68*, 2168-2182.
61. Ash, S. G.; Everett, D. H.; Radke, C., *J Chem Soc Farad T 2* **1973,** *69*, 1256-1277.
62. Carambassis, A.; Jonker, L. C.; Attard, P.; Rutland, M. W., Forces measured between hydrophobic surfaces due to a submicroscopic bridging bubble. *Physical Review Letters* **1998,** *80* (24), 5357-5360.
63. Parker, J. L.; Claesson, P. M.; Attard, P., Bubbles, Cavities, and the Long-Ranged Attraction between Hydrophobic Surfaces. *J Phys Chem-Us* **1994,** *98* (34), 8468-8480.
64. Parker, J. L.; Cho, D. L.; Claesson, P. M., Plasma Modification of Mica - Forces between Fluorocarbon Surfaces in Water and a Nonpolar Liquid. *J Phys Chem-Us* **1989,** *93* (16), 6121-6125.
65. Attard, P., Thermodynamic analysis of bridging bubbles and a quantitative comparison with the measured hydrophobic attraction. *Langmuir* **2000,** *16* (10), 4455-4466.
66. Attard, P., Nanobubbles and the hydrophobic attraction. *Advances in Colloid and Interface Science* **2003,** *104*, 75-91.
67. Attard, P.; Moody, M. P.; Tyrrell, J. W. G., Nanobubbles: the big picture. *Physica A* **2002,** *314* (1-4), 696-705.
68. Ducker, W. A., Contact Angle and Stability of Interfacial Nanobubbles. *Langmuir* **2009,** *25* (16), 8907-8910.
69. Zhang, X. H.; Khan, A.; Ducker, W. A., A nanoscale gas state. *Physical Review Letters* **2007,** *98* (13).
70. Miklavic, S. J.; Chan, D. Y. C.; White, L. R.; Healy, T. W., Double-Layer Forces between Heterogeneous Charged Surfaces. *J Phys Chem-Us* **1994,** *98* (36), 9022-9032.
71. Hampton, M. A.; Donose, B. C.; Nguyen, A. V., Effect of alcohol-water exchange and surface scanning on nanobubbles and the attraction between hydrophobic surfaces. *Journal of Colloid and Interface Science* **2008,** *325* (1), 267-274.
72. Zhang, X. H.; Quinn, A.; Ducker, W. A., Nanobubbles at the interface between water and a hydrophobic solid. *Langmuir* **2008,** *24* (9), 4756-4764.
73. Berard, D. R.; Attard, P.; Patey, G. N., Cavitation of a Lennard-Jones Fluid between Hard Walls, and the Possible Relevance to the Attraction Measured between Hydrophobic Surfaces. *J. Chem. Phys.* **1993,** *98* (9), 7236-7244.
74. Eriksson, J. C.; Ljunggren, S.; Claesson, P. M., A Phenomenological Theory of Long-Range Hydrophobic Attraction Forces Based on a Square-Gradient Variational Approach. *J Chem Soc Farad T 2* **1989,** *85*, 163-176.
75. Jensen, T.; Østergaard Jensen, M.; Reitzel, N.; Balashev, K.; Peters, G.; Kjaer, K.; Bjørnholm, T., Water in Contact with Extended Hydrophobic Surfaces: Direct Evidence of Weak Dewetting. *Physical Review Letters* **2003,** *90* (8), 086101
76. Mezger, M.; Reichert, H.; Schöder, S.; Okasinski, J.; Schröder, H.; Dosch, H.; Palms, D.; Ralston, J.; Honkimäki, V., High resolution in situ x-ray study of the hydrophobic gap at the water-octadecyl-trichlorosilane interface. *Proc. Natl Acad. Sci.* **2006,** *103* (49), 18401-18404.
77. Poynor, A.; Hong, L.; Robinson, I. K.; Granick, S.; Zhang, Z.; Fenter, P. A., How Water Meets a Hydrophobic Surface. *Phys. Rev. Lett.* **2006,** *97*, 266101.
78. Mao, M.; Zhang, J. H.; Yoon, R. H.; Ducker, W. A., Is there a thin film of air at the interface between water and smooth hydrophobic solids? *Langmuir* **2004,** *20* (5), 1843-1849.

79. Pertsin, A. J.; Hayashi, T.; Grunze, M., Grand canonical Monte Carlo Simulations of the hydration interaction between oligo(ethylene glycol)-terminated alkanethiol self-assembled monolayers. *Journal of Physical Chemistry B* **2002,** *106* (47), 12274-12281.
80. Hayashi, T.; Pertsin, A. J.; Grunze, M., Grand canonical Monte Carlo simulation of hydration forces between nonorienting and orienting structureless walls. *J. Chem. Phys.* **2002,** *117* (13), 6271-6280.
81. Cottin-Bizonne, C.; Steinberger, A.; Cross, B.; Raccurt, O.; Charlaix, E., Nanohydrodynamics: The intrinsic flow boundary condition on smooth surfaces. *Langmuir* **2008,** *24* (4), 1165-1172.
82. Hammer, M. U.; Anderson, T. H.; Chaimovich, A.; Shell, M. S.; Israelachvili, J., The search for the hydrophobic force law. *Faraday Discussions* **2010,** *146*, 299-308.
83. Binnig, G.; Quate, C. F.; Gerber, C., Atomic Force Microscope. *Physical Review Letters* **1986,** *56* (9), 930-933.
84. Butt, H. J.; Cappella, B.; Kappl, M., Force measurements with the atomic force microscope: Technique, interpretation and applications. *Surf Sci Rep* **2005,** *59* (1-6), 1-152.
85. Cappella, B.; Dietler, G., Force-distance curves by atomic force microscopy. *Surf Sci Rep* **1999,** *34* (1-3), 1-+.
86. Ducker, W. A.; Senden, T. J.; Pashley, R. M., Measurement of Forces in Liquids Using a Force Microscope. *Langmuir* **1992,** *8* (7), 1831-1836.
87. Derjaguin, B. V.; Muller, V. M.; Toporov, Y. P., Effect of Contact Deformations on Adhesion of Particles. *Journal of Colloid and Interface Science* **1975,** *53* (2), 314-326.
88. Hutter, J. L.; Bechhoefer, J., Calibration of Atomic-Force Microscope Tips. *Rev Sci Instrum* **1993,** *64* (7), 1868-1873.
89. Hamaker, H. C., The London-van der Waals attraction between spherical particles. *Physica* **1937,** *4*, 1058-1072.
90. Parsegian, V. A., *Van der Waals Force: A Handbook for Biologists, Chemists, Engineers, and Physicists*. Cambridge University Press: Cambridge, 2006.
91. Hough, D. B.; White, L. R., The Calculation of Hamaker Constants from Lifshitz Theory with Applications to Wetting Phenomena. *Advances in Colloid and Interface Science* **1980,** *14* (1), 3-41.
92. Mastropietro, D. J.; Ducker, W. A., Forces between Hydrophobic Solids in Concentrated Aqueous Salt Solution. *Physical Review Letters* **2012,** *108* (10).
93. BK7 http://www.cvimellesgriot.com/products/Documents/Catalog/Dispersion_Equations.pdf (accessed Accessed: September 25th, 2011).
94. Bevan, M. A.; Prieve, D. C., Direct measurement of retarded van der Waals attraction. *Langmuir* **1999,** *15* (23), 7925-7936.
95. Ducker, W. A.; Senden, T. J.; Pashley, R. M., Direct Measurement of Colloidal Forces Using an Atomic Force Microscope. *Nature* **1991,** *353* (6341), 239-241.
96. Honig, C. D. F.; Ducker, W. A., Thin Film Lubrication for Large Colloidal Particles: Experimental Test of the No-Slip Boundary Condition. *Journal of Physical Chemistry C* **2007,** *111*, 16300-16312
97. Derjaguin, B. V., *Kolloid Z.* **1934,** *69*, 155-164 See also Hunter, R. J. Foundations of Colloid Science, Vol. I; Oxford Science Press, Oxford, 1987, p191.
98. White, L. R., van der Waals interaction energy and disjoining pressure at small separation. *Journal of Colloid and Interface Science* **2010,** *343* (1), 338-343.
99. Johnson, K. L.; Kendall, K.; Roberts, A. D., *Proc R Soc London Ser A* **1971,** *324*, 301–313.
100. Hutter, J. L.; Bechhoefer, J., Calibration of Atomic-Force Microscope Tips (Vol 64, Pg 1868, 1993). *Rev Sci Instrum* **1993,** *64* (11), 3342-3342.
101. Stachurski, J.; Michalek, M., The effect of the zeta potential on the stability of a non-polar oil-in-water emulsion. *Journal of Colloid and Interface Science* **1996,** *184* (2), 433-436.

102. Chan, D. Y.; Dagastine, R. R.; White, L. R., Forces between a Rigid Probe Particle and a Liquid Interface. *J Colloid Interface Sci* **2001,** *236* (1), 141-154.
103. Stiernstedt, J.; Rutland, M. W.; Attard, P., A novel technique for the in situ calibration and measurement of friction with the atomic force microscope. *Rev Sci Instrum* **2005,** *76* (8).
104. Derjaguin, B. V., *Kolloid Z.* **1934,** *69*, 155-164.
105. Hunter, R. J., *Foundations of Colloid Science*. Oxford University Press: Oxford, 2001.
106. Kuznetsov, V.; Papastavrou, G., Ion Adsorption on Modified Electrodes as Determined by Direct Force Measurements under Potentiostatic Control. *J Phys Chem C* **2014,** *118* (5), 2673-2685.
107. Galamba, N., On the Effects of Temperature, Pressure and Dissolved Salts on the Hydrogen-bond Network of Water (vol 117, pg 589, 2013). *Journal of Physical Chemistry B* **2013,** *117* (18), 5792-5792.
108. Hampton, M. A.; Nguyen, A. V., Nanobubbles and the nanobubble bridging capillary force. *Advances in Colloid and Interface Science* **2010,** *154* (1-2), 30-55.
109. Mastropietro, D. J.; Ducker, W. A., Forces between hydrophobic solids in concentrated aqueous salt solution. *Phys. Rev. Lett.* **2012**.
110. Habich, A.; Ducker, W.; Dunstan, D. E.; Zhang, X. H., Do Stable Nanobubbles Exist in Mixtures of Organic Solvents and Water? *Journal of Physical Chemistry B* **2010,** *114* (20), 6962-6967.
111. Considine, R. F.; Hayes, R. A.; Horn, R. G., Forces measured between latex spheres in aqueous electrolyte: Non-DLVO behavior and sensitivity to dissolved gas. *Langmuir* **1999,** *15* (5), 1657-1659.
112. Yang, S. J.; Dammer, S. M.; Bremond, N.; Zandvliet, H. J. W.; Kooij, E. S.; Lohse, D., Characterization of nanobubbles on hydrophobic surfaces in water. *Langmuir* **2007,** *23* (13), 7072-7077.
113. Yang, J. W.; Duan, J. M.; Fornasiero, D.; Ralston, J., Very small bubble formation at the solid-water interface. *Journal of Physical Chemistry B* **2003,** *107* (25), 6139-6147.
114. Borkent, B. M.; Dammer, S. M.; Schonherr, H.; Vancso, G. J.; Lohse, D., Superstability of surface nanobubbles. *Physical Review Letters* **2007,** *98* (20).
115. Zhang, X. H.; Chan, D. Y. C.; Wang, D. Y.; Maeda, N., Stability of Interfacial Nanobubbles. *Langmuir* **2013,** *29* (4), 1017-1023.
116. Ishida, N.; Inoue, T.; Miyahara, M.; Higashitani, K., Nano bubbles on a hydrophobic surface in water observed by tapping-mode atomic force microscopy. *Langmuir* **2000,** *16* (16), 6377-6380.
117. Hampton, M. A.; Donose, B. C.; Taran, E.; Nguyen, A. V., Effect of nanobubbles on friction forces between hydrophobic surfaces in water. *Journal of Colloid and Interface Science* **2009,** *329* (1), 202-207.
118. Hampton, M. A.; Nguyen, A. V., Accumulation of dissolved gases at hydrophobic surfaces in water and sodium chloride solutions: Implications for coal flotation. *Miner Eng* **2009,** *22* (9-10), 786-792.
119. Hampton, M. A.; Nguyen, A. V., Systematically altering the hydrophobic nanobubble bridging capillary force from attractive to repulsive. *Journal of Colloid and Interface Science* **2009,** *333* (2), 800-806.
120. Yang, S.; Kooij, E. S.; Poelsema, B.; Lohse, D.; Zandvliet, H. J. W., Correlation between geometry and nanobubble distribution on HOPG surface. *Epl-Europhys Lett* **2008,** *81* (6).
121. Brenner, M. P.; Lohse, D., Dynamic Equilibrium Mechanism for Surface Nanobubble Stabilization. *Physical Review Letters* **2008,** *101* (21).
122. Lou, S. T.; Gao, J. X.; Xiao, X. D.; Li, X. J.; Li, G. L.; Zhang, Y.; Li, M. Q.; Sun, J. L.; Li, X. H.; Hu, J., Studies of nanobubbles produced at liquid/solid interfaces. *Mater Charact* **2002,** *48* (2-3), 211-214.
123. Zhang, X. H.; Ducker, W., Formation of interfacial nanodroplets through changes in solvent quality. *Langmuir* **2007,** *23* (25), 12478-12480.
124. Zhang, X. H.; Zhang, X. D.; Lou, S. T.; Zhang, Z. X.; Sun, J. L.; Hu, J., Degassing and temperature effects on the formation of nanobubbles at the mica/water interface. *Langmuir* **2004,** *20* (9), 3813-3815.
125. Zhang, X. H.; Maeda, N.; Craig, V. S. J., Physical properties of nanobubbles on hydrophobic surfaces in water and aqueous solutions. *Langmuir* **2006,** *22* (11), 5025-5035.

126. Wu, Z. H.; Zhang, X. H.; Zhang, X. D.; Li, G.; Sun, J. L.; Zhang, Y.; Li, M. Q.; Hu, J., Nanobubbles influence on BSA adsorption on mica surface. *Surf Interface Anal* **2006,** *38* (6), 990-995.
127. Mezger, M.; Schoder, S.; Reichert, H.; Schroder, H.; Okasinski, J.; Honkimaki, V.; Ralston, J.; Bilgram, J.; Roth, R.; Dosch, H., Water and ice in contact with octadecyl-trichlorosilane functionalized surfaces: A high resolution x-ray reflectivity study. *J. Chem. Phys.* **2008,** *128* (24).
128. Simonsen, A. C.; Hansen, P. L.; Klosgen, B., Nanobubbles give evidence of incomplete wetting at a hydrophobic interface. *Journal of Colloid and Interface Science* **2004,** *273* (1), 291-299.
129. Steitz, R.; Gutberlet, T.; Hauss, T.; Klosgen, B.; Krastev, R.; Schemmel, S.; Simonsen, A. C.; Findenegg, G. H., Nanobubbles and their precursor layer at the interface of water against a hydrophobic substrate. *Langmuir* **2003,** *19* (6), 2409-2418.